University of Warsaw

Faculty of Physics

Orbital effects in elemental chalcogens

Adam Kłosiński

A thesis presented for the degree of
Doctor of Philosophy

Advisor:
Dr hab. Krzysztof Wohlfeld

May 6, 2023

Author's publications

[1] A. Kłosiński, D. V. Efremov, J. van den Brink, and K. Wohlfeld, "Photoemission spectrum of Ca_2RuO_4: spin polaron physics in an $S = 1$ antiferromagnet with anisotropies", Phys. Rev. B 101, 035115 (2020).

[2] A. Kłosiński, A. M. Oleś, C. Efthimia Agrapidis, J. van Wezel, and K. Wohlfeld, "Chalcogenic orbital density waves in the weak- and strong-coupling limit", Phys. Rev. B 103, 235123 (2021).

[3] A. Kłosiński, W. Brzezicki, A. Lau, C. E. Agrapidis, A. M. Oleś, J. van Wezel, and K. Wohlfeld, "Topology of chalcogen chains", Phys. Rev. B 107, 125123 (2023).

[4] P. Wrzosek, A. Kłosiński, K. Wohlfeld, and C. E. Agrapidis, "Rare collapse of fermionic quasiparticles upon coupling to local bosons", Phys. Rev. B 107, 205103 (2023).

[5] P. Wrzosek, A. Kłosiński, Y. Wang, M. Berciu, C. E. Agrapidis, and K. Wohlfeld, "The fate of the spin polaron in the 1d antiferromagnet", (2022) 10.48550/arXiv.2203.01846.

Table of contents

1 Introduction **7**
1.1 This thesis . . . 11

2 Preliminaries **15**
2.1 **p** orbitals . . . 16
2.1.1 **p**-orbital rotations . . . 16
2.1.2 Tunnelling between **p** orbitals . . . 17
2.1.3 Inter-orbital Coulomb repulsion . . . 18
2.2 Helical chains . . . 19
2.2.1 Helical chain Hamiltonian . . . 20
2.2.2 Global orbital basis . . . 21
2.2.3 Generalised Bloch theorem . . . 22
2.3 Chalcogen chain Hamiltonian . . . 26
2.3.1 Spinless chalcogen chain . . . 27
2.3.2 Spinfull chalcogen chain and spin-orbit coupling . . . 27
2.3.3 Crystalline symmetry of the chalcogen chain . . . 30
2.3.4 The $\boldsymbol{\alpha} = \mathbf{90}^\circ$ chalcogen chain – the cubic limit . . . 31

3 Orbital density waves in chalcogen chains **33**
3.1 Model . . . 36
3.2 Non-interacting chalcogen chain . . . 37
3.2.1 Linearised bond angle dependence . . . 37
3.2.2 Band structure . . . 40
3.2.3 Ground state . . . 42
3.3 Hartree solution . . . 43
3.3.1 Mean-field decoupling . . . 43
3.3.2 Restricting the parameter space . . . 45

3.3.3 Hartree flow . . . 46
3.3.4 Ground state orbital density . . . 50
3.3.5 Two different orbital density waves . . . 51
3.4 Benchmark: Density Matrix Renormalization Group . . . 53
3.4.1 Motivation . . . 53
3.4.2 Method . . . 54
3.4.3 Results . . . 56
3.5 Conclusions . . . 58
3.5.1 Summary of results . . . 58
3.5.2 Final remarks . . . 59

4 Interlude: One-dimensional topological insulators 61
4.1 Introduction . . . 61
4.2 Chiral topological insulators in one dimension . . . 64
4.2.1 Su-Schrieffer-Heeger model . . . 65
4.3 Symmetry-protected one-dimensional topological insulators . . . 70
4.3.1 Period-three Su-Schrieffer-Heeger model . . . 71

5 Topology of chalcogen chains 79
5.1 Models . . . 80
5.2 Topology of the chalcogen chain model . . . 84
5.2.1 Band structure and spectrum . . . 84
5.2.2 Bulk topological properties . . . 86
5.2.3 Bulk-boundary correspondence . . . 87
5.2.4 End states . . . 92
5.3 Chalcogen chain model vs cubic chain model . . . 93
5.4 Comparison with orbital SSH model . . . 95
5.5 Conclusions . . . 96

A Table of abbreviations 99

Chapter 1

Introduction

In solid state physics, the change in the number of electrons per atom – and the resulting modification of the valence shell configuration – is accompanied by a change in the nature of the solid. There are three main mechanisms facilitating this. First, the number of weakly-bound electrons in the valence shell translates to the number of possible crystal configurations the atom can enter in its ionic form [1]. This is seen in transition metals, with the number of valence d sub-shell electrons ranging from 1 to 10, as compared with s or p block elements, with at most 2 or 6 valence sub-shell electrons respectively. Because of the relatively large number of valence sub-shell electrons, transitions metals – such as iron – occur in many different ionizations, and feature in a great number of compounds. Elemental crystals of transition metals are all metallic, hard and with high melting temperatures because of the large number of electrons available to form metallic bonds. This is in contrast with s and p block elements, among whom one finds not only metals but also insulators and semiconductors, and these elements that are metallic are soft and with comparatively low melting temperatures because of the lower number of valence electrons [1].

Second, not only the number of valence electrons, but also their orbital index is important. In many metals with valence d and f sub-shells, only a portion of valence electrons forms metallic bonds – some remain bound to the ion. This happens because of the more localised charge distribution in the d and particularly f sub-shell orbitals compared with the s and p orbitals [2] [1]. These bound electrons give rise to localised spin moments and therefore to magnetism in transition and rare-earth metals, which

[1] Note that the spatial extent of s p d and f orbitals with the same principal quantum number n is comparable. The localised nature of f and d orbitals is a result of the order in which the shells are filled, which is such that in the valence shell the principal quantum number of the d and f orbitals is always lower than that of the p and s orbitals.

is absent in the p and s block metals.

Third, not only the extent of the charge distribution, but also its shape differs between the f, d, p and s orbitals. This is particularly important for electrons that are associated with a particular ion and not delocalised over the entire crystal lattice, i.e. in covalent materials or in metallic atoms forming ionic bonds with ligands. There, the electrostatic repulsion between the charge distributions (i.e. the orbital shapes) on neighbouring ions matters. An example of this can be found in the p block, where there is a propensity to form covalent bonds with the coordination number $8 - N$, where N is the number of electrons in the valence shell (two s electrons plus the number of p electrons in the valence sub-shell). This is called the octet rule [3]. When such covalent bonds form, there exist particular angles between the bonds which minimise the electrostatic energy of the bonding orbitals. This leads to specific crystal structures, such as the lattice of graphene, polyatomic rings of sulphur with coordination number two, or the 104.5° angle between the two covalent bonds in the molecule of water [4].

The second and third mechanisms described above are collectively known as orbital phenomena. Although they were appreciated early on in molecular physics, their impact on the electronic properties of solids was not immediately realised. Historically, the electronic properties of solids were first understood for metals, which were initially modelled using the free electron model [5], which treated electrons as a gas of free fermions and completely disregarded the lattice. The nearly free electron model followed, which considered the electrostatic potential of the lattice as a weak perturbation [6]. Both models assumed electrons behaved like delocalised Bloch waves, with approximately constant charge distribution across the entire crystal, thus excluding the possibility of localised electrons or different orbital shapes.

It was eventually realised that these models were not correct, especially once the first experiments mapping the Fermi surface appeared, which showed that the Fermi surfaces of metals were far from spherical, unlike what the free and almost-free electron models predicted. What followed was the search for new theoretical methods. Apart from a few exact solutions to the Schrödinger equation in a periodic potential, such as the Kronig-Penney model [7], this led to the advent of band theory, with approximate methods such as Density Functional Theory [8] and the tight-binding (TB) approximation [9]. Both of these methods borrowed heavily from molecular physics [2], in particular from valence bond theory [11] and molecular orbital theory [12], which together form the foundations for modern quantum chemistry. In band theory,

[2] In particular, the TB approximation is essentially a simplification of the Linear Combination of Atomic Orbitals (LCAO) method [10] developed as an approximation of the molecular orbital theory.

one consider overlaps between localised orbitals centred on neighbouring atoms and thus orbital shapes become crucial. The theory can be applied to metals and insulators alike and is still extensively used today. It has already explained a wide range of effects in solid state physics, including many linked to orbital phenomena. I list some of these effects below.

In the d block, the consequences of the d orbital shape can be seen when transition metal ions form ionic bonds with ligands, in the phenomenon of orbital momentum quenching. The quenching arises because of the electrostatic potential of ligands which enforce a symmetry on the transition metal ion d orbitals, such as the octahedral symmetry in perovskites. This is called the crystal field (CF) effect and it leads to a splitting of the d sub-shell energy levels into the e_g doublet and the t_{2g} triplet. These new orbitals have vanishing projections of angular momentum on all three axes and effective total angular momentum of 0 (e_g orbitals) and 1 (t_{2g} orbitals), suppressing the orbital magnetic moment on the transition metal ions. This in turn leads to weaker spin-orbit coupling (SOC). The d orbital valence is a crucial element in this scenario, as it is the d orbital charge distributions which couple to the crystal environment introducing the CF splitting. This mechanism is much weaker in rare-earth compounds, because the f electrons are more localised and their interaction with the crystal environment is weaker. Consequently, rare-earth compounds exhibit considerably stronger SOC effects than transition metal compounds.

Another example of an orbital phenomenon in transition metal compounds is the Jahn-Teller distortion [13]. This crystal structure distortion occurs when it is energetically favourable to induce further splittings within the e_g or t_{2g} energy levels by lowering the crystal symmetry. The Jahn-Teller effect is most pronounced when the e_g orbitals are partly occupied. A prime example is the d^9 configuration of the copper Cu^{2+} ion at the center of the CuO_6 octahedron in cuprates. There, a single hole occupies the degenerate e_g orbitals leading to a two-fold degenerate ground state (discounting spin degeneracy) and it is energetically favourable to introduce a splitting in the e_g orbitals by distorting the CuO_6 octahedra [14]. Just as with orbital momentum quenching, the Jahn-Teller distortions are much weaker in rare earth elements than in transition metals because of the more localised nature of the f electrons.

For a completely different type of orbital phenomenon, a strong link between orbitals and topology has recently been demonstrated in the so-called orbital Su-Schrieffer-Heeger (orbital SSH) model [15]. There, a half-filled zigzag chain with local p orbital degrees of freedom has been demonstrated to split into two copies of the SSH model [16] and SSH-like end states were found for each orbital flavour. The

mechanism behind this remarkable fact is the alternating strong-weak bonding pattern of each p orbital flavour on consecutive x and y bonds. In all probability, this discovery is just the tip of the colloquial iceberg, as topology is encoded in band structures and the band shape (Fermi velocity) in the TB approximation depends chiefly on inter-site orbital overlaps. These overlaps, in turn, are a direct consequence of orbital shapes, i.e. the difference between σ bonds, π bonds and non-overlapping orbitals.

Up to now electron-electron interactions were excluded from the discussion. In some solids, however, the accurate description of the electronic structure cannot be achieved without them. Electron-electron interactions lead to even richer orbital physics. In Mott insulators [17] the superexchange mechanism [18], in which electrons on rare-earth or transition metal ions interact via ligand orbitals, leads to effective magnetic interactions between spins localised on said ions. The result, in some cases, is long-range magnetic order. The superexchange interaction is a second and higher order process. It depends on (i) the inter-ion tunnelling amplitude $t_{ij}^{\alpha\beta}$, where i and j number the ions in the lattice and α and β number the orbitals, and (ii) the electron-electron interaction. Because of the dependence on $t_{ij}^{\alpha\beta}$ it can be highly spatially anisotropic for fixed α and β.

An example of a superexchange interaction is the antiferromagnetic interaction in the copper-oxygen planes in cuprates. In the case of an orbitally non-degenerate ground state, such as the d^9 configuration of the copper ion, the sign and magnitude of the superexchange interaction are governed by Goodenough-Kanamori-Anderson rules [19–21]. $t_{ij}^{\alpha\beta}$ becomes independent of the orbital index and the Hamiltonians describing such systems do not include orbital degrees of freedom, as the exact orbital ground state is always known.

If the orbital ground state is degenerate, however, the models become much more complex. The degenerate ground state leads to Jahn-Teller distortions, which need to be considered along with superexchange. The resulting Hamiltonians contain both spin and orbital degrees of freedom [3] and are known as Kugel-Khomskii-type models [22]. There, magnetic interactions are heavily dependent on the lattice, because different lattice symmetries lead to different CF splittings, different Jahn-Teller distortions and different superexchange processes. This leads to a variety of coexisting orbital (structural) and magnetic orders, with structural and magnetic phase transitions occurring at different temperatures. One example is the 'ferromagnetic' orbital order of the e_g orbitals in the spinel structure of $CuFe_2O_4$, with an associated distortion towards a tetragonal crystal structure. In the same material a Neel antiferromag-

[3] I am not talking about relativistic effects. SOC is a different phenomenon to the one described here.

netic order is observed, which sets in at a lower temperature. Another example is the 'antiferromagnetic' (alternating) orbital order of the e_g orbitals in perovskites $KCuF_3$ and $LaMnO_3$, accompanied by a tetragonal distortion of the octahedra. Both materials exhibit concomitant magnetic order consisting of antiferromagnetically coupled ferromagnetic planes.

1.1 This thesis

In this thesis I focus on two systems in which orbital physics is key – the elemental chalcogens selenium and tellurium, which are sufficiently similar so as to be described by a single TB model. The chalcogens were originally studied in the 50s and 60s of the last century [23–25], with a few recent developments, such as the papers by Fukutome [26] and Shimoi and Fukutome [27], as well as work by Silva *et. al.* [28, 29]. Yet, there has so far been no attempt to describe these systems using modern concepts in orbital physics – such as orbital order and the multi-orbital Hubbard model – developed for the study of correlated systems. The topological properties of elemental chalcogens also remain largely unscrutinised. In this thesis I set out to provide a fuller description of elemental selenium and tellurium using these modern concepts.

The crystal structure of selenium and tellurium consists of weakly-coupled helical chains [23–25, 30] (chalcogen chains), arranged in a two-dimensional, hexagonal pattern, with helixes' axes parallel to each other (see Fig. 2.5). It is these one-dimensional chains that I study, following the precedent set by other authors [23–25]. The ground state of a single helical chain is an orbitally-ordered state, called an orbital density wave (ODW) [28, 29], in which different orbitals are occupied on each of the three inequivalent sites of the period-three helix. This situation is a result of the helical geometry and the p orbital shape, and leads to physics very different from that of simple, linear chains. This is described in detail in **chapter 2**, where chalcogen chains are introduced.

In chalcogen chains, I investigate two distinct problems. One, in **chapter 3** I consider the effect of weak inter-orbital Coulomb repulsion on the ODW ground state of a spinless chain. This question is related to previous research [28], which indicated that inter-orbital Coulomb repulsion might be responsible for the structural deformation of a hypothetical parent simple cubic lattice which would stabilise the three-dimensional crystal structure of elemental selenium and tellurium. The inclusion of an inter-orbital Coulomb term in the Hamiltonian, however, is known to destabilise

simple chains, leading to a Peiers-type transition [31]. Is it the same for chalcogen chains? I find that such a deformation does not occur in chalcogen chains for realistic values of the electron-electron interaction parameter U, because of the insulating nature of the chains and their sizeable band gap, both a consequence of the p orbital valence. This is an important conclusion, as it shows that the deformation mechanism proposed in [28] is not inconsistent. The research presented in chapter 3 is based on the article [32] of which I was a co-author.

Two, following a brief introduction to one-diemnsional topological insulators in **chapter 4**, in **chapter 5** I consider the topology of a realistic, spinfull chalcogen chain with non-zero SOC, which has not previously been studied in much detail. I find that the chalcogen chain harbours a topological ground state, with end states protected by a 180-degree rotation symmetry of the chain. The exponentially decaying end states have a particular form, with the charge density exactly zero on every third site. This feature is linked to the physics of the period-three Su-Schrieffer-Heeger model (SSH-3) [33]. In terms of bulk topological properties, I find that the relevant topological invariant is the Lau-Brink-Ortix (LBO) invariant [34], only recently defined. These findings lead one to expect topological surface states in elemental chalcogens, which form from the end states of individual chalcogen chains via the weak inter-chain coupling. Indeed, some unexplained surface magnetism has been recently reported in selenium crystals [35]. Chapter 5 is based on the article [36] of my co-authorship.

Altogether, this thesis offers a detailed look on the electronic properties of elemental chalcogens as well as describes original research which uncovers novel phenomena in these materials. On the one hand it investigates the effect of electron-electron interactions in selenium and tellurium, on the other it describes and classifies the topological ground state of chalcogen chains. The latter result offers a promising platform for future research, investigating the topological properties of three-dimensional selenium and tellurium where one expects the end states of individual chalcogen chains to form surface states. These surface states are orbitally polarised and coupled to spin via SOC, which leads one to expect some form of surface magnetism.

Another interesting avenue of research opened by this thesis is the numerical investigation of the phase transition in the ODW ground state of chalcogen chains due to inter-orbital Coulomb repulsion. The results presented in chapter 3 concentrate chiefly on the two extreme ODW ground states – one in the weak coupling regime, relevant to chalcogens, and one in the strong coupling regime. What is only mentioned in passing in the conclusions to chapter 3 is that the Density Matrix Renormalisation Group (DMRG) results strongly indicate an intermediate phase, with a large ground-state degeneracy. Even though not physically relevant to chalcogen chains due to the

unrealistically large Coulomb repulsion needed to stabilise it, this intermediate phase might be interesting from a model point of view, as the large ground state degeneracy translates to orbital frustration.

Chapter 2

Preliminaries

In this chapter I introduce the models that will be studied throughout the thesis, that is the spinless and the spinfull chalcogen chain model, as well as a broader class of models to which the chalcogen chains belong, namely helical chain models. Even though any valence sub-shell can be considered in helical chains (and the results will strongly depend on the choice), in order to make the discussion more tangible and focused I restrict it to helical chains whose active sub-shell is the p sub-shell. The reason for this choice is simple – the p sub-shell is the relevant sub-shell for the chalcogen chains, which are the focus of this work. The chapter is structured as follows.

In Sec. 2.1 I discuss the p orbitals. I begin with the discussion of the transformation properties of p orbitals under rotations (Sec. 2.1.1). Next, I discuss the results of Slater and Koster [9], who used an approximation to the LCAO method [10] to derive simple, nearest-neighbour tight-binding tunnelling matrix elements for p orbital systems (Sec. 2.1.2). I finish this section with a description of Coulomb repulsion in the p sub-shell for a spinless system (Sec. 2.1.3).

In Sec. 2.2 the discussion focuses on helical chains. I discuss a general Hamiltonian of a helical chain (Sec. 2.2.1) and a convenient basis choice in dealing with helical chains (Sec. 2.2.2). I then discuss a key symmetry – the helical symmetry – which allows for a much simplified treatment of helical chain Hamiltonians, making use of the so-called generalised Bloch theorem (GBT) (Sec. 2.2.3). In the entire section the discussion is restricted to spinless helical chains.

In Sec, 2.3 I discuss a particular instance of a helical chain, the chalcogen chain, which is a period-three helical chain with a specific bond angle α. This is the model which is studied throughout this thesis. In the first subsection (Sec. 2.3.1) I give the

Hamiltonian of a spinless chalcogen chain and discuss it as an example of a helical chain. In the second subsection (Sec. 2.3.2) I turn to the discussion of the spin-full chalcogen chain and SOC. This subsection also generalises the helical symmetry to include spin. In the third subsection (Sec. 2.3.3) I look at another key symmetry of a chalcogen chain – the 180-degree rotation. In the final subsection (Sec. 2.3.4) I introduce a simplified version of the chalcogen chain model, which I call the cubic chain model. The cubic chain model is distinguished from the standard chalcogen chain model by a different helix bond angle, $\alpha = 90^\circ$ and vanishing SOC.

2.1 p orbitals

To begin with, let me recall some properties of p-orbitals. The three p orbitals, p_x, p_y and p_z, constitute a real orbital basis in the p sub-shell – a basis which is the simplest to work with and which I will be using throughout this thesis. I will denote the basis states in a p-orbital chain as

$$|j, \mu\rangle \equiv \mathbf{c}^\dagger_{j\mu} |0\rangle \,, \tag{2.1}$$

where j is the lattice site index and $\mu = x, y, z$ is the orbital index, while $\mathbf{c}^\dagger_{j\mu}$ is the creation operator of an electron on orbital p_μ and on site j. $|0\rangle$ is the vacuum of the Fock space. I will sometimes omit the site index j when talking about single atom properties. The notation will then be

$$|j, \mu\rangle \to |\mu\rangle \,. \tag{2.2}$$

2.1.1 p-orbital rotations

The transformation properties of the p orbitals under rotations are the same as for vectors expressed in Cartesian coordinates. Consider the rotation matrix $O(\vec{v}, \theta)$, where $\vec{v}$ is the rotation axis and θ is the angle of rotation. The generators of rotations are the projections of angular momentum onto the Cartesian axes

$$\vec{l} = (l_x, l_y, l_z). \tag{2.3}$$

The rotations themselves are given by the exponential map

$$O(\vec{v}, \theta) = e^{i\vec{v}\cdot\vec{l}\theta}. \tag{2.4}$$

Note that I pick a convention which defines the operators l_m as hermitian, so that the rotation matrices are anti-symmetric. In the p-orbital basis the matrix form of the hermitian operators l_m, $m = x, y, z$ is

$$(l_m)_{jk} = i\epsilon_{mjk}, \tag{2.5}$$

where m, j and k take one of the values x, y, z and ϵ_{mij} is the Levi-Civita symbol. This leads to the standard rotation matrices in Cartesian coordinates

$$\begin{aligned} O(\vec{x},\theta) &= \begin{pmatrix} 1 & 0 & 0 \\ 0 & \cos\theta & -\sin\theta \\ 0 & \sin\theta & \cos\theta \end{pmatrix}, \\ O(\vec{y},\theta) &= \begin{pmatrix} \cos\theta & 0 & \sin\theta \\ 0 & 1 & 0 \\ -\sin\theta & 0 & \cos\theta \end{pmatrix}, \\ O(\vec{z},\theta) &= \begin{pmatrix} \cos\theta & -\sin\theta & 0 \\ \sin\theta & \cos\theta & 0 \\ 0 & 0 & 1 \end{pmatrix}. \end{aligned} \tag{2.6}$$

The transformation of the p orbitals under rotations is therefore given by

$$|\nu\rangle = \sum_{\mu=x,y,z} O(\vec{v},\theta)_{\nu\mu} |\mu\rangle, \tag{2.7}$$

with the rotation matrix expressed in the Cartesian basis [see (2.6)].

2.1.2 Tunnelling between p orbitals

In their seminal 1954 paper [9] Slater and Koster described an approximation to the LCAO method [10] and found a simplified description of nearest-neighbour tunnelling matrix elements in a periodic crystal with a valence s, p or d sub-shell. Here I will use their result for the p sub-shell to construct the tight-binding Hamiltonians of first – a general helical chain, and second – a chalcogen chain.

In [9] Slater and Koster provide expressions for tunnelling integrals between any pair of p orbitals[1] along an arbitrarily-oriented bond. The bond direction is expressed

[1] In their paper [9] the authors provide expressions for Löwdin p-type orbitals [37], not standard p-orbitals. Here and throughout I will call the Löwdin p-type orbitals p-orbitals for brevity, as their transformation properties are the same as for the standard p orbitals.

using the normalised tunnelling vector $\vec{n}$ pointing from the center of one p-orbital to the center of the other. Different possible orientations of the p orbitals with respect to the bond result in the splitting of an arbitrary tunnelling matrix element into two components. The first component, t_σ, corresponds to the tunnelling integral between two p orbitals oriented along the bond, while the second component, t_π, corresponds to the tunnelling matrix element between two p orbitals oriented perpendicular to the bond. Thus, an arbitrary tunnelling matrix element between two p orbitals is a function of t_σ, t_π and the tunnelling vector $\vec{n}$. It is [9]

$$K = \begin{pmatrix} n_x^2\delta t + t_\pi & -n_x n_y \delta t & -n_x n_z \delta t \\ -n_y n_x \delta t & n_y^2 \delta t + t_\pi & -n_y n_z \delta t \\ -n_z n_x \delta t & -n_z n_y \delta t & n_z^2 \delta t + t_\pi \end{pmatrix}, \tag{2.8}$$

with $\delta t = t_\sigma - t_\pi$ and $\vec{n} = (n_x, n_y, n_z)$. (2.8) can be used directly to construct a tight-binding Hamiltonian for a chain and obtain the band structure.

2.1.3 Inter-orbital Coulomb repulsion

In this section I will describe Coulomb repulsion within the p sub-shell in a spinless system (Hubbard interaction term). I restrict the discussion to the spinless system because the spinless chalcogen chain is one of the models studied in this thesis and is also a natural starting point in defining the spinfull chalcogen chain, discussed later. Since I am interested in the spinless case, I need only consider inter-orbital Coulomb repulsion.

The interaction between each pair of p orbitals is the same – this is simply a consequence of the rotational symmetry of the Coulomb term. In any p-orbital basis the Coulomb interaction Hamiltonian for a spinless chalcogen chain is

$$\mathbf{H}_{\text{Coul.}} = \sum_j \sum_{\substack{\mu,\nu=x,y,z \\ \mu\neq\nu}} U \mathbf{n}_{j\mu}\mathbf{n}_{j\nu}, \tag{2.9}$$

where

$$\mathbf{n}_{j\mu} = \mathbf{c}^\dagger_{j\mu}\mathbf{c}_{j\mu}. \tag{2.10}$$

Throughout this thesis I will be interested exclusively in the 2/3 filling case. For a spinless p-orbital system this means two electrons out of three. The on-site Hilbert space dimension for such a system is three – there are three distinct pairs of p orbitals, whose energies are all equal to U.

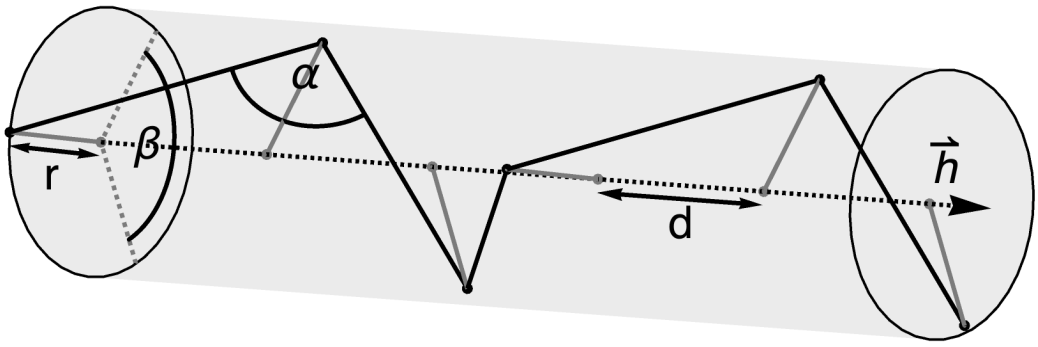

Figure 2.1: The period-three helical chain. The atoms are arranged along the helical axis $\vec{h}$ indicated by a dashed line. All sites in the helical chain lie on the wall of the shaded gray cylinder. The distance of each atom from the helical axis is r. The projection of the chain sites onto the helical axis is shown. The fixed distance between the projected points is d. This is the helix pitch. Also shown is the helix angle β, equal to 120° for a period-three helix, and the helix bond angle α.

2.2 Helical chains

Before I discuss chalcogen chains I want to look at a more general class of models, namely helical chains. This is a convenient path to follow, because a key symmetry of chalcogen chains – the helical symmetry – is a feature chalcogen chains share with this wider class of models. Helical symmetry is a purely geometric feature of a helix and therefore is most conveniently discussed using the general Hamiltonian of a helical chain, rather than the more particular Hamiltonian of the chalcogen chain, where other peculiarities of chalcogen chains – such as their period being equal to three – might obfuscate the discussion of helical symmetry.

A helical chain is an arrangement of atoms in a helical pattern around a common helical axis $\vec{h}$. Such a chain can be built by taking an atom at a distance r from the helical axis $\vec{h}$, sliding it along $\vec{h}$ by a fixed distance d – called the helix pitch – and rotating by a fixed angle β – called the helix angle – around the helix axis $\vec{h}$. Applying this transformation N times yields a helical chain of length N. A period-three helical chain of length $N = 6$ is shown in Fig. 2.1.

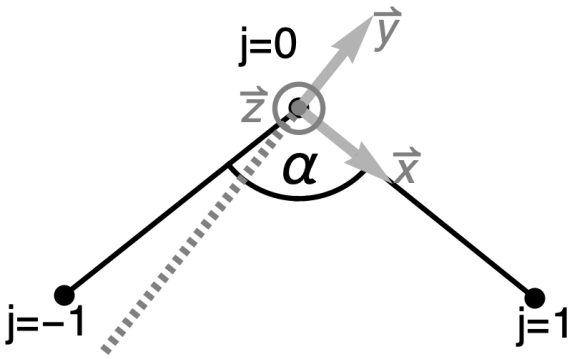

Figure 2.2: The $\vec{x}, \vec{y}, \vec{z}$ basis vectors of the p-orbital basis defined in this section. The figure is drawn in the plane defined by three sites, in this case $j = -1, 0, 1$, called the bond angle plane. The basis vectors are shown in relation to the bond angle α (see Fig. 2.1). The sites with $j = -1, 0, 1$ are chosen because the basis is defined with respect to the bond joining sites with $j = 0$ and $j = 1$ (see Sec. 2.2.1). Note that the bond angle between any three neighbouring sites is always the same for a helix.

2.2.1 Helical chain Hamiltonian

The TB Hamiltonian of a helical chain can be built in an iterative fashion. First, one chooses a site in the helix and gives it the index $j = 0$. Then, one picks the bond joining this site with the next one along the helix ($j = 1$). Next, one calculates the tunnelling matrix K along that bond. The result is dependent on the p-orbital basis choice [see Sec. 2.1.2]. Given a tunnelling matrix K [whose general form is (2.8)], the TB Hamiltonian of the helical chain is

$$\mathbf{H}_{\text{hel.}} = \sum_j \vec{\mathbf{c}}^{\dagger}_{j+1} \left(O(\vec{h}, \beta)^j \right)^{\dagger} K O(\vec{h}, \beta)^j \vec{\mathbf{c}}_j + \text{h.c.}, \tag{2.11}$$

where $O(\vec{h}, \beta)$ is a matrix representing the orbital basis rotation by the helix angle β around the helix axis $\vec{h}$ and

$$\vec{\mathbf{c}}_j = (\mathbf{c}_{jx}, \mathbf{c}_{jy}, \mathbf{c}_{jz}). \tag{2.12}$$

Equation (2.11) is simply a consequence of the fact that the j-th bond is rotated with respect to the zero-th bond j times around the helix axis $\vec{h}$ by the helix angle β.

2.2.2 Global orbital basis

The choice of the p-orbital basis in which to express (2.11) is a matter of personal preference. One can strive to make either the tunnelling matrices K, or the rotation matrices $O(\vec{h}, \beta)$ as simple as possible. I follow the former strategy. To this end, I define my p-orbital basis, which I will call the *global* orbital (GO) basis, in the following way.

I pick a site in the helix and label it as $j = 0$, then:

1. the x axis is parallel to the bond joining the $j = 0$ and $j = 1$ sites, pointing towards the $j = 1$ site,
2. the z axis is normal to the bond-angle plane, with the direction chosen so that $\vec{z} \cdot \vec{h}$ is positive,
3. the y axis is defined by the other two.

This basis is shown in Fig. 2.2 in relation to the bond angle. The basis is the same on every site, meaning that

$$\forall i, j \ \vec{x}_i \cdot \vec{x}_j = 1, \tag{2.13}$$
$$\forall i, j \ \vec{y}_i \cdot \vec{y}_j = 1, \tag{2.14}$$
$$\forall i, j \ \vec{z}_i \cdot \vec{z}_j = 1, \tag{2.15}$$

where x_j is the x basis vector defined on site j, similarly for y_j and z_j. This is what I mean by calling this basis a GO basis.

The advantage of this basis choice is that the tunnelling matrix K [see (2.11)], defined for the bond between sites with $j = 0$ and $j = 1$, takes a particularly simple form. According to Slater-Koster rules [9] (see Sec. 2.1.2), for this basis choice one gets

$$K = \begin{pmatrix} t_\sigma & 0 & 0 \\ 0 & t_\pi & 0 \\ 0 & 0 & t_\pi \end{pmatrix}, \tag{2.16}$$

with t_σ and t_π defined in Sec. 2.1.2. On the other hand, the expression for the helical axis $\vec{h}$ is relatively complicated. Namely

$$\vec{h} = O\left(\vec{a}, \theta\right) \cdot \vec{z}, \tag{2.17}$$

where $O(\vec{a}, \theta)$ is the standard Euclidean rotation (2.6) around the rotation axis

$$\vec{a} = O\left(\vec{z}, 180^\circ - \frac{\alpha}{2}\right) \cdot \vec{x}, \tag{2.18}$$

by the angle

$$\theta = \frac{180}{\pi} \arccos \frac{\tan \pi/6}{\tan \alpha/2}, \tag{2.19}$$

where α is the helix bond angle [2].

The Hamiltonian of a helical chain for this choice of basis is therefore (2.11) with K given by (2.16) and $\vec{h}$ given by (2.17)-(2.18).

2.2.3 Generalised Bloch theorem

The Bloch theorem [10] applies to non-interacting electrons in periodic potentials, in particular chains. The physics of electrons in such chains can be described by single-particle Hamiltonians that commute with the single particle translation operator $\mathbf{T}$

$$\mathbf{T} = \sum_j \vec{\mathbf{c}}^{\dagger}_{j+1} \cdot \vec{\mathbf{c}}_j. \tag{2.20}$$

Bloch's theorem establishes that a convenient single-particle basis for such periodic Hamiltonians is given by the pseudo-momentum basis

$$\vec{\mathbf{c}}_q = \frac{1}{\sqrt{N}} \sum_j e^{ijaq} \vec{\mathbf{c}}_j, \tag{2.21}$$

where

$$q = \frac{2\pi n}{Na}, \qquad n = 0, 1, ..., N-1, \tag{2.22}$$

is the pseudo-momentum, a is the inter-atomic distance in the chain, N is the chain length and

$$\vec{\mathbf{c}}_q = (\mathbf{c}_{qx}, \mathbf{c}_{qy}, \mathbf{c}_{qz}), \tag{2.23}$$

where $\mathbf{c}_{q\mu}$ is the annihilation operator of an electron with pseudo-momentum q and orbital flavour p_μ. This basis is the eigenbasis of $\mathbf{T}$

$$\mathbf{T} = \sum_q e^{iqa} \vec{\mathbf{c}}^{\dagger}_q \cdot \vec{\mathbf{c}}_q. \tag{2.24}$$

[2] θ is the angle between the $\vec{z}$ vector of the GO basis and the helix axis $\vec{h}$, which makes (2.19) a basis-dependent expression. Moreover, since this is an angle in three dimensions, the derivation of (2.19) is tedious, in spite of its simple geometric interpretation. Because of this, the derivation is not shown.

Consequently, for a single-particle Hamiltonian commuting with $\mathbf{T}$, the electron's pseudo-momentum is a conserved quantity. Therefore, if a Hamiltonian commutes with $\mathbf{T}$ it takes a particularly simple form in the pseudo-momentum basis – it separates into blocks, one for each distinct pseudo-momentum. Since there are N distinct pseudo-momenta, this is a great simplification.

For helical chains the Bloch theorem does not directly apply, as $\mathbf{T}$ is not a symmetry. This is because, unlike for a simple chain, for a helix each site is not equivalent. Some helices do have a period, for instance every third site is equivalent if $\beta = 120°$. In this case one can still use the Bloch theorem by defining a larger, three-atom unit cell, taking the inter-atomic distance a to be thrice larger and letting the index μ in (2.23) number not only orbitals, but also non-equivalent atoms in the unit cell. This, however, leads to a larger single-particle Hilbert space – the increase in size is by a factor equal to the period of the helix, in this case three. Other helical chains have no period at all – they can be called incommensurate. For such chains the angle β, given in degrees, is irrational.

Luckily, one can relatively simply generalise the Bloch theorem to the helical case. This is because any helix has a type of translational symmetry – the helical symmetry. The symmetry operator is

$$\mathbf{O}(\vec{h},\beta)\mathbf{T} = \sum_j \left(\vec{\mathbf{c}}^\dagger_{j+1} \cdot O(\vec{h},\beta)^\dagger\right) \cdot \vec{\mathbf{c}}_j, \tag{2.25}$$

where $\mathbf{O}(\vec{h},\beta)$ is a rotation of the entire helix by an angle β around the helical axis $\vec{h}$. $O(\vec{h},\beta)$, meanwhile, is the rotation $\mathbf{O}(\vec{h},\beta)$ applied to the orbitals on a single site, just as in (2.11). It is independent of the site index j, as $\mathbf{O}(\vec{h},\beta)$ is a rotation of the entire chain.

The operator $\mathbf{O}(\vec{h},\beta)\mathbf{T}$ is diagonalised by the transformation

$$\vec{\mathbf{c}}_Q = \frac{1}{\sqrt{N}} \sum_Q e^{ijaQ} O(\vec{h},\beta)^j \cdot \vec{\mathbf{c}}_j. \tag{2.26}$$

I will call (2.26) the generalised pseudo-momentum (GP) basis. The transformation from the GO basis to the GP basis is a combination of a discrete Fourier Transform (FT) and an orbital basis change

$$\vec{\mathbf{c}}'_j = O(\vec{h},\beta)^j \cdot \vec{\mathbf{c}}_j. \tag{2.27}$$

I will call the basis defined by (2.27) the *local* orbital (LO) basis. Both the LO basis and the GO basis of Sec. 2.2.2 are shown in Fig. 2.3 (b) and (a) respectively. One

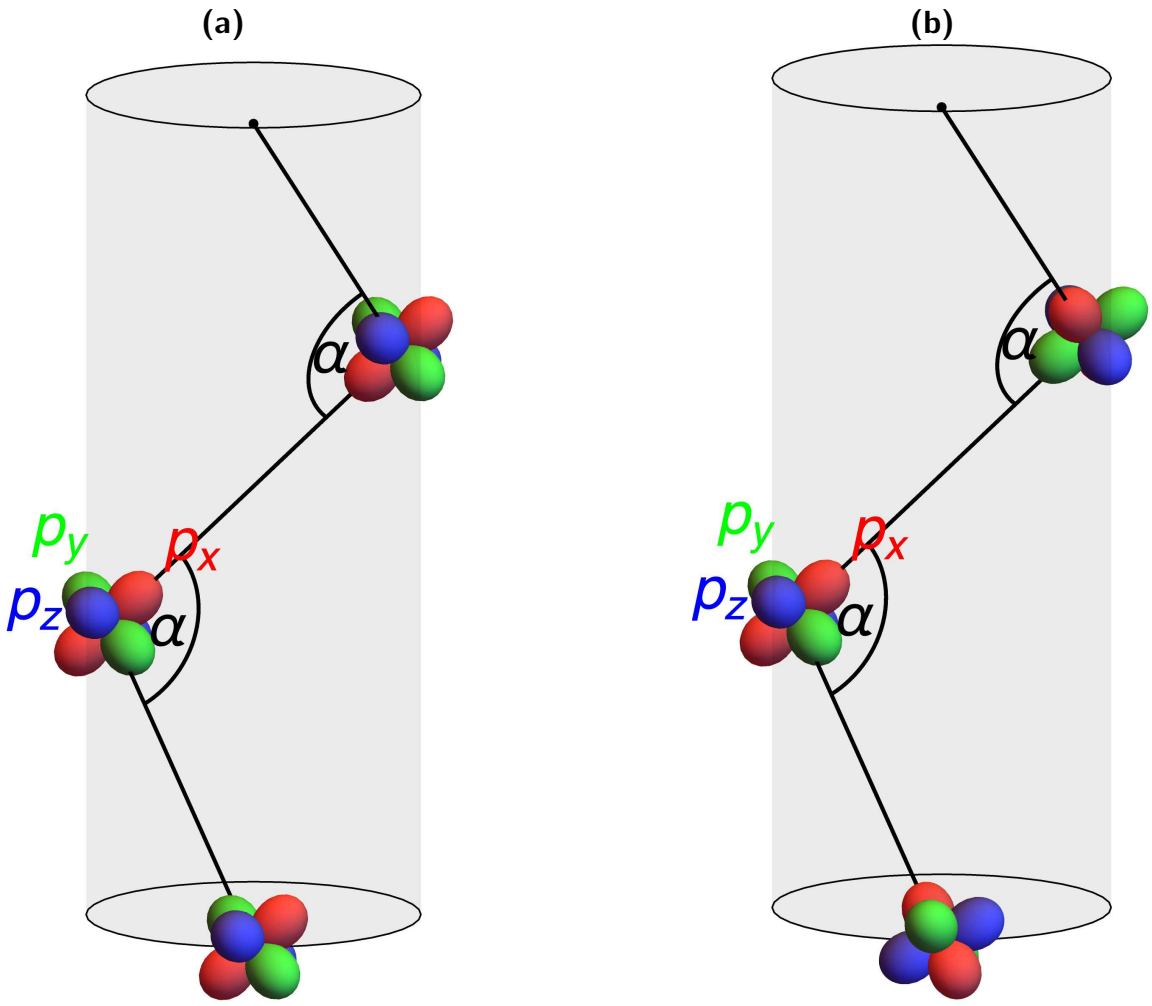

Figure 2.3: (a) The GO basis of Sec. 2.2.2 and (b) the LO basis (2.27) of section 2.2.3 in relation to the period-three helical chain (see also Fig. 2.1). The p_x, p_y and p_z orbitals are indicated by schematic orbital shapes coloured red, green and blue respectively. In the GO basis, the basis is the same irrespective of the position in the helical chain (a), in the LO basis the orbital basis rotates from one site to another (b). The helix bond angle α is also shown. All sites of the helical chain lie on the wall of the shaded gray cylinder.

can clearly see that in contrast to the GO basis of Sec. 2.2.2, the LO basis (2.27) is defined differently on different sites of the helix. This is precisely what I mean when I call this basis local. The schematic relationship between the various bases discussed

$$\text{(GO)} \xrightarrow{\text{Eq. (2.27)}} \text{(LO)} \xrightarrow{\text{FT}} \text{(GP)}$$

Figure 2.4: The relation between the various bases used in this chapter. The bases are: the global orbital basis (GO), the local orbital basis (LO) and the general pseudo-momentum basis (GP). The superscripts above the arrows indicate the transformations which map each basis onto the next. FT stands for discrete Fourier transform (2.21). Only the mapping in one direction is shown, although both mappings are bijective.

in this chapter is presented in Fig. 2.4.

In the GP basis the Hamiltonian (2.11) takes the simple form

$$\mathbf{H}_{\text{hel.}} = \sum_{Q} e^{iQa} \vec{\mathbf{c}}_Q^\dagger O(\vec{h}, \beta)^\dagger K \vec{\mathbf{c}}_Q + \text{h.c.}, \tag{2.28}$$

with K defined in (2.16) and $\vec{h}$ defined in (2.17)-(2.18). The dimension of $O(\vec{h}, \beta)^\dagger K$ is just the number of degrees of freedom on a single site, therefore the basis change (2.26) maps the helical chain onto a period-one chain. This is true even for incommensurate, non-periodic helices.

The only complication with working in the GP basis (2.26) is that for any calculated observable one needs to down-fold the pseudo-momenta to the fundamental unit-cell of the helix (which, for an incommensurate helix, can even be the entire chain) and translate the orbital basis back to a natural GO basis, i.e. apply the inverse of (2.27).

Finally, since I will be discussing topological properties in this thesis, I stress that – at least for any commensurate helix – working in the GP basis (2.26) does not affect the topological properties of the chain. This is because for any periodic helix the GP basis (2.26) differs from the standard Bloch basis (2.21) by the orbital basis change (2.27), which is a global unitary transformation, i.e. a unitary transformation which is the same in every fundamental unit cell. In the case of chalcogen chains, where the period and the size of the unit cell is three, and therefore $\beta = 120°$, this is manifested in the fact that

$$O(\vec{h}, 120°)^3 = \mathbb{1}_3, \tag{2.29}$$

which shows that the GO basis on every fourth site (on each equivalent atom in the chain) is the same [cf. (2.27)].

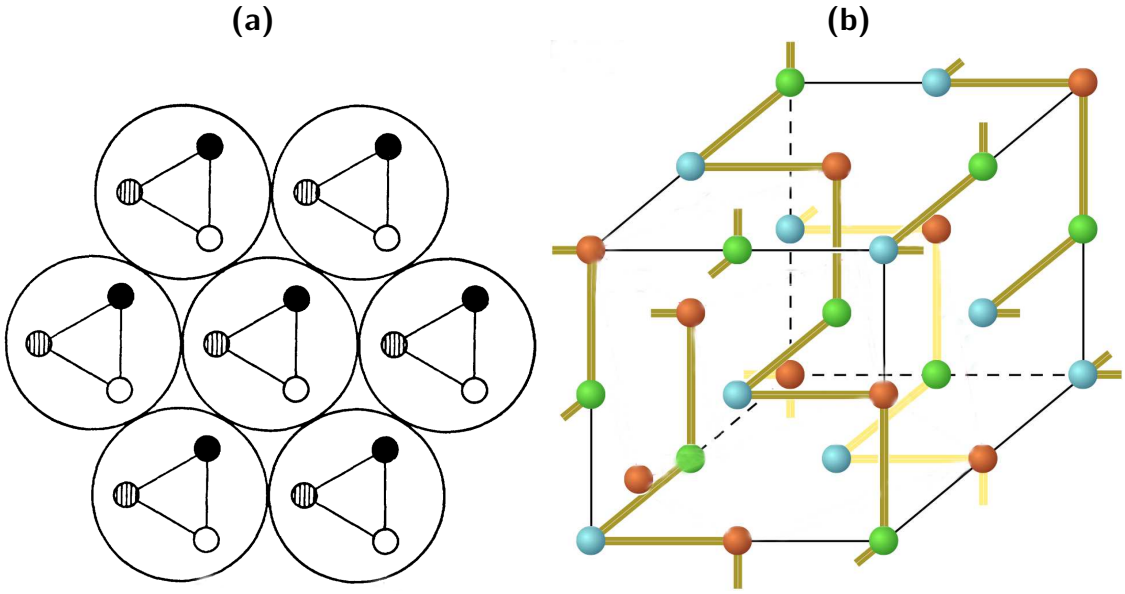

Figure 2.5: (a) The crystal structure of elemental selenium and tellurium, top view. The structure can be understood as a collection of helical chains (see Fig. 2.1) arranged on a hexagonal lattice. The shading of the atoms indicates that they lie on different layers, each perpendicular to the surface of the page. *Panel borrowed from [24].* (b) The crystal structure of elemental chalcogens can be understood as a collection of short bonds (solid, bright and dark yellow lines) in a simple cubic lattice. The long bonds are not shown. Sets of continuously connected short bonds constitute chalcogen chains. The three inequivalent atom positions in each chalcogen chain are coloured red, green and blue. *Panel borrowed from [28].*

2.3 Chalcogen chain Hamiltonian

This ends the general discussion of helical chains. From now on I will focus on the particular case of chalcogen chains, which are period-three helical chains, i.e. with the helix angle $\beta = 120°$. Chalcogen chain is a building block of the crystal structure of trigonal selenium and tellurium, also called elemental chalcogens [23, 24], where the chains are arranged in a two-dimensional, hexagonal pattern, with helical axes parallel to each other (see Fig. 2.5). Elemental chalcogens have been extensively studied in the middle of the last century and early on it was noticed that the helical chains in these systems might be considered as weakly-coupled [23–25], an observation corroborated by more recent numerical studies [30]. The chalcogen

chains are period-three helical chains with bond angles α reported in the literature ranging from 102.5° to 105, 4° for selenium [38] and from 102.6° to 103° for tellurium [24, 38]. Here I will use a value of $\alpha = 103°$ which falls within the ranges reported for both materials.

2.3.1 Spinless chalcogen chain

The TB Hamiltonian of the spinless chalcogen chain in the GP basis is

$$\mathbf{H}_{\text{chalc.}} = \sum_{Q} e^{iQa} \vec{\mathbf{c}}_{Q}^{\dagger} O(\vec{h}, 120°)^{\dagger} K \vec{\mathbf{c}}_{Q} + \text{h.c.}, \tag{2.30}$$

and the Hamiltonian in real space and in the GO basis is

$$\mathbf{H}_{\text{chalc.}} = \sum_{j} \vec{\mathbf{c}}_{j+1}^{\dagger} \left(O(\vec{h}, 120°)^{j} \right)^{\dagger} K O(\vec{h}, 120°)^{j} \vec{\mathbf{c}}_{j} + \text{h.c.}, \tag{2.31}$$

with K defined in (2.16) and $\vec{h}$ defined in (2.17)-(2.18) with the bond angle $\alpha = 103°$. The spinless TB models (2.30) and (2.31), along with (2.9), will be used in chapter 3 to study weak inter-orbital Coulomb repulsion in chalcogen chains. Reasons for neglecting spin in this setting are given in chapter 3.

2.3.2 Spinfull chalcogen chain and spin-orbit coupling

In the absence of SOC, adding spin to the spinless chalcogen chain model (2.31), amounts to simply considering two copies of the same model, one for each spin channel. With SOC, however, the problem becomes more complicated. In the GO basis (see Sec. 2.2.2) the SOC Hamiltonian of the chalcogen chain at 2/3 filling is

$$\mathbf{H}_{\lambda} = -\lambda \sum_{j} \sum_{m} \vec{\mathbf{C}}_{j}^{\dagger} \, s_m \otimes l_m \, \vec{\mathbf{C}}_{j}. \tag{2.32}$$

In the above

$$\vec{\mathbf{C}}_{j} = \left(\mathbf{c}_{jx\uparrow}, \mathbf{c}_{jy\uparrow}, ..., \mathbf{c}_{jx\downarrow}, ... \right), \tag{2.33}$$

where $\mathbf{c}_{j\mu\sigma}$ is the annihilation operator of an electron on site j, orbital p_μ and with spin σ. s_m, $m = x, y, z$ is the $m - th$ component of the spin operator, given by

$$s_m = \frac{1}{2}\sigma_m, \tag{2.34}$$

where σ_m is the Pauli matrix with index $m = x, y, z$. Finally, l_m, $m = x, y, z$ is the $m - th$ component of the angular momentum operator (2.5).

In the spinless model, in the LO basis (2.27) the orbital basis on site j is rotated by an angle dependent on j. In order for the SOC Hamiltonian (2.32) to be invariant with respect to the global to local basis transformation – and therefore site-independent – (2.27) has to be generalised to include spin. More concretely, the orbital rotation needs to be accompanied by a spin rotation by an angle ϕ – whose magnitude will be determined shortly – around the helical axis $\vec{h}$, resulting in a generalization of the global to local orbital basis change (2.27) to the spinfull case

$$\vec{\mathbf{C}}'_j = \left(U(\vec{h}, \phi)^j \otimes O(\vec{h}, 120^\circ)^j\right) \vec{\mathbf{C}}_j, \tag{2.35}$$

where $U(\vec{h}, \phi)$ is a spin rotation by an angle ϕ around the helical axis $\vec{h}$. Spin rotations are constructed the same way as orbital rotations, using generators. The generators of spin rotations are the spin operators s_x, s_y, s_z (2.34). A spin rotation by angle ϕ around the axis $\vec{h}$ is given by the exponential map

$$U(\phi, \vec{v}) = e^{i\vec{h}\cdot\vec{s}\phi}, \tag{2.36}$$

where

$$\vec{s} = (s_x, s_y, s_z). \tag{2.37}$$

Similarly, the GP basis (2.26) becomes

$$\vec{\mathbf{C}}_Q = \frac{1}{\sqrt{N}} \sum_j e^{ijaQ} \left(U(\vec{h}, \phi)^j \otimes O(\vec{h}, 120^\circ)^j\right) \vec{\mathbf{C}}_j. \tag{2.38}$$

For spin rotations, for any $\vec{n}$,

$$U(\vec{h}, \phi)^\dagger \vec{n} \cdot \vec{s} U(\vec{h}, \phi) = \left(O(\vec{h}, \phi) \cdot \vec{n}\right) \cdot \vec{s}, \tag{2.39}$$

where $O(\phi, \vec{h})$ is the standard, Euclidean rotation matrix (2.6). At the same time, for p-orbital rotations, for any $\vec{n}$

$$O(120^\circ, \vec{h})^\dagger \vec{n} \cdot \vec{l} O(\vec{h}, 120^\circ) = \left(O(\vec{h}, 120^\circ) \cdot \vec{n}\right) \cdot \vec{l}. \tag{2.40}$$

Consequently, in order for the SOC Hamiltonian (2.32) to be invariant with respect to the global-to-local basis transformation (2.44), the angle ϕ needs to satisfy two conditions:

$$\begin{aligned} &1. \quad \left(O(\vec{h}, 120^\circ) \cdot \vec{s}\right) \cdot \left(O(\vec{h}, \phi) \cdot \vec{l}\right) = \vec{s} \cdot \vec{l}, \\ &2. \quad U(\vec{h}, \phi)^3 = \mathbb{1}_2. \end{aligned} \tag{2.41}$$

The first condition implies that

$$O(\vec{h}, 120^\circ)^T \cdot O(\vec{h}, \phi) = \mathbb{1}_3, \tag{2.42}$$

the second condition implies that

$$3\phi = 0 \bmod 720^\circ, \tag{2.43}$$

as $U(\phi, \vec{h})$ is a spin rotation.

The solution is $\phi = 480^\circ$. Thus, defining the spinfull global-to-local basis transformation as

$$\vec{\mathbf{C}}'_j = \left(U(\vec{h}, 480^\circ)^j \otimes O(\vec{h}, 120^\circ)^j\right) \vec{\mathbf{C}}_j \tag{2.44}$$

and the spinfull GP basis as

$$\vec{\mathbf{C}}_Q = \frac{1}{\sqrt{N}} \sum_j e^{ijaQ} \left(U(\vec{h}, 480^\circ)^j \otimes O(\vec{h}, 120^\circ)^j\right) \vec{\mathbf{C}}_j, \tag{2.45}$$

one can write the spinfull, non-interacting chalcogen chain Hamiltonian in the GP basis

$$\begin{aligned}\mathbf{H}_{\text{scc}} &= \tilde{\mathbf{H}}_{\text{chalc.}} + \mathbf{H}_\lambda \\ &= \sum_Q \left[e^{iQa} \vec{\mathbf{C}}_Q^\dagger \left(U(\vec{h}, 480^\circ) \otimes O(\vec{h}, 120^\circ)\right)^\dagger K \vec{\mathbf{C}}_Q + \text{h.c.}\right] - \lambda \sum_Q \sum_m \vec{\mathbf{C}}_Q^\dagger \, s_m \otimes l_m \, \vec{\mathbf{C}}_Q,\end{aligned} \tag{2.46}$$

where the TB Hamiltonian

$$\tilde{\mathbf{H}}_{\text{chalc.}} = \sum_Q \left[e^{iQa} \vec{\mathbf{C}}_Q^\dagger \left(U(\vec{h}, 480^\circ) \otimes O(\vec{h}, 120^\circ)\right)^\dagger K \vec{\mathbf{C}}_Q + \text{h.c.}\right] \tag{2.47}$$

is the spinfull analogue of (2.30). In real space and in the GO basis the Hamiltonian $\mathbf{H}_{\text{scc}}$ takes the form

$$\begin{aligned}\mathbf{H}_{\text{scc}} &= \tilde{\mathbf{H}}_{\text{chalc.}} + \mathbf{H}_\lambda \\ &= \sum\nolimits_j \Bigg[\vec{\mathbf{C}}_{j+1}^\dagger \left(U(\vec{h}, 480^\circ)^j \otimes O(\vec{h}, 120^\circ)^j\right)^\dagger K \left(U(\vec{h}, 480^\circ)^j \otimes O(\vec{h}, 120^\circ)^j\right) \vec{\mathbf{C}}_j \\ &\quad + \text{h.c.}\Bigg] - \lambda \sum_j \sum_m \vec{\mathbf{C}}_j^\dagger \, s_m \otimes l_m \, \vec{\mathbf{C}}_j.\end{aligned} \tag{2.48}$$

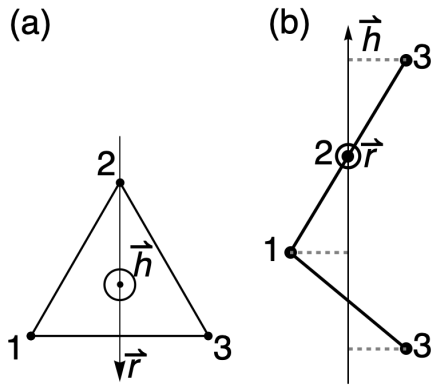

Figure 2.6: The chalcogen chain, (a) top view and (b) side view. Equivalent atoms in the chalcogen chain are marked by the same numbers. In the top view, all sites in the helical chain collapse onto the vertices of an equilateral triangle, with equivalent sites collapsing on the same vertex. Marked: helical axis $\vec{h}$, rotation axis $\vec{r}$ (see text for description).

The non-interacting Hamiltonians (2.46) and (2.48) will be used in chapter 5 to study the topology of chalcogen chains. Neglecting the weak Coulomb interactions in chalcogen chains is a reasonable assumption, as I will show in chapter 3. It is also common practice [24, 25, 30].

2.3.3 Crystalline symmetry of the chalcogen chain

For chains the number of crystalline symmetries is limited. Amongst rotation symmetries, only a 180-degree rotation symmetry $\mathcal{R}_\pi$ is possible. For mirror symmetries, there is only one mirror plane – perpendicular to the chain – and the corresponding symmetry operation $\mathcal{M}$. The final possible symmetry is inversion $\mathcal{I}$.

From Fig. 2.1 it is clear that neither $\mathcal{I}$, nor $\mathcal{M}$ applies to a helix. This is because both inversion and mirror reflection give a helix of opposite handedness – the helical angle β is mapped to $-\beta$. $\mathcal{R}_\pi$, however, is a symmetry of any helix. In Fig. 2.6 I show the top and side view of the chalcogen chain. I also mark the $\mathcal{R}_\pi$ rotation axis

$\vec{r}$. Note that while for a periodic chain the choice of $\vec{r}$ is ambiguous, for a finite, open chain $\vec{r}$ is unique – it has to go through the middle of the chain. If the length of the chain N is odd, $\vec{r}$ goes through one of the atoms. If N is even it goes through the middle of one of the bonds.

In the GO basis defined in Sec. 2.2.2 and with the rotation axis $\vec{r}$ going through the zeroth site, one finds that

$$\vec{r} = \vec{a} \tag{2.49}$$

with $\vec{a}$ defined in (2.18). Using (2.18) and (2.49) one can find the expression for the 180-degree rotation symmetry operation in the GO basis

$$\mathcal{R}_\pi = \sum_j \vec{\mathbf{c}}^\dagger_{-j} U(\vec{r}, 180^\circ) \otimes O(\vec{r}, 180^\circ) \vec{\mathbf{c}}_j. \tag{2.50}$$

with

$$O(\vec{r}, 180^\circ) = O\left(\vec{z}, 180^\circ - \frac{\alpha}{2}\right)^T O\left(\vec{x}, 180^\circ\right) O\left(\vec{z}, 180^\circ - \frac{\alpha}{2}\right) \tag{2.51}$$

and

$$U(\vec{r}, 180^\circ) = U\left(\vec{z}, 180^\circ - \frac{\alpha}{2}\right)^\dagger U\left(\vec{x}, 180^\circ\right) U\left(\vec{z}, 180^\circ - \frac{\alpha}{2}\right) \tag{2.52}$$

2.3.4 The $\alpha = 90^\circ$ chalcogen chain – the cubic limit

An important special case for a period-three helical chain is when the bond angle is $\alpha = 90^\circ$. I call this the cubic chain model, as opposed to the chalcogen chain model for $\alpha = 103^\circ$. I neglect spin (see chapter 5 for more details). In the cubic chain model the chain can be immersed in a simple cubic lattice (see Fig. 2.7). This leads to extra symmetries, which significantly simplify the Hamiltonian. One finds that the helical axis $\vec{h}$ (2.17) becomes

$$\vec{h} = \frac{1}{\sqrt{3}}(1, 1, 1), \tag{2.53}$$

which leads to

$$O(\vec{h}, 120^\circ) = \begin{pmatrix} 0 & 0 & 1 \\ 1 & 0 & 0 \\ 0 & 1 & 0 \end{pmatrix}. \tag{2.54}$$

For a spinless cubic chain the real space Hamiltonian is

$$\mathbf{H}_{\text{cubic}} = \sum_j \vec{\mathbf{c}}^\dagger_{j+1} K_j \vec{\mathbf{c}}_j + \text{h.c.}, \tag{2.55}$$

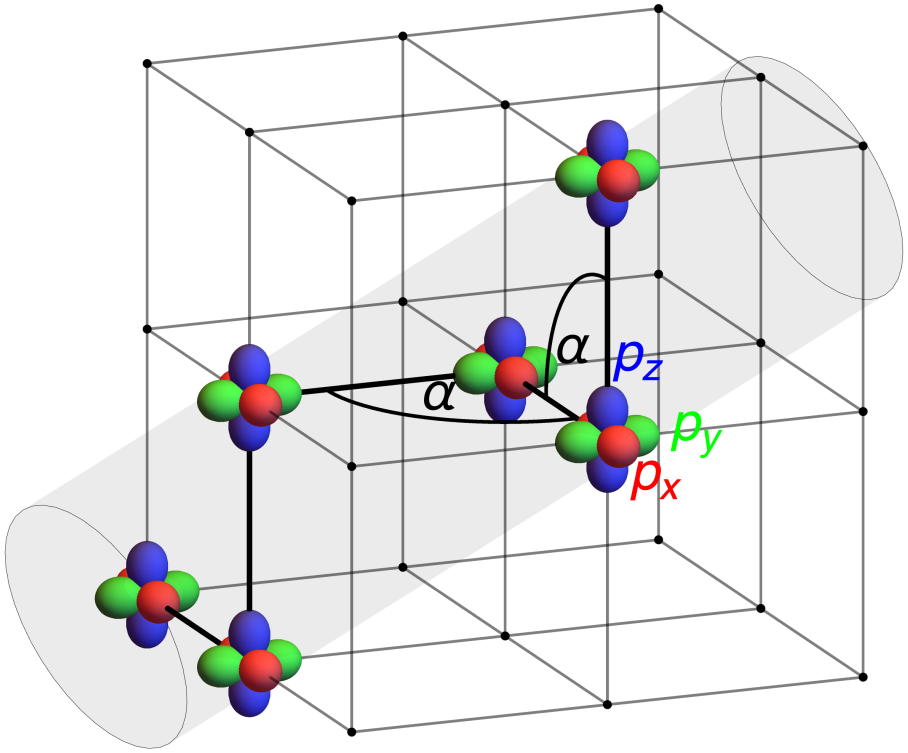

Figure 2.7: The cubic chain, distinguished from the chalcogen chain by a different bond angle, which for the cubic chain is $\alpha = 90°$. The cubic chain can be immersed in a simple cubic, three-dimensional lattice, marked in the plot by thin, gray lines. The cubic chain bonds are marked by thick black lines. The p-orbitals of the GO basis of Sec. 2.2.2 (see Fig. 2.2) are also shown, with p_x, p_y and p_z orbitals coloured red, green and blue respectively. For a cubic chain, each basis vector of the GO basis is parallel to one of the bonds in the chain. All sites in the cubic chain lie on the wall of the shaded gray cylinder.

where

$$K_j = \begin{cases} \begin{pmatrix} t_\sigma & 0 & 0 \\ 0 & t_\pi & 0 \\ 0 & 0 & t_\pi \end{pmatrix} & j = 0 \bmod 3 \\ \begin{pmatrix} t_\pi & 0 & 0 \\ 0 & t_\pi & 0 \\ 0 & 0 & t_\sigma \end{pmatrix} & j = 1 \bmod 3 \\ \begin{pmatrix} t_\pi & 0 & 0 \\ 0 & t_\sigma & 0 \\ 0 & 0 & t_\pi \end{pmatrix} & j = 2 \bmod 3 \end{cases} \tag{2.56}$$

Chapter 3

Orbital density waves in chalcogen chains

This chapter is based on a 2021 article titled *'Chalcogenic orbital density waves in the weak- and strong-coupling limit'*, published in *Physical Review B 103, 235123* [32].

Elemental chalcogens, selenium and tellurium, are known to crystallise in a trigonal structure which can be described as a collection of parallel, helical chains arranged on a two-dimensional, hexagonal lattice (see chapter 2, in particular Fig. 2.5, for a more detailed description). These helical chains, which in this thesis I call chalcogen chains, exhibit a relatively exotic, orbitally-ordered ground state, called an ODW [36]. An ODW is an arrangement of electrons in a crystal lattice in which the total charge is the same on each lattice site, however, the orbital polarisation differs from site to site resulting in a non-trivial, ordered state. ODWs are currently suspected to exist in just a handful of materials other than elemental selenium and tellurium, two examples are the compounds 1T-$TiSe_2$ and 2H-TaS_2 [39, 40].

The ODW ground state of the non-interacting chalcogen chain is described in Sec. 3.2. It can be seen as a fixed (site-independent) distribution of two electrons between three p orbitals per site, with the inter-site modulation represented by a $\beta = 120^\circ$ rotation of the charge distribution around the helical chain axis $\vec{h}$, see Fig. 3.4. The fixed charge distribution is the following: one electron occupies the p_z orbital (normal to the bond-angle plane) of the LO basis, while the other electron is distributed equally between the other two p orbitals, lying in the bond-angle plane (see Fig. 3.1 and 3.4).

The origin of this exotic ground state in elemental chalcogens is the helical geometry in conjunction with the p^4 valence configuration. This is in contrast with other

types of periodic modulations found in chains. For instance, Charge Density Waves (CDWs) and spin density waves (SDWs) found in the one-dimensional, extended Hubbard model come about due to Coulomb interactions [41–43]. There, arbitrarily small Coulomb repulsion at special fillings leads to a nesting instability, giving rise to a periodic distortion, resulting in charge or spin order. In selenium and tellurium no interaction is needed to stabilise the periodically-modulated orbital order – it results from the chain geometry and anisotropic hopping in the p sub-shell alone.

In 2018 [28] it was theorised that the trigonal structure of elemental selenium and tellurium crystals is a deformation of a hypothetical simple cubic lattice (see Fig. 2.5), which is the crystal structure of the next element in the chalcogen group (group 16 of the periodic table), polonium, the only known element to crystallise in a simple cubic lattice under ambient conditions. The authors of [28] argue that, in selenium and tellurium, the deformation towards the trigonal lattice is brought about by the onset of very weak inter-orbital Coulomb repulsion. The mechanism of this deformation is the following. First, in the initial simple cubic lattice each p_μ orbital is aligned with a single cubic direction, $\mu = x, y, z$. This alignment triggers a Peierls-type transition in all the "straight" chains within the simple cubic structure, that is the shortening of every third bond in each of the three cubic directions. Second, these alternating short-long-long bond patterns in all three cubic directions are locked in phase by a very weak inter-orbital Coulomb repulsion [see Fig. 2.5 (b)]. Note that this mechanism does not involve spin, which is why in this chapter I consider spinless chalcogen chains.

The scenario described above, however, presents a conundrum. As I have mentioned above, it is known that in the one-dimensional, extended Hubbard model infinitesimally weak Coulomb repulsion brings about a structural phase transition. The chalcogen chain is likewise a one-dimensional system, described by a one-dimensional Hubbard model. While it is known that the non-interacting ODW ground state of selenium and tellurium is compatible with the trigonal structure [24, 26], and therefore with the deformation proposed in [28], will the addition of weak, inter-orbital Coulomb repulsion not bring about an instability, yielding a different ground state? In other words, there exists a possible inconsistency between the following two facts. On the one hand, one needs to consider inter-orbital Coulomb repulsion in order to explain the deformation from the hypothetical simple cubic to the actual trigonal crystal structure in selenium and tellurium, proposed in [28]. On the other hand, the inclusion of inter-orbital Coulomb repulsion in the chalcogen chain model introduces a distinct possibility of a phase transition from the non-interacting ODW ground state to a different, unobserved ground state in selenium and tellurium chains, possibly

incompatible with the trigonal structure.

With this in mind, in this chapter I look for the ground state a spinless chalcogen chain model with inter-orbital Coulomb repulsion. In particular, I investigate how robust the non-interacting ground state is with respect to the increasing strength of Coulomb interaction, if and when a phase transition to a different ground state occurs, and what is the nature of this new ground state.

To this end, in Sec. 3.1 I formulate the model of a spinless chalcogen chain with inter-orbital Coulomb interaction, based on the general tight-binding model of a chalcogen chain already discussed in Sec. 2.

In Sec. 3.2 I describe the electronic structure of the non-interacting, spinless chalcogen chain. The section is structured in the following way. In Sec. 3.2.1 I provide a simplified, linearised Hamiltonian of such a chain, that is model (2.30) linearised around the bond angle $\alpha = 90°$. This is done in order to make the numerical calculations tractable. In Sec. 3.2.2 I show the band structure of the non-interacting, spinless chalcogen chain, both for the linearised model of Sec. 3.2.1 and the full model (2.30) and in both the single-atom unit cell and downfolded to a period-three unit cell of the helical chain in the GO basis (see Fig. 2.3). This is done in order to (i) show the gapped nature of the ground state and (ii) show that the linearised model is a good approximation. In Sec. 3.2.3 I further analyse the ground state, providing a characterisation of each band in terms of orbital polarisation as well as showing a schematic picture of the ODW ground state of the non-interacting chalcogen chain (Fig. 3.4).

Sec. 3.3 describes a mean-field Hartree solution of the interacting chalcogen chain model. In particular, in Sec. 3.3.1 and Sec. 3.3.2 I perform a mean-field decoupling of the interacting model using the Hartree method. In Sec. 3.3.3 I present the fixed points of the Hartree method, representing self-consistent mean-field solutions of the interacting chalcogen chain, and identify the ground state. Then, in Sec. 3.3.4, I describe the evolution of the ground-state orbital density with increasing Coulomb interaction strength, identifying two distinct ODW phases separated by a phase transition. Finally, in Sec. 3.3.5 I compare the two ODW phases.

Sec. 3.4 corroborates the results of Sec. 3.3 by providing DMRG results on a finite, open chalcogen chain with inter-orbital Coulomb interactions. It is subdivided into the following subsections. In Sec. 3.4.1 I provide the motivation for performing this calculation in addition to the mean-field calculation of Sec. 3.3 by comparing the two methods. In Sec. 3.4.2 I characterise the DMRG method and in Sec. 3.4.3 I provide the results of the DMRG calculations.

Finally, Sec. 3.5 concludes this chapter. In Sec. 3.5.1 I present a summary of

results presented in this chapter and reiterate key conclusions. Sec. 3.5.2 contains some concluding remarks.

3.1 Model

The first step in dealing with the challenge I set myself in this chapter is to formulate a tight-binding model of a chalcogen chain. Since the pre-eminent goal is to establish whether the mechanism of crystal structure deformation, proposed in [28] and discussed above, which postulates a simple cubic to trigonal distortion as a result of inter-orbital Coulomb repulsion in a spinless model (see introduction to this chapter), I will consider a spinless chalcogen chain.

The tight-binding Hamiltonian of a non-interacting, spinless chalcogen chain is given in Sec. 2.3.1, both in the GP basis (2.26), with the Hamiltonian (2.30), and in real space, in the GO basis (see Sec. 2.2.2), with the Hamiltionian (2.31). Since the goal is to establish whether the ground state of the non-interacting chalcogen chain is robust in the presence of relatively weak inter-orbital Coulomb repulsion, I will additionally consider the inter-orbital Coulomb repulsion term in the tight binding Hamiltonian. Such a term is always present in any multi-orbital system, but often neglected. The inter-orbital Coulomb repulsion Hamiltonian for p orbitals is given in (2.9). Note that this Hamiltonian is the same in both the LO and the GO basis, as the relation between the two bases is simply an orbital rotation [see (2.27)], with respect to which the Coulomb term is invariant.

Altogether, following chapter 2 and the arguments above, the general, real-space, GO-basis Hamiltonian of a spinless chalcogen chain with inter-orbital Coulomb interaction reads

$$\begin{aligned}\mathbf{H}_{\text{cc}} &= \mathbf{H}_{\text{chalc.}} + \mathbf{H}_{\text{Coul.}} \\ &= \sum_j \left[\vec{\mathbf{c}}^{\dagger}_{j+1} \left(O(\vec{h}, 120^\circ)^j \right)^{\dagger} K O(\vec{h}, 120^\circ)^j \vec{\mathbf{c}}_j + \text{h.c.} \right] + \sum_j \sum_{\mu,\nu=x,y,z} U \mathbf{n}_{j\mu} \mathbf{n}_{j\nu},\end{aligned} \tag{3.1}$$

where the tunnelling matrix K and the helix axis vector $\vec{h}$ depend on the choice of the p-orbital basis and will be specified in the next section. The TB Hamiltonian $\mathbf{H}_{\text{chalc.}}$ is defined in (2.30), while the inter-orbital Coulomb term $\mathbf{H}_{\text{Coul.}}$ is defined in (2.9). For chalcogen chains $U/t_\sigma \approx 0.24$ [41–43].

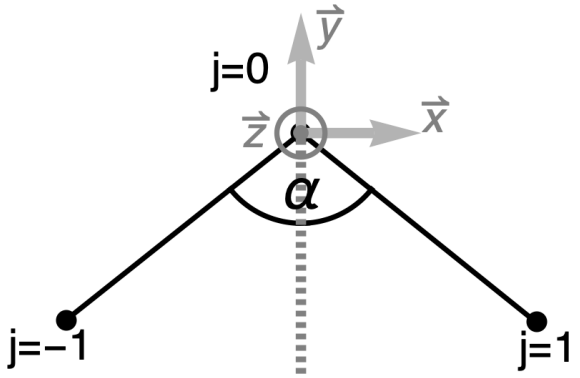

Figure 3.1: The $\vec{x}, \vec{y}, \vec{z}$ basis vectors of the alternate p-orbital basis defined in this section. The figure is drawn in the plane defined by three sites, in this case $j = -1, 0, 1$, called the bond angle plane. The basis vectors are shown in relation to the bond angle α (see Fig. 2.1). The sites with $j = -1, 0, 1$ are chosen because the basis is defined with respect to the bond joining sites with $j = 0$ and $j = 1$ (see Sec. 2.2.2).

3.2 Non-interacting chalcogen chain

I will begin by looking at the non-interacting chalcogen chain, that is model (3.1) with $U = 0$

$$\mathbf{H}_{\text{cc}}\big|_{U=0} = \sum_j \left[\vec{\mathbf{c}}_{j+1}^{\dagger} \left(O(\vec{h}, 120°)^j \right)^{\dagger} K O(\vec{h}, 120°)^j \vec{\mathbf{c}}_j + \text{h.c.} \right]. \tag{3.2}$$

The reasoning behind this approach is to first build an understanding of the behaviour of electrons in a helix and find the ground state of the non-interacting model, which will later allow me to build a low-energy theory around that ground state.

3.2.1 Linearised bond angle dependence

As discussed in Sec. 2.2.3 one can use the generalised Bloch theorem and go to the GP basis (2.26), in which the Hamiltonian (3.2) takes the form

$$\mathbf{H}_{\text{cc}}\big|_{U=0} = \sum_Q \left[e^{iQa} \vec{\mathbf{c}}_Q^{\dagger} O(\vec{h}, 120°)^{\dagger} K \vec{\mathbf{c}}_Q + \text{h.c.} \right]. \tag{3.3}$$

The dependence of the Hamiltonian (3.3) on the helix geometry is encoded in the tunnelling matrix K and the rotation matrix $O(\vec{h}, 120°)$, which is a relatively complex

function of the helix bond angle α, namely

$$O(\vec{h}, 120^\circ) = e^{i\vec{h}\cdot\vec{l}\theta}, \tag{3.4}$$

where $\vec{h}$ is the helix axis vector and θ is given by (2.19). For numerical calculations It is desirable to simplify the Hamiltonian (3.3) by approximating (3.4) by a simpler expression. (3.4) takes a particularly simple form for the bond angle $\alpha = 90^\circ$ (see Sec. 2.3.4). For small deviations from the bond angle $\alpha = 90^\circ$ one can exploit this fact and take the Taylor series of (3.4)

$$O(\vec{h}, 120^\circ) = O(\vec{h}, 120^\circ)\big|_{\alpha=90^\circ} + \left[\frac{d}{d\alpha}O(\vec{h}, 120^\circ)\right]\Bigg|_{\alpha=90^\circ} \epsilon + O(\epsilon^2) \tag{3.5}$$

using the deviation of the bond angle from $\alpha = 90^\circ$

$$\epsilon = \alpha - 90^\circ, \tag{3.6}$$

expressed in radians, as a small parameter and keeping only terms at most linear in ϵ.

The expansion (3.5) will, however, depend on the p-orbital basis choice. So will its convergence. The GO basis defined ins Sec. 2.2.2, Fig. 2.2, while very convenient for the purposes of the rest of this thesis, is not a good setting for such an expansion. Taking the expansion (3.5) in this basis and using the chalcogen value of $\epsilon = 13/180\pi$, one finds that even if one includes terms up to order 2 in ϵ one does not obtain a band structure which is comparable with that of the full model, given by (3.3). In this section, therefore, I will use a different basis.

The basis I choose is one rotated with respect to the basis of Sec. 2.2.2, Fig. 2.2 by the angle

$$\gamma = 90^\circ - \alpha/2 \tag{3.7}$$

around the $\vec{z}$ axis. I will call this basis the *alternative* global orbital (AGO) basis. This basis is shown in Fig. 3.1. Its relation with the bases introduced in chapter 2 is shown in Fig. 3.2.

In the AGO basis

$$K = \begin{pmatrix} t_\sigma \cos^2\gamma + t_\pi \sin^2\gamma & (-t_\sigma + t_\pi)\sin\gamma\cos\gamma & 0 \\ (-t_\sigma + t_\pi)\sin\gamma\cos\gamma & t_\sigma \sin^2\gamma + t_\pi \cos^2\gamma & 0 \\ 0 & 0 & t_\pi \end{pmatrix}, \tag{3.8}$$

with

$$\gamma = 90^\circ - \frac{\alpha}{2} \tag{3.9}$$

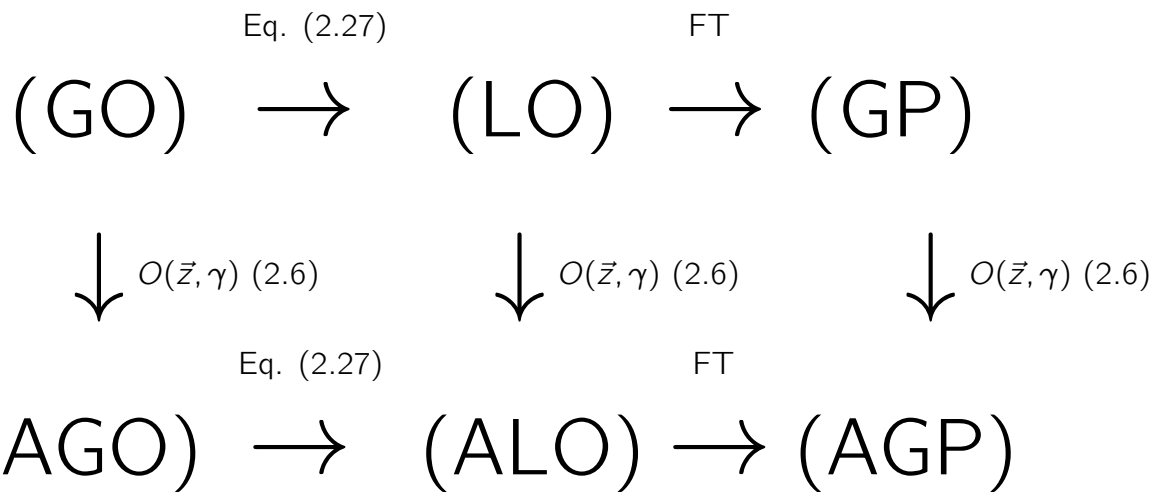

Figure 3.2: The relation between the various bases used in this and the previous chapter. The bases are: the global orbital basis (GO), the local orbital basis (LO) and the general pseudo-momentum basis (GP), the alternative global orbital basis (AGO), the alternative local orbital basis (ALO) and the alternative generalised pseudo-momentum basis (AGP). The superscripts above the arrows indicate the transformations which map each basis onto the next. FT stands for discrete Fourier transform (2.21), γ is given by (3.7). Only the mapping in one direction is shown, although all the mappings are bijective.

and

$$\vec{h} = O\left(\vec{y},\theta\right)\cdot\vec{z} = \left(\sin\theta, 0, \cos\theta\right), \tag{3.10}$$

with θ, as before, given by (2.19). The Taylor expansion of the tunnelling matrix on the ALO orbital basis, up to terms linear in ϵ, is

$$O(\vec{h},120^\circ)^\dagger K \approx T = \frac{1}{2}\begin{pmatrix} (1+\epsilon)\,t_\sigma + \epsilon\,t_\pi & t_\sigma - \epsilon\,t_\pi & \frac{2-\epsilon}{\sqrt{2}}\,t_\pi \\ -\,t_\sigma + \epsilon\,t_\pi & (-1+\epsilon)\,t_\sigma - \epsilon\,t_\pi & \frac{2+\epsilon}{\sqrt{2}}\,t_\pi \\ \frac{2-\epsilon}{\sqrt{2}}\,t_\pi & -\frac{2+\epsilon}{\sqrt{2}}\,t_\pi & -2\epsilon\,t_\pi \end{pmatrix}, \tag{3.11}$$

while the linearised Hamiltonian is

$$\mathbf{H}_{\mathrm{cc}}\big|_{U=0} \approx \mathbf{H}_0 = \sum_Q \left[e^{iQa}\vec{\mathbf{c}}_Q^\dagger T\vec{\mathbf{c}}_Q + \mathrm{h.c.}\right]. \tag{3.12}$$

The ratio of tunnelling amplitudes for chalcogens is $t_\pi/t_\sigma = -1/3$.

3.2.2 Band structure

The band structure of the linearised, non-interacting chalcogen chain model (3.12) and the full, non-interacting chalcogen chain model (3.3) is shown in Fig. 3.3. The linearised model captures the band structure of the full model remarkably well. The band structure consists of three bands, which can be downfolded to form nine bands in the fundamental three-atom unit cell of the helix. The bands are separated from one another by substantial gaps. At 2/3 filling, the two bottom bands are occupied and the Fermi level lies within the upper gap. The ground state of a chalcogen chain is therefore insulating.

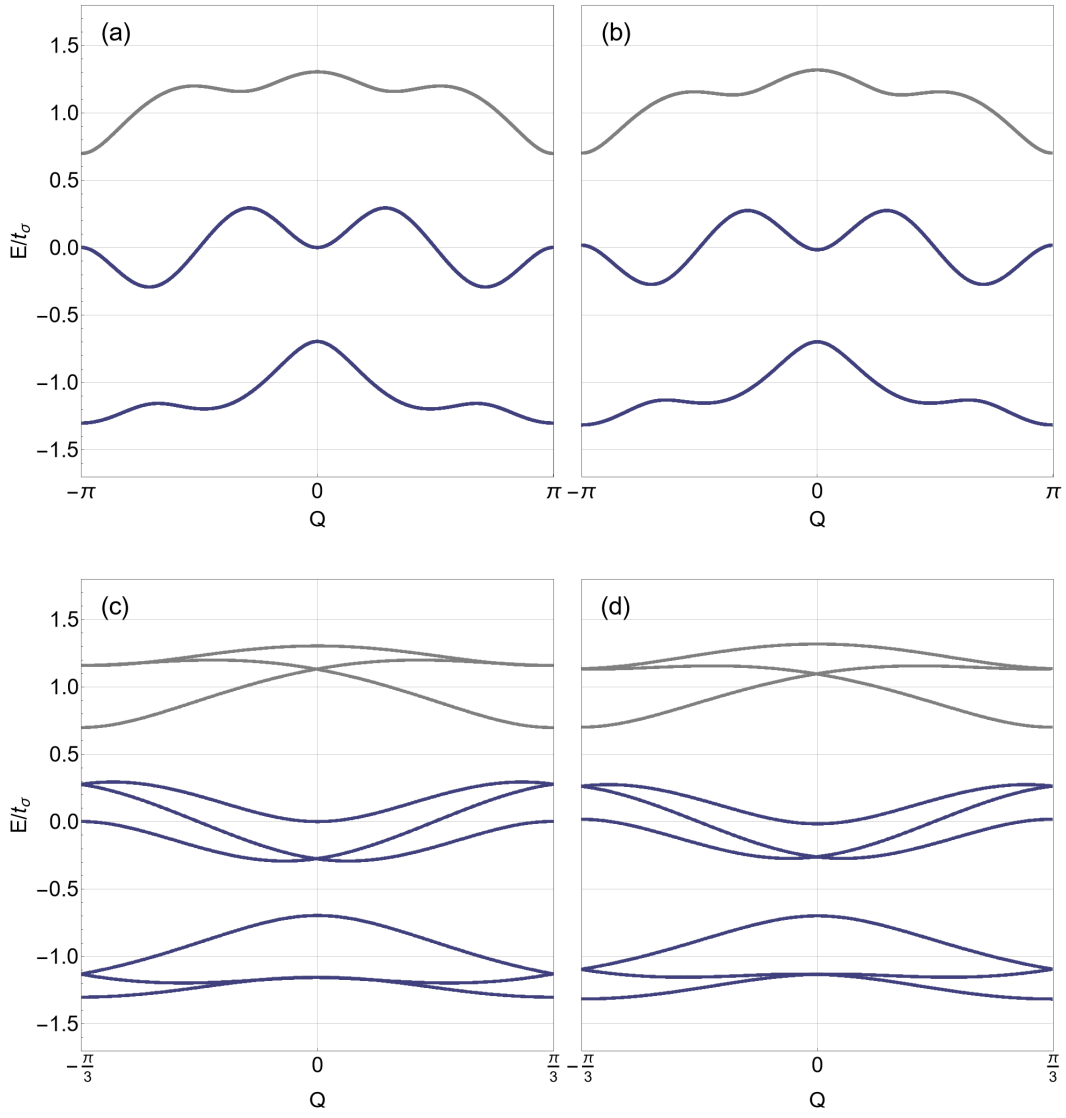

Figure 3.3: Band structure of the non-interacting chalcogen chain. (a) The linearised model (3.12), fundamental unit-cell. (b) Full model (3.3), fundamental unit cell. (c) The linearised model (3.12), downfolded to the three-site unit cell of the helix. (d) Full model (3.3), downfolded to the three-site unit cell of the helix. The parameters used in all plots are: $t_\pi/t_\sigma = -1/3$ and $\alpha = 103^\circ$ ($\epsilon = 13^\circ$). The occupied bands are coloured blue, the empty bands are coloured gray. The linearised model (3.12) captures the band structure of the full model (3.3) remarkably well. The substantial insulating gap is clearly visible in both models.

bond angle	$\alpha = 90^\circ$			$\alpha = 103^\circ$		
orbital / band	p_x	p_y	p_z	p_x	p_y	p_z
top band	0.4593	0.4609	0.0798	0.4595	0.4600	0.0805
middle band	0.0800	0.0798	0.8402	0.0796	0.0817	0.8387
bottom band	0.4607	0.4593	0.0800	0.4609	0.4583	0.0808

Table 3.1: The orbital character of each of the three bands, averaged over q, for the cubic chain model (2.55)-(2.56) (chalcogen chain model with $\alpha = 90^\circ$) and the linearised chalcogen chain model (3.12) with $\alpha = 103^\circ$ ($\epsilon = 13^\circ$), in the local orbital basis (2.27). The values in the table were obtained for the chalcogen chain tunnelling amplitudes $t_\pi/t_\sigma = -1/3$.

3.2.3 Ground state

To better understand the ground state of the non-interacting chalcogen chain (3.3) it is essential to know the orbital character of each of the three bands, which enables one to visualise the orbital density in real space. The model in the ALO basis (see Fig. 3.2) is a period-one chain, therefore the orbital occupation in the ALO basis is the same on every site. The orbital character of each band for both $\alpha = 103^\circ$ ($\epsilon = 13^\circ$) and the more symmetric case of $\alpha = 90^\circ$ (cubic chain model) is shown in Tab.3.1. The middle band is dominated by the p_z orbital, which is the orbital normal to the bond angle plane in the ALO basis, while the top and bottom band are formed predominantly by the orbitals in the bond angle plane. In the literature the top and bottom bands are often called the $\sigma^\pm$ bands, while the middle band is often called the lone pair (LP) band [30].

As seen in Tab. 3.1, the bands of the chalcogen chain are orbitally polarised. In the ALO basis the orbital polarization is constant along the chain, with one of the two electrons per site occupying the p_z orbital and the other electron distributed equally between the p_x and p_y orbitals. In the AGO basis (see Fig. 3.1) this translates to a helical pattern of orbital polarisation, whereby the orbital pattern twists, following the screw-axis of the helix, which is schematically shown in Fig. 3.4. I will call this ODW the '2-1-1' ODW, because the charge density on one orbital is twice that on each of the other two orbitals.

This concludes the discussion of the non-interacting chalcogen chain. Presently, I will move to discuss the interacting chalcogen chain and its solution in the mean-field approximation.

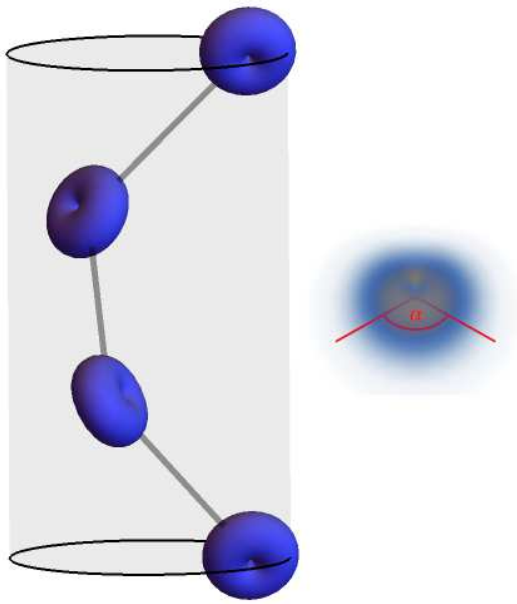

Figure 3.4: The '2-1-1' ODW ground state of the non-interacting chalcogen chain. The hole orbital density is shown. The orbital density is represented schematically in blue, showing the ground-state distribution of the hole in the local p-orbital basis (see Fig. 3.1). On each site the local p_z orbital, normal to the bond angle plane, is fully occupied by one electron. The single hole per site (2/3 filling) is equally distributed between the two p-orbitals in the bond angle plane, resulting in a doughnut-like shape. The inset shows the charge distribution of the hole in relation to the bond angle α.

3.3 Hartree solution

Model (3.1) is impossible to solve exactly for long chains, as it is an interacting model and its Hilbert space dimension grows exponentially with system size for a fixed filling. However, one can treat it approximately. One way is to perform a mean-field decoupling following the so-called Hartree method [44].

3.3.1 Mean-field decoupling

The Hartree method approximates an operator by its ground-state expectation value

$$\mathbf{n}_{j\mu} \to \bar{n}_{j\mu} \tag{3.13}$$

and true eigenstates of the system by product states. When looking for the ground state alone this approximation is valid whenever one can assume that

$$\forall\mu\forall j\ \mathbf{n}_{j\mu}\left|\psi_{\mathrm{GS}}\right\rangle \approx \bar{n}_{j\mu}\left|\psi_{\mathrm{GS}}\right\rangle, \tag{3.14}$$

where $|\psi_{\mathrm{GS}}\rangle$ is the ground state of the system. In other words, whenever the ground state is an approximate eigenstate of all the number operators $\mathbf{n}_{j\mu}$, corresponding to the eigenvalues $\bar{n}_{j\mu}$. The relation (3.14) becomes an equality for product states.

Using

$$\mathbf{\Delta}_{j\mu} \equiv \bar{n}_{j\mu} - \mathbf{n}_{j\mu}, \tag{3.15}$$

the inter-orbital Coulomb term (2.9) can be written as

$$\mathbf{H}_{\mathrm{Coul.}} = \sum_{j} \sum_{\substack{\mu,\nu=x,y,z \\ \mu\neq\nu}} U\left(-\bar{n}_{j\mu}\mathbf{\Delta}_{j\nu} - \bar{n}_{j\nu}\mathbf{\Delta}_{j\mu} + \bar{n}_{j\mu}\bar{n}_{j\nu} + O(\mathbf{\Delta})^2\right). \tag{3.16}$$

Thus, removing terms that are second order in $\mathbf{\Delta}_{j\mu}$, one obtains

$$\mathbf{H}_{\mathrm{Coul.}} \approx \sum_{j} \sum_{\mu,\nu=x,y,z} U\left(\bar{n}_{j\mu}\mathbf{n}_{j\nu} + \bar{n}_{j\nu}\mathbf{n}_{j\mu} - \bar{n}_{j\mu}\bar{n}_{j\nu}\right). \tag{3.17}$$

The Hamiltonian (3.17) is quadratic in creation/annihilation operators and can be easily diagonalised. It depends on $3N$ parameters $\bar{n}_{j\mu}$, $j = 1, ..., N$, $\mu = x, y, z$.

The model (3.1) after the mean field decoupling (3.17)

$$\begin{aligned}\mathbf{H}_{\mathrm{cc}} \approx \mathbf{H}_{\mathrm{HF}} = &\sum_{j}\left[\vec{\mathbf{c}}^{\dagger}_{j+1}\left(O(\vec{h},120^\circ)^{j}\right)^{\dagger} K O(\vec{h},120^\circ)^{j}\vec{\mathbf{c}}_{j} + \mathrm{h.c.}\right] \\ &+ \sum_{j}\sum_{\substack{\mu,\nu=x,y,z \\ \mu\neq\nu}} U\left(\bar{n}_{j\mu}\mathbf{n}_{j\nu} + \bar{n}_{j\nu}\mathbf{n}_{j\mu} - \bar{n}_{j\mu}\bar{n}_{j\nu}\right)\end{aligned} \tag{3.18}$$

has to be solved self-consistently, as the parameters $\bar{n}_{j\mu}$ represent electron densities which can be independently extracted once the ground state of (3.18) is known. The self-consistency condition is given by $3N$ equations

$$\left\langle\psi_0(\vec{\bar{n}})\right|\mathbf{n}_{j\mu}\left|\psi_0(\vec{\bar{n}})\right\rangle = \bar{n}_{j\mu}, \tag{3.19}$$

where $\vec{\bar{n}}$ holds the values of $3N$ parameters $\bar{n}_{j\mu}$, $j = 1, ..., N$, $\mu = x, y, z$

$$\vec{\bar{n}} = (\bar{n}_{0x}, \bar{n}_{0y}, \bar{n}_{0z}, \bar{n}_{1x}, ...) \tag{3.20}$$

and $\left|\psi_0(\vec{\bar{n}})\right\rangle$ is the ground state of (3.18) corresponding to the $3N$ parameters $\bar{n}_{j\mu}$.

Since (3.17) is invariant with respect to orbital rotations (a feature inherited from (2.9)), (3.18) can be mapped to a period-one chain (the ALO basis) and then represented in the AGP basis (see Fig. 3.2). In the AGP basis the Hamiltonian becomes

$$\begin{aligned}\mathbf{H}_{\mathrm{HF}} = &\sum_{Q} e^{iQa}\vec{\mathbf{c}}^{\dagger}_{Q} O(\vec{h}, 120^{\circ})^{\dagger} K \vec{\mathbf{c}}_{Q} + \\ &+ \sum_{Q,Q'} \sum_{\substack{\mu,\nu=x,y,z \\ \mu\neq\nu}} \frac{U}{\sqrt{N}} \Big[\mathcal{F}_{\bar{n}_{j\mu}}(Q-Q') \mathbf{c}^{\dagger}_{Q\nu} \mathbf{c}_{Q'\nu} + \mathcal{F}_{\bar{n}_{j\nu}}(Q-Q') \mathbf{c}^{\dagger}_{Q\mu} \mathbf{c}_{Q'\mu} + \\ &- \sqrt{N}\delta(Q+Q') \mathcal{F}_{\bar{n}_{j\mu}}(Q) \mathcal{F}_{\bar{n}_{j\nu}}(Q') \Big],\end{aligned} \tag{3.21}$$

where $\mathcal{F}_{\bar{n}_{j\mu}}(Q)$ is the discrete Fourier transform of $\bar{n}_{j\mu}$ at pseudo-momentum Q

$$\mathcal{F}_{\bar{n}_{j\mu}}(Q) = \frac{1}{\sqrt{N}} \sum_{j} e^{ijaQ} \bar{n}_{j\mu}, \tag{3.22}$$

where a is the inter-atomic distance in the chain.

3.3.2 Restricting the parameter space

Given the Hamiltonian (3.21) one has to assume something about the expected ground state and thereby restrict the huge parameter space, spanned by $3N$ parameters $n_{j\mu}$. Usually one has some idea of the phase transition which might occur in a given system for a physically reasonable Coulomb interaction strength U.

One may, for example, expect a structural instability. When a band crosses the Fermi surface at two different pseudo-momenta, at a distance $Q^{\star}$ from each other, this leads to possible tunnelling terms between electrons whose pseudo-momenta differ by $Q^{\star}$. These tunnelling terms occur between states whose energies are arbitrarily close to each other, which leads to a Fermi surface instability corresponding to a structural deformation whose period is $Q^{\star}/\pi$, even for negligibly small U. If that were the expected scenario, one would restrict the parameter space by requiring that $n_{j\mu}$ were sinusoidal, with period $Q^{\star}/\pi$. In the present case the structural instability is absent, as the Fermi surface is tangent to the middle band at a single point, $Q = \pi$, and there is a sizeable band gap (see Fig. 3.3).

If one does not expect a structural instability, one might still observe a phase transition to a state with the same period as the non-interacting ground state, but

whose other properties change. This would correspond to the ODW ground state of the chalcogen chain abruptly changing its orbital polarisation for some critical value of the Coulomb interaction parameter $U_{\text{crit.}}$. Because of the band gap one expects $U_{\text{crit.}}$ to be finite. Such a scenario will be investigated here.

To that end, one requires that

$$\bar{n}_{j\mu} \to \bar{n}_{\mu}, \tag{3.23}$$

that is that the orbital density remains constant along the chain (in the ALO basis!), which restricts the number of parameters to just three, namely $\bar{n}_x$, $\bar{n}_y$ and $\bar{n}_z$, with an additional constraint

$$\bar{n}_x + \bar{n}_y + \bar{n}_z = 2, \tag{3.24}$$

which is the consequence of the filling in the chain being 2/3. (3.23) leads to

$$\mathcal{F}_{\bar{n}_{j\mu}}(q) = \sqrt{N}\delta(q)\bar{n}_{\mu}, \tag{3.25}$$

and the Hamiltonian (3.21) becomes

$$\begin{aligned}\mathbf{H}_{\text{HF}} = \sum_{Q} e^{iQa}\vec{\mathbf{c}}_Q^{\dagger} O(\vec{h}, 120^{\circ})^{\dagger} K \vec{\mathbf{c}}_Q + \sum_{q} \sum_{\mu,\nu=x,y,z} U\left[\bar{n}_{\mu}\mathbf{n}_{q\nu} + \bar{n}_{\nu}\mathbf{n}_{q\mu}\right] + \\ - UN \sum_{\substack{\mu,\nu=x,y,z \\ \mu\neq\nu}} \bar{n}_{\mu}\bar{n}_{\nu}.\end{aligned} \tag{3.26}$$

Meanwhile, the linearised mean-field Hamiltonian is

$$\begin{aligned}\mathbf{H}_{\text{HF}} \approx \mathbf{H}_{\text{HF}}^{\text{lin.}} \equiv \mathbf{H}_{\text{MF}} = \sum_{Q} e^{iQa}\vec{\mathbf{c}}_Q^{\dagger} T \vec{\mathbf{c}}_Q + \sum_{q} \sum_{\substack{\mu,\nu=x,y,z \\ \mu\neq\nu}} U\left[\bar{n}_{\mu}\mathbf{n}_{q\nu} + \bar{n}_{\nu}\mathbf{n}_{q\mu}\right] + \\ - UN \sum_{\substack{\mu,\nu=x,y,z \\ \mu\neq\nu}} \bar{n}_{\mu}\bar{n}_{\nu},\end{aligned} \tag{3.27}$$

with T defined in (3.11). From now on, in studying the mean-field model, I will use (3.27) as it is simpler to deal with numerically and, as I have shown, it approximates the full Hamiltonian (3.26) well.

3.3.3 Hartree flow

The self-consistent nature of the solution to the Hartree problem (3.27) does not imply a self-consistent calculation. Instead, the solution can be found iteratively.

Consider the mean-field Hartree Hamiltonian (3.27), which depends on three parameters $\bar{n}_x$, $\bar{n}_y$ and $\bar{n}_z$. I will denote this Hamiltonian, for specific values of the three parameters, as $\mathbf{H}_{\mathrm{MF}}(\vec{\bar{n}})$, where $\vec{\bar{n}}$ is, as before, the vector whose components are the parameter values. Furthermore, I will denote the ground state of that Hamiltonian as $\left|\psi_0(\vec{\bar{n}})\right\rangle$,

$$\mathbf{H}_{\mathrm{MF}}(\vec{\bar{n}})\left|\psi_0(\vec{\bar{n}})\right\rangle = E_0(\vec{\bar{n}})\left|\psi_0(\vec{\bar{n}})\right\rangle, \tag{3.28}$$

where $E_0(\vec{\bar{n}})$ is the ground state energy of $\mathbf{H}_{\mathrm{MF}}(\vec{\bar{n}})$. Finally, I will use a superscript $\vec{\bar{n}}^k$ to denote the parameter values after the k-th step in the calculation, with the initial parameter values denoted as $\vec{\bar{n}}^0$. Given this notation, the iterative procedure is

$$\vec{\bar{n}}^k = \left\langle\psi_0(\vec{\bar{n}}^{k-1})\right| \frac{1}{N}\sum_q \vec{\mathbf{n}}_q \left|\psi_0(\vec{\bar{n}}^{k-1})\right\rangle, \tag{3.29}$$

where

$$\vec{\mathbf{n}}_q = (\mathbf{n}_{qx}, \mathbf{n}_{qy}, \mathbf{n}_{qz}). \tag{3.30}$$

In (3.29) I have used the fact that, since the orbital occupation is site-independent, one has

$$\forall j \forall \mu \langle \mathbf{n}_{j\mu}\rangle = \left\langle \frac{1}{N}\sum_j \mathbf{n}_{j\mu}\right\rangle = \left\langle \frac{1}{N}\sum_q \mathbf{n}_{q\mu}\right\rangle, \tag{3.31}$$

where $\langle\bullet\rangle$ indicates the ground-state expectation value. The step (3.29) is repeated until

$$\vec{\bar{n}}^k = \vec{\bar{n}}^{k-1} \tag{3.32}$$

up to prescribed accuracy.

The map defined by (3.29) can have multiple fixed points $\vec{\bar{n}}^{\star l}$, where l numbers the fixed points, in which case the solution should be chosen to be the fixed point for which the ground state energy $E_0(\vec{\bar{n}}^{\star l})$ is the lowest. Because of this one needs to be weary of choosing initial parameters $\vec{\bar{n}}^0$ – these have to be such that the flow is towards the correct fixed point. In order to make an informed choice in this regard it is useful to plot the flow of (3.29), visualising all the fixed points, as well as the directions of the flow in various regions of the parameter space. This is of course only practicable if the dimension of the parameter space is appropriately small – visualising flow in more than three dimensions is impossible. However, even then one can look at the flow with certain parameters fixed, which may still be informative. In the present case, however, the parameter space is three dimensional, with only two independent parameters because of the constraint (3.24). This makes plotting the Hartree flow particularly informative for the chalcogen chain.

The Hartree flow for the linearised chalcogen chain model (3.27) is shown in Fig. 3.5. For U smaller than t_σ there is only one fixed point $\vec{\bar{n}}^\star(U < U_{\text{crit.}})$ [see panel (a) and (b) in Fig. 3.5], adiabatically connected to the non-interacting solution

$$\vec{\bar{n}}^\star(U = 0) = (\bar{n}_x^\star, \bar{n}_y^\star, \bar{n}_z^\star) = (0.5961, 0.4486, 0.9553) \tag{3.33}$$

(see Tab. 3.1). With increasing U, this fixed point initially shifts towards the diagonal line $\bar{n}_x + \bar{n}_y = 1$ [see panel (a) vs (b) in Fig. 3.5].

For $U_{\text{crit.}}/t_\sigma = 3$ a discontinuous change occurs, whereby three new fixed points emerge near the corners of the parameter space, that is points corresponding to the parameter values

$$\begin{aligned} \vec{\bar{n}}^{\star 1}(U > U_{\text{crit.}}) &\approx (0, 1, 1), \\ \vec{\bar{n}}^{\star 2}(U > U_{\text{crit.}}) &\approx (1, 1, 0), \\ \vec{\bar{n}}^{\star 3}(U > U_{\text{crit.}}) &\approx (1, 0, 1), \end{aligned} \tag{3.34}$$

while the initial fixed point vanishes [see panel (c) and (d) in Fig. 3.5]. The three fixed points have very similar energies, with the fixed point $\vec{\bar{n}}^{\star 1}(U > U_{\text{crit.}})$ being the global ground state.

As U is increased even further, beyond the phase transition, the fixed points move farther towards the corners of the parameter space and the energy difference between their corresponding eigenstates becomes relatively less significant (relative to the typical spacing between the energy levels in the system), so that in the limit $U \to \infty$ the fixed points are located exactly at the points listed in (3.34) and their corresponding eigenenergies are degenerate.

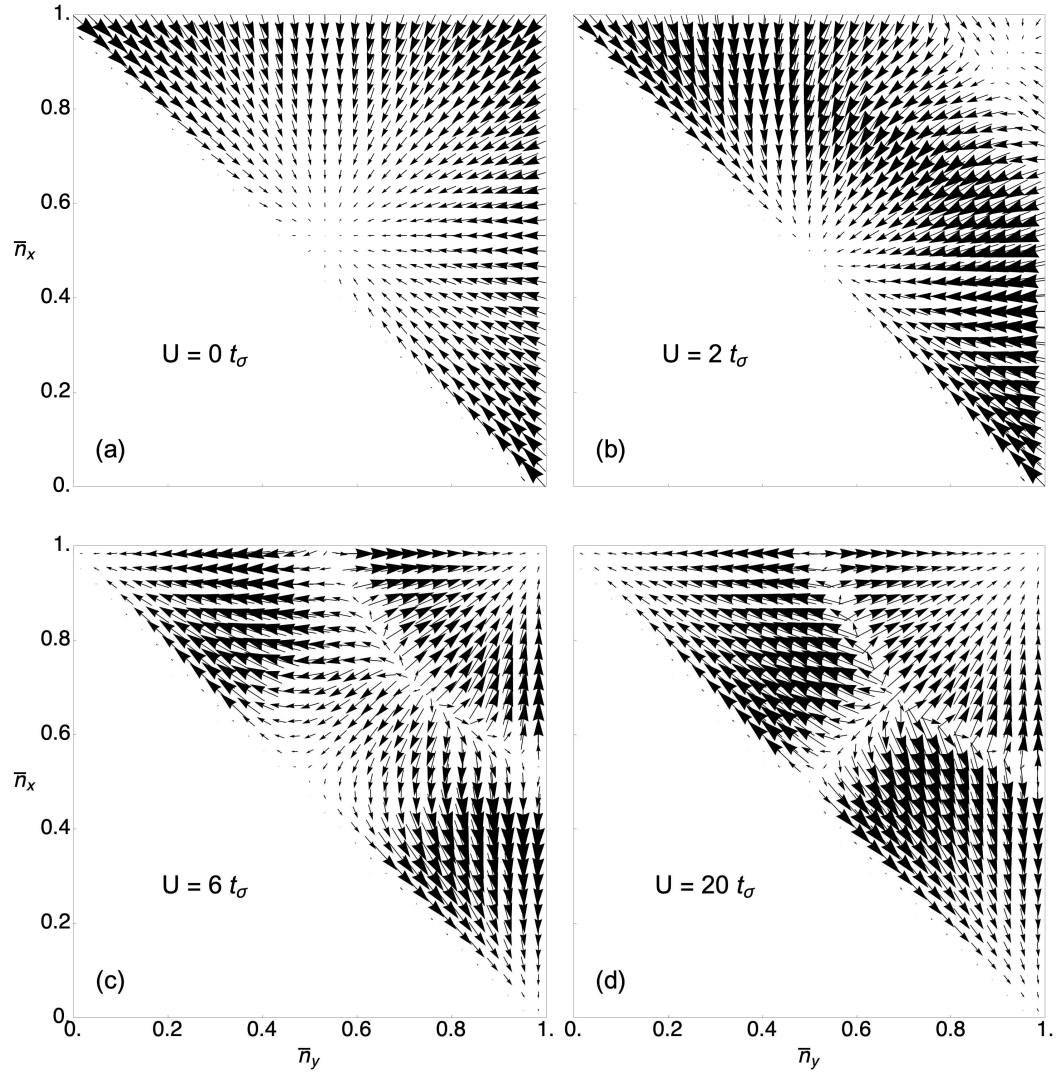

Figure 3.5: The Hartree flow of (3.29), for the linearised chalcogen chain model (3.27), with $t_\pi/t_\sigma = -1/3$ and $\alpha = 103^\circ$ ($\epsilon = 13^\circ$), for different values of U. (a) $U = 0$, (b) $U = 2t_\sigma$, (c) $U = 6t_\sigma$, (d) $U = 20t_\sigma$. The arrows represent the vectors $\vec{\bar{n}}^1 - \vec{\bar{n}}^0$, for different initial parameters $\vec{\bar{n}}^0$ [see (3.29)], projected onto the $\bar{n}_x$-$\bar{n}_y$ plane. In panels (a) and (b) one fixed point is visible, while in panels (c) and (d) there are three fixed points, located at the corners of parameter space. The ground state in panels (c) and (d) is the fixed point at the top left corner of the $\bar{n}_x$-$\bar{n}_y$ plane. For each point shown in the panels $\bar{n}_z = 2 - \bar{n}_x - \bar{n}_y$.

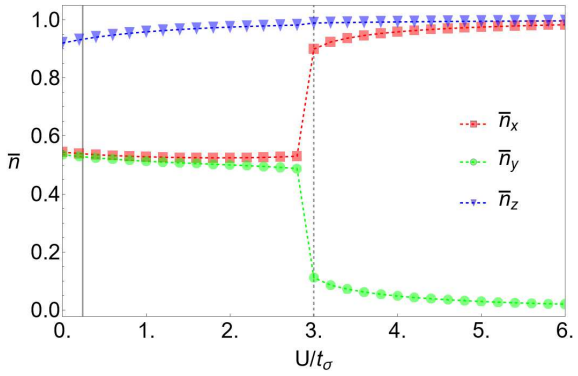

Figure 3.6: Ground state orbital density for the linearised chalcogen chain model (3.27), with $t_\pi/t_\sigma = -1/3$ and $\alpha = 103^\circ$ ($\epsilon = 13^\circ$), calculated using the Hartree method for different values of the Coulomb parameter U. The charge density in each orbital is indicated with a different colour. The grey vertical lines indicate the physically relevant value of $U/t_\sigma = 0.24$ [45, 46] (solid vertical line) and the critical value of $U_{\text{crit.}}/t_\sigma = 3$ (dashed vertical line).

3.3.4 Ground state orbital density

Having calculated the Hartree flow, one can use the flow diagram of Fig. 3.5 to pick a starting point $\vec{\bar{n}}^0$ in the parameter space for each U in turn and run the iteration defined by (3.29) until it converges to the exact solution in terms of the expectation values of orbital densities

$$\vec{\bar{n}}^\star(U) = \left\langle \psi_0(\vec{\bar{n}}^\star(U)) \right| \frac{1}{N} \sum_q \mathbf{n}_{q\mu} \left| \psi_0(\vec{\bar{n}}^\star(U)) \right\rangle \tag{3.35}$$

and the corresponding eigenenergy $E_0(\vec{\bar{n}}^\star(U))$. $\vec{\bar{n}}^0$ has to be chosen in such a way that the flow converges to the fixed point for which $E_0(\vec{\bar{n}}^\star(U))$ is the lowest, i.e. the ground state. The solution is shown in Fig. 3.6.

The evolution of orbital densities with increasing U clearly follows the evolution of the fixed points in the Hartree flow shown in Fig. 3.5, whereby the initial single fixed point for $U < U_{\text{crit.}}$ first moves slightly towards the $\bar{n}_x + \bar{n}_y = 1$ diagonal line, which is reflected in the slight downward trend in the evolution of $\bar{n}_x$ and $\bar{n}_y$ orbital occupations in Fig. 3.6 for $U/t_\sigma < 3$, and then disappears, being replaced by three fixed points in the corners of the parameter space in Fig. 3.5. The ground state, i.e. the fixed point corresponding to the lowest eigenenergy, is the fixed point near the $\bar{n}_y = 0$ corner of the parameter space in Fig. 3.5, which is reflected in the sharp

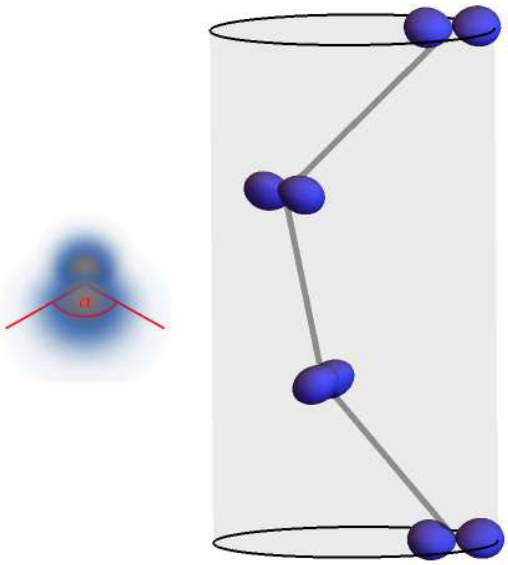

Figure 3.7: The '2-2-0' ODW ground state of the chalcogen chain for $U > U_{\text{crit.}}$. The hole orbital density is shown. The orbital density is represented schematically in blue, showing the ground-state distribution of the hole in the local p-orbital basis. On each site both the local p_z and p_x orbitals (see Fig. 3.1) are almost fully occupied by electrons, while the single hole per site (2/3 filling) occupies the p_y orbital. The inset shows the charge distribution of the hole in relation to the bond angle α. The shape is elongated along the bond-angle bisector (the y axis of the ALO basis, see Fig. 3.1)

.

decrease of the $\bar{n}_y$ orbital occupation in Fig. 3.6, as the varied parameter U passes the critical value of $U_{\text{crit.}}/t_\sigma = 3$.

3.3.5 Two different orbital density waves

For $U > U_{\text{crit.}}$ the ground-state orbital density changes and one obtains a different ODW solution than the '2-1-1' ODW found in the non-interacting and the weakly-interacting chalcogen chains (see Fig. 3.5 and 3.6). The ODW ground state found in the strongly-interacting limit is schematically shown on Fig. 3.7. The picture in the ALO basis is that the electrons fully localise on particular orbitals, in this case

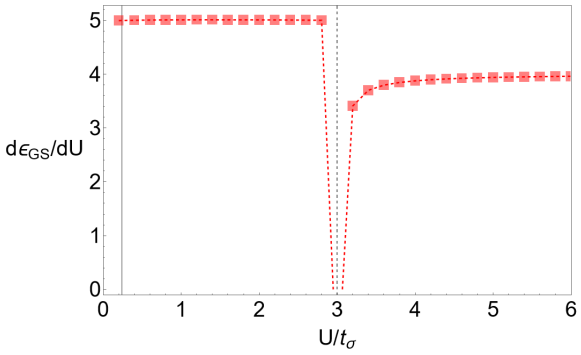

Figure 3.8: The derivative of the per-site ground-state energy ϵ_{GS} with respect to the Coulomb parameter U as a function of U for the linearised chalcogen chain model (3.27), with $t_\pi/t_\sigma = -1/3$ and $\alpha = 103^\circ$ ($\epsilon = 13^\circ$). At the critical value $U_{\mathrm{crit.}}/t_\sigma = 3$ a discontinuity appears, marking a phase transition. The grey vertical lines indicate the physically relevant value of $U/t_\sigma = 0.24$ [45, 46] (solid vertical line) and the critical value of $U_{\mathrm{crit.}}/t_\sigma = 3$ (dashed vertical line).

p_x and p_z, rather than remain distributed between different orbitals, as is the case for the ODW stable for $U < U_{\mathrm{crit.}}$. To differentiate this new ODW ground state from the weakly-interacting '2-1-1' ODW, I will call the ODW stable for $U > U_{\mathrm{crit.}}$ the '2-2-0' ODW, as in this limit one orbital is almost completely unoccupied. What one sees, therefore, is a transition between two different ODWs, of the '2-1-1' and '2-2-0' variety. This transition is accompanied by a discontinuity in the first derivative of the per-site ground-state energy with respect to the Coulomb parameter $d\epsilon_{\mathrm{GS}}/dU$, shown in Fig. 3.8.

This reordering of orbital density is favourable from the point of view of dominant inter-orbital Coulomb repulsion. Namely, if $U/t_\sigma \gg 1$ one can neglect the first term in (3.27) and obtain

$$\lim_{\frac{U}{t_\sigma}\to\infty} \mathbf{H}_{\mathrm{MF}} = U \sum_{\substack{\mu,\nu=x,y,z \\ \mu\neq\nu}} \left[\sum_Q \left(\bar{n}_\mu \mathbf{n}_{Q\nu} + \bar{n}_\nu \mathbf{n}_{Q\mu} \right) - N \bar{n}_\mu \bar{n}_\nu \right]. \tag{3.36}$$

Using the fact that for a fixed point of the iterative procedure (3.29)

$$\bar{n}_\mu = \langle \mathbf{n}_{j\mu} \rangle = \left\langle \frac{1}{N} \sum_Q \mathbf{n}_{Q\mu} \right\rangle \tag{3.37}$$

(see 3.23, 3.31 and 3.35), one can rewrite (3.36) as

$$\lim_{\frac{U}{t_\sigma}\to\infty} \mathbf{H}_{\mathrm{MF}} = NU \sum_{\substack{\mu,\nu=x,y,z \\ \mu\neq\nu}} \bar{n}_\nu \bar{n}_\mu. \tag{3.38}$$

Consequently, the ground state orbital density minimises the function

$$g = \bar{n}_x \bar{n}_y + \bar{n}_x \bar{n}_z + \bar{n}_y \bar{n}_z \tag{3.39}$$

with the additional constraint

$$\bar{n}_z = 2 - \bar{n}_x - \bar{n}_y. \tag{3.40}$$

This gives

$$g = \bar{n}_x \bar{n}_y + 2(\bar{n}_x + \bar{n}_y) - (\bar{n}_x + \bar{n}_y)^2, \tag{3.41}$$

with the constraints

$$n_x + n_y \in [1, 2] \tag{3.42}$$

and

$$\bar{n}_x \bar{n}_y \in \left[\bar{n}_x + \bar{n}_y - 1, \left(\frac{\bar{n}_x + \bar{n}_y}{2} \right)^2 \right]. \tag{3.43}$$

Consequently,

$$\min_{\bar{n}_x \bar{n}_y} g = -(\bar{n}_x + \bar{n}_y)^2 + 3(\bar{n}_x + \bar{n}_y) - 1, \tag{3.44}$$

which has three minima – two for $\bar{n}_x + \bar{n}_y = 1$ with $\bar{n}_x \bar{n}_y = 0$ and one for $\bar{n}_x + \bar{n}_y = 2$ with $\bar{n}_x \bar{n}_y = 1$. These are precisely the corners of the parameter space in Fig. 3.5. For finite U/t_σ the first term in (3.27) breaks the symmetry between the three minima, yielding a unique ground state discussed above.

3.4 Benchmark: Density Matrix Renormalization Group

3.4.1 Motivation

As I have already mentioned, the Hartree mean-field decoupling that I used in Sec. 3.3 is based on two key assumptions. The first assumption is that the true ground state can be approximated by a product state, at least if one's goal is to calculate the orbital densities in the chain. This assumption is a significant one. For instance, it becomes invalid when dealing with a strongly correlated system, for which the dominant energy

scale is linked to correlations, not to the kinetic energy associated with the tunnelling of non-interacting electrons. For such a system the eigenstates are very different from product states and it is impossible to capture its energy hierarchy, and therefore find the ground state, by approximating its eigenstates with product states. However, as I mentioned in Sec. 3.3, the non-interacting chalcogen chain is orbitally ordered and the gap protecting that order is significant (see Fig. 3.3), therefore the mean-field approach is reasonable, at least for $U_{\text{crit.}}/t_\sigma < 1$, and in particular for the physically significant value of $U/t_\sigma = 0.24$. Similarly, the infinite-U ground state should be captured by this method, as in this regime the tunnelling of electrons can be neglected and consequently the chain sites are completely uncorrelated. Nonetheless, some results of Sec. 3.3, in particular the critical value of the Coulomb parameter $U_{\text{crit.}}$, need to be supported by a calculation which takes correlations into account.

The second assumption of the particular Hartree calculation presented in Sec. 3.3 is that the phase transition occurs between ordered states with the same period [see (3.23)]. As I argued in Sec. 3.3, because the Fermi level in the non-interacting system does not cross any bands, there is no reason to expect a structural instability due to nesting (which would result in a change in the period of the ground-state order), at least for small, physical values of the Coulomb parameter U. However, this has to be ruled out explicitly, by a direct calculation using a different method which captures such phenomena.

For these reasons Cliò Efthimia Agrapidis, a co-author of [32], undertook a DMRG study of a finite, open chalcogen chain. This method was chosen because it takes correlations into account and does not impose any restrictions on the ground state order, in particular, it does not restrict the period of the possible orbital order in the open chain. I say more about the DMRG algorithm in the next section.

Presently, I stress that in context of this research I treat DMRG as a secondary tool, complementary to the primary Hartree method – a benchmark. This is because it is very difficult to interpret the results of state-of-the-art numerical calculations, unlike those of the Hartree method, which allows for back-of-the-envelope analytical calculations that I feel provide more physical insight, as long as they are reliable.

3.4.2 Method

While it is not my intention to describe the DMRG method in any detail, as I am not an expert or even a practitioner, nonetheless I believe that a general characterisation of the DMRG procedure and its capabilities is in order. This section will explain why this method is, on the one hand, a good benchmark for the Hartree method and, on

the other hand, a good method to exclude the possibility of the '2-1-1' ODW ground state undergoing a structural phase transition to a ground state with a different period, which is a possibility the Hartree method with the employed approximation [see (3.23)] cannot dismiss.

DMRG [47, 48] is a method of choice for considering one-dimensional systems with correlations. In particular, one-dimensional Hubbard models [to which family the chalcogen chain model (3.27) belongs] have been extensively studied using DMRG (see for instance [49, 50]). Just like the Hartree method, the DMRG algorithm is an approximate approach to finding the ground state of an interacting, quantum system. Both truncate the Hilbert space of the investigated model. In contrast to the Hartree method, however, where the truncation of the Hilbert space is done – quite crudely – by considering only product states built of single-particle wavefunctions, the truncation of the Hilbert space in DMRG is carried out in a more subtle and informed way.

Speaking in broadest possible terms, in the *finite* DMRG algorithm, which we use here, in each step the chain is divided into two parts – the system and the environment – and these two parts are coupled. The truncation of the Hilbert space is done using the eigenstates and eigenvalues of the reduced density matrix of the system. The eigenstates corresponding to the lowest eigenvalues (weights) in the reduced density matrix are discarded, so that a fixed total number m of highest-weight states is kept. In the next step, the system is grown by one site at the expense of the environment and the m states saved in the previous step, along with the new states on the added site, form the new product basis of the system. Then the procedure repeats. This way, while the system grows, the dimension of the Hilbert space of the system is unchanged, equal to m.

Crucially, unlike mean-field decoupling, this method of truncating the Hilbert space leaves in the dominant correlations, leading to a truly (if not fully) correlated description of the ground state. This allows it to capture many properties of correlated systems which the Hartree method, or indeed any mean-field method, is unable to. Moreover, as it is a real-space method which does not enforce any order on the ground state, DMRG can predict the onset of real space ground state modulations, such as charge density waves or antiferromagnetism. As I mentioned above, such spatial modulations (structural instabilities) can destabilise the '2-1-1' ODW ground state of the non-interacting chalcogen chain, but are disregarded in the Hartree calculation. As such, they need to be investigated using DMRG.

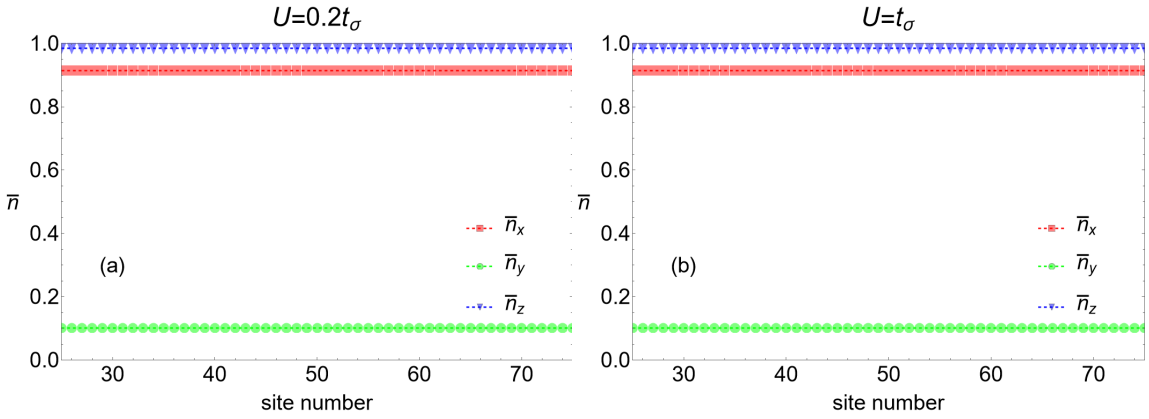

Figure 3.9: Orbital densities in the chalcogen chain (3.27), with $t_\sigma = 1$, $t_\pi = -1/3$ and $\alpha = 103^\circ$ ($\epsilon = 13^\circ$), in the ALO basis, plotted as a function of position in the chain (chain site number). Results obtained using DMRG on a finite, open chain, for (a) $U/t_\sigma = 0.2$ and (b) $U/t_\sigma = 1$. The chain length is $L = 100$ sites, with three orbitals per site. The middle half of the chain is shown, edges are omitted (see text). The '2-1-1' ODW ground state of the non-interacting chalcogen chain survives for both values of U, visible as a constant orbital polarisation in the ALO basis, which translates to a helical modulation in orbital densities in the AGO basis.

3.4.3 Results

The DMRG calculations presented below were performed using the finite DMRG algorithm [48] on a chalcogen chain of length $L \times 3$, where $L = 100$ is the chain length and 3 is the number of orbitals per site. Open boundary conditions were used. Up to $m = 2000$ density matrix eigenvalues were kept in the renormalization procedure. This way it was possible to obtain accurate results with an error $\delta/L = 10^{-10}$. To suppress edge effects, in what follows the local orbital densities are plotted only for sites between site number $L/4$ and site number $3L/4$ in the chain – away from the edges.

Weak Coulomb repulsion

Fig. 3.9 shows the results of a DMRG calculation performed for two values of the Coulomb parameter: $U/t_\sigma = 0.2$ and $U/t_\sigma = 1$. Presented in the plots are the orbital densities on different sites in the chain, with the edges of the chain omitted to disregard finite-size effects on chain ends. For both values of U the non-interacting

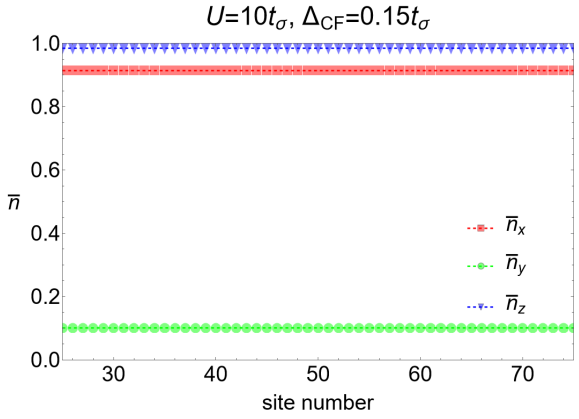

Figure 3.10: Orbital densities in the chalcogen chain (3.27), with $t_\sigma = 1$, $t_\pi = -1/3$ and $\alpha = 103^\circ$ ($\epsilon = 13^\circ$), in the ALO basis, plotted as a function of position in the chain (chain site number). Results obtained using DMRG on a finite, open chain, for $U/t_\sigma = 10$ with a weak CF $\Delta_{CF}/t_\sigma = 0.15$ splitting the energies of the three p orbitals, favouring the p_x orbital (lowest energy). The chain length is $L = 100$ sites, with three orbitals per site. The middle half of the chain is shown, edges are omitted (see text). The '2-2-0' ODW is found, visible as a constant orbital polarisation in the ALO basis, which translates to a helical modulation in orbital densities in the AGO basis.

'2-1-1' ODW ground state predicted by the Hartree calculation to survive in the small-U regime is recovered, visible as a constant orbital polarisation in the ALO basis (see caption).

The robustness of the non-interacting ground state is due to the fact that the non-interacting chalcogen chain ($U = 0$) is in an orbitally-ordered phase, protected by a finite gap. Consequently, the fluctuations of orbital densities due to the Coulomb interaction – captured in the DMRG method, but neglected in the mean-field calculation – are negligible, and the two pictures agree.

Two conclusions can be drawn from this. First, one sees that in the physical regime, that is for $U/t_\sigma \approx 0.24$ the '2-1-1' ODW is stable, which corroborates the mean-field results and supports [28]. Second, there is no structural deformation for $U/t_\sigma \leq 1$ which the mean-field method with the applied assumptions [see (3.23)] would fail to predict. This was expected, however, it still had to be checked.

Strong Coulomb repulsion

Fig. 3.10 shows the results of a DMRG calculation performed for the Coulomb parameter value $U/t_\sigma = 10$ with additional CF splitting between the three p orbitals $\Delta_{\mathrm{CF}}/t_\sigma = 0.15$, which lowers the energy of the p_x orbital. The '2-2-0' ODW predicted by the Hartree method is recovered.

The CF term is needed to stabilise this solution. Without it, the '2-2-0' ODW predicted by the Hartree calculation is not found for $U/t_\sigma = 10$. In fact, the calculation fails to converge in the available CPU time. For an even larger value of the Coulomb parameter, namely $U/t_\sigma = 20$, the calculation converges without the CF term, however, the ground state contains strong orbital density fluctuations in the chain (not shown). This result can be at least partly attributed to the open edges of the chain.

Importantly, including the weak, symmetry-breaking CF $\Delta_{\mathrm{CF}}/t_\sigma = 0.15$ reduces the calculation time 50-fold, suggesting a presence of competing interactions in the systems, likely related to the three very-nearly-degenerate fixed points in the edges of the parameter space identified in the mean field calculation (see Fig. 3.5) – the addition of CF breaks the approximate degeneracy between these three solutions, substantially reducing the DMRG calculation time.

3.5 Conclusions

3.5.1 Summary of results

In this chapter I have studied selenium and tellurium chains, which are helical chains described using a one-dimensional Hubbard model with an active p sub-shell. Using the mean-field Hartree approximation results, I have shown that, regardless of the strength of the Coulomb repulsion, the ground state of chalcogen chains is an ODW, whose period is the same as that of the helical chain itself. Moreover, I established that there exist two such ODW ground states, distinct from each other, stable for different values of the Coulomb parameter U and separated by a phase transition. For a physical value of the Coulomb parameter $U/t_\sigma \approx 0.24$ [41–43], and well above this value – up to $U_{\mathrm{crit.}}/t_\sigma = 3$, according to the mean-field calculation – the '2-1-1' ODW is stable. This ground state is the same as that for the non-interacting chain, previously reported in the literature [24, 26]. For very large, unrealistic values of the Coulomb parameter, $U/t_\sigma > 3$, a different ODW is seen to stabilise in the mean-field calculation – the '2-2-0' ODW. This ground state is easily understood when one

considers the infinite-U regime, where all interaction in the chain are completely local and different sites are uncorrelated.

To corroborate these results I have also shown DMRG results on an open chalcogen chain, obtained by a co-author of [32], Cliò Efthimia Agrapidis. This method also finds the '2-1-1' ODW for the physical value of $U/t_\sigma \approx 0.24$ and well beyond, up to at least $U/t_\sigma \approx 1$. Similarly, in the large-U regime, the DMRG calculation recovers the '2-2-0' ODW found in the mean-field results, albeit a small symmetry-breaking CF of magnitude $\Delta_{\mathrm{CF}}/t_\sigma = 0.15$ is needed to stabilise the solution. The only point at which these two methods disagree is the exact nature and position of the phase transition between the two ODWs, which is sharp in the mean-field calculation, occurring for $U_{\mathrm{crit.}}/t_\sigma = 3$, while in the DMRG results no such clear transition is observed. Instead, one sees a real-space modulation of the orbital density around the mean-field critical point (not shown), indicating, perhaps, a structural phase transition to an intermediate phase. However, further investigation is needed.

Thus, I have shown that the non-interacting, '2-1-1' ODW ground state of the chalcogen chain survives the inclusion of an inter-orbital Coulomb repulsion whose energy scale is comparable with that reported in real materials. Consequently, I have demonstrated that inter-orbital Coulomb repulsion is compatible with the '2-1-1' ODW described in the literature [24, 26]. This supports the scenario put forward by the authors of [28], who argue that in elemental selenium and elemental tellurium crystals a weak inter-orbital Coulomb repulsion leads to a deformation from a hypothetical simple cubic lattice towards the observed trigonal lattice (see introduction to this chapter).

3.5.2 Final remarks

This chapter highlights the fact that the chalcogen chain Hubbard model is different from the standard, one-dimensional Hubbard model. While in the latter one observes charge and spin density waves representing a structural phase transition, brought about by the introduction of arbitrarily weak Coulomb interaction, in the former no structural phase transition is observed even for relatively strong inter-orbital Coulomb repulsion. This is a consequence of different geometry in combination with anisotropic tunnelling amplitudes in the p sub-shell, which introduce sizeable gaps in the band structure, protecting the non-interacting ground state from perturbations due to Coulomb interactions. This shows the importance of considering the lattice deformations and geometry before formulating the tight-binding model.

Chapter 4

Interlude: One-dimensional topological insulators

In this chapter I introduce the key concepts in the field of topological insulators. I focus the discussion on one-dimensional topological insulators, a decision motivated by the intention to apply all of the concepts presented here as directly as possible to chalcogen chains, which is done in chapter 5.

This chapter is structured as follows. In Sec. 4.1 I provide a general discussion of topological insulators, with a special focus on one-dimensional topological insulators.

Sec. 4.2 discusses one-dimensional topological insulators protected by chiral symmetry. In Sec. 4.2.1 an example of such an insulator is given – the SSH model [16].

The final section, Sec. 4.3, discusses lattice-symmetry protected topological insulators in one dimension, with an example – the SSH-3 model [33] – given in Sec. 4.3.1.

4.1 Introduction

Topological insulators can be broadly divided into two categories. The first category, which I will call fundamental topological insulators (FTI), comprises topological insulators whose properties stem from their Hamiltonians having certain fundamental symmetries. These symmetries are time-reversal symmetry ($\mathcal{T}$), particle-hole (charge-conjugation) symmetry ($\mathcal{C}$) and chiral symmetry ($\mathcal{S}$). More on these symmetries below.

Insulators respecting the same combination of these three symmetries, and for

AZ class\d	0	1	2	3	4	5	6	7	T	C	S
A	$\mathbb{Z}$	0	$\mathbb{Z}$	0	$\mathbb{Z}$	0	$\mathbb{Z}$	0	0	0	0
AIII	0	$\mathbb{Z}$	0	$\mathbb{Z}$	0	$\mathbb{Z}$	0	$\mathbb{Z}$	0	0	1
AI	$\mathbb{Z}$	0	0	0	$2\mathbb{Z}$	0	$\mathbb{Z}_2$	$\mathbb{Z}_2$	+	0	0
BDI	$\mathbb{Z}_2$	$\mathbb{Z}$	0	0	0	$2\mathbb{Z}$	0	$\mathbb{Z}_2$	+	+	1
D	$\mathbb{Z}_2$	$\mathbb{Z}_2$	$\mathbb{Z}$	0	0	0	$2\mathbb{Z}$	0	0	+	0
DIII	0	$\mathbb{Z}_2$	$\mathbb{Z}_2$	$\mathbb{Z}$	0	0	0	$2\mathbb{Z}$	−	+	1
AII	$2\mathbb{Z}$	0	$\mathbb{Z}_2$	$\mathbb{Z}_2$	$\mathbb{Z}$	0	0	0	−	0	0
CII	0	$2\mathbb{Z}$	0	$\mathbb{Z}_2$	$\mathbb{Z}_2$	$\mathbb{Z}$	0	0	−	−	1
C	0	0	$2\mathbb{Z}$	0	$\mathbb{Z}_2$	$\mathbb{Z}_2$	$\mathbb{Z}$	0	0	−	0
CI	0	0	0	$2\mathbb{Z}$	0	$\mathbb{Z}_2$	$\mathbb{Z}_2$	$\mathbb{Z}$	+	−	1

Table 4.1: The ten-fold classification of fundamental topological insulators [51]. Each row corresponds to a different Atland-Zirnbauer (AZ) class. The columns labelled 0-7 corresponds to the number of spatial dimensions. The last three columns, labelled T, C and S, correspond to the time-reversal, charge-conjugation and chiral symmetries respectively. In columns 0-7, a $\mathbb{Z}$ entry indicates that for the given AZ class in the given dimension an integer topological invariant can be defined. Similarly, $\mathbb{Z}_2$ indicates a binary topological invariant, while $2\mathbb{Z}$ indicates an even integer topological invariant. 0 indicates that no topological invariant exists. In the two penultimate columns, a $\pm$ entry indicates that a particular class has given symmetry and that in this class this symmetry squares to ± 1, while 0 indicates that given symmetry is absent in this particular AZ class. In the last column, 1 indicates that given class has chiral symmetry (which must square to $+1$ as it is given by a unitary operator), while 0 indicates that in the given class chiral symmetry is absent. *Source: [52]*

whom the squares of the symmetry operators $\mathcal{T}^2$ and $\mathcal{C}^2$ are equal (either 1 or -1), are grouped together. Thus, the category of FTIs is subdivided into classes. This classification was first given by Atland and Zirnbauer [51] and is sometimes referred to as "the ten-fold way". It is usually represented as a table (Tab. 4.1). Importantly, the ten-fold way describes not only topological insulators. Some classes apply exclusively to superconductors described by Bogoliubov-de-Gennes-type Hamiltonians (classes D, C, DIII, CI) and therefore are not relevant for topological insulators.

Time reversal symmetry is defined as an anti-unitary operator which can be written as

$$\mathcal{T} = \vec{\mathbf{c}}^{\dagger} K U_T \vec{\mathbf{c}}, \tag{4.1}$$

where

$$\vec{\mathbf{c}} = (\mathbf{c}_0, \mathbf{c}_1, ...) \tag{4.2}$$

is the vector of annihilation operators in the relevant basis, K is complex conjugation

– i.e. $K^\dagger M K = M^\star$ for any matrix M – and U_T is the unitary part of the time-reversal symmetry

$$U_T = e^{i\vec{g}\cdot\vec{J}\pi}, \tag{4.3}$$

where

$$\vec{J} = \sum_n \vec{l}_n + \vec{s}_n \tag{4.4}$$

is the total pseudo-spin operator, with $\vec{l}_n$ being the angular-momentum operator (defined in 2.3) on the n-th site and $\vec{s}_n$ the spin operator (defined in 2.37), similarly on the n-th site. $\vec{g}$ is some axis, which depends on the spin and orbital basis choice. More precisely, a system with Hamiltonian $\mathcal{H}$ is time-reversal symmetric if

$$\exists \vec{g}\ \mathcal{T}^\dagger \mathcal{H} \mathcal{T} = \mathcal{H}. \tag{4.5}$$

U_T is simply a 180° rotation of pseudo-spin around axis $\vec{g}$. For spinless systems with no orbital degrees of freedom U_T becomes trivial and time-reversal symmetry becomes complex conjugation.

Particle-hole (charge conjugation) symmetry is the transformation

$$\vec{\mathbf{c}} \leftrightarrow \vec{\mathbf{c}}^\dagger, \tag{4.6}$$

accompanied by complex conjugation. A system is particle-hole symmetric if

$$\mathcal{C}^\dagger \mathcal{H} \mathcal{C} = -\mathcal{H}. \tag{4.7}$$

Finally, chiral symmetry is the combination of time-reversal and particle-hole symmetries.

The second category of topological insulators, which I will call lattice-symmetry-protected topological insulators (LSPTI), comprises topological insulators whose properties are a consequence of certain lattice symmetries of their respective Hamiltonians. By lattice symmetries I simply mean spatial symmetries, such as rotation symmetry, mirror symmetry or inversion. If the relevant lattice symmetry is broken (which can happen, for example, due to lattice deformations), the topological insulators in this category become topologically trivial. This means that while FTIs' topological properties are immune to a wide variety of disorders (it is difficult, for example, for non-magnetic disorder to break time-reversal symmetry), the properties of LSPTIs are more fragile, a lattice deformation being enough to destroy them.

A number of extended classification tables, in which the standard Atland-Zirnbauer table (Tab. 4.1) is extended to include various additional symmetries, have been

produced over the years. In [53] the authors extend the classification by considering inversion symmetry, in [52] a classification involving mirror symmetries is given. Finally, more comprehensive analyses of possible topological phases given different space-group symmetries can be found in [54–57].

In one dimension the variety of both FTIs and LSPTIs is strongly limited. Looking at Tab. 4.1 one sees that for FTIs in one-dimension there is a one-to-one correspondence between the presence of chiral symmetry ($\mathcal{C}$) and the presence of a topological invariant (if one excludes classes D, C, DIII, CI, not describing insulators). Therefore, the only FTIs in one dimension are chiral topological insulators. These are discussed in the next section. For LSPTIs, the limited variety in one dimension is a consequence of the limited number of lattice symmetries that one can consider in a chain. The only non-trivial possibilities are: (i) mirror symmetry, with the mirror plane normal to the chain, (ii) inversion symmetry and (iii) 180-degree rotation symmetry. For systems with neither orbital, nor spin degrees of freedom these three are all the same.

4.2 Chiral topological insulators in one dimension

A feature of chiral-symmetric Hamiltonians is that their energy spectrum is symmetric with respect to zero. For periodic Hamiltonians, a chiral-symmetric model is not necessarily chiral in each pseudo-momentum q block. For this to be the case, the chiral symmetry operator needs to commute with translations. Here, however, I will take chiral-symmetric to mean Hamiltonian which are chiral symmetric in each q block. These can be easily identified by checking if their band structure is symmetric with respect to zero energy.

For Hamiltonians defined on a lattice, chiral symmetry is often called the sub-lattice symmetry. This is because if

1. a Hamiltonian can be split into two sub-lattices A and B, with intra-lattice blocks H_A and H_B and inter-lattice blocks H_{AB} and H_{BA}

$$\mathbf{H} = \begin{pmatrix} \vec{\mathbf{a}}^\dagger & \vec{\mathbf{b}}^\dagger \end{pmatrix} \begin{pmatrix} H_{\mathrm{A}} & H_{\mathrm{AB}} \\ H_{\mathrm{BA}} & H_{\mathrm{B}} \end{pmatrix} \begin{pmatrix} \vec{\mathbf{a}} \\ \vec{\mathbf{b}} \end{pmatrix}, \tag{4.8}$$

   with

$$\vec{\mathbf{a}} = (\mathbf{a}_0, \mathbf{a}_1, ...), \tag{4.9}$$
$$\vec{\mathbf{b}} = (\mathbf{b}_0, \mathbf{b}_1, ...), \tag{4.10}$$

where $\mathbf{a}_j$ is the annihilation operator of an electron on the $j-th$ atom of sublattice A, while $\mathbf{b}_j$ is the annihilation operator of an electron on the $j-th$ atom of sublattice B,

2.
$$\begin{aligned} H_{\mathrm{A}} = H_{\mathrm{B}} = \mathbb{0}, \\ H_{\mathrm{AB}} = H_{\mathrm{BA}}^{\dagger}, \end{aligned} \tag{4.11}$$

then the Hamiltonian is chiral.

To see this, note that if one takes the matrix

$$S = \begin{pmatrix} \mathbb{1} & \mathbb{0} \\ \mathbb{0} & -\mathbb{1} \end{pmatrix}, \tag{4.12}$$

where $\mathbb{1}$ is the identity matrix, while $\mathbb{0}$ is the matrix of zeros, both of an appropriate size, and the Hamiltonian matrix

$$H \equiv \begin{pmatrix} \mathbb{0} & H_{\mathrm{AB}} \\ H_{\mathrm{AB}}^{\dagger} & \mathbb{0} \end{pmatrix}, \tag{4.13}$$

one has

$$S^{\dagger} H S = -H. \tag{4.14}$$

The situation described above is relatively common. One example is the tight-binding model of graphene.

Perhaps the best known model of a topological insulator in one dimension is the SSH model [16], which also features sublattice symmetry. Looking at it more closely is a useful exercise, as it constitutes a concrete example to supplement some general concepts presented so far. This is why I now move to discuss it. From now on I fix the inter-atomic distance $d = 1$.

4.2.1 Su-Schrieffer-Heeger model

The SSH model is given by a simple, half-filled chain of atoms with only nearest-neighbour tunnelling elements. There are two distinct, alternating tunnelling elements – t_1 and t_2. Consequently, the fundamental unit cell contains two atoms – a and b (see Fig. 4.1). If one labels the atoms in the chain as 0,1,2,3,... and divides them into two sublattices A (atoms 0,2,4,...) and B (atoms 1,3,5,...), then atom a in each

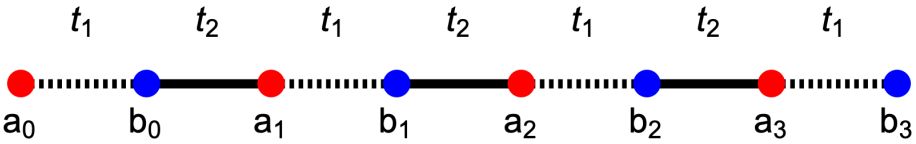

Figure 4.1: The SSH chain. The atoms of the A sublattice are coloured red, while the atoms of the B sublattice are coloured blue. The dashed lines mark the intra-unit-cell tunnelling amplitudes (t_1), the solid lines mark the inter-unit-cell tunnelling amplitudes (t_2). The atoms in each sublattice are numbered separately.

unit cell belongs to sublattice A, while atom b belongs to sublattice B. It is easy to check that this Hamiltonian splits into four blocks which satisfy (4.11). One has

$$\mathbf{H}_{\text{SSH}} = \begin{pmatrix} \vec{\mathbf{a}}^\dagger & \vec{\mathbf{b}}^\dagger \end{pmatrix} H_{\text{SSH}} \begin{pmatrix} \vec{\mathbf{a}} \\ \vec{\mathbf{b}} \end{pmatrix}, \tag{4.15}$$

with

$$H_{\text{SSH}} \equiv \begin{pmatrix} \mathbb{0} & H_{\text{AB}} \\ H_{\text{AB}}^\dagger & \mathbb{0} \end{pmatrix}, \tag{4.16}$$

where $\mathbb{0}$ indicates a matrix of zeros and

$$H_{\text{AB}} = \begin{pmatrix} t_1 & t_2 & 0 & 0 & \\ 0 & t_1 & t_2 & 0 & \\ 0 & 0 & t_1 & t_2 & \\ 0 & 0 & 0 & t_1 & \ddots \\ & & & & \ddots \end{pmatrix}. \tag{4.17}$$

In pseudo-momentum space the SSH Hamiltonian (4.15) splits into separate pseudo-momentum blocks

$$\mathbf{H}_{\text{SSH}} = \sum_q \begin{pmatrix} \mathbf{a}_q^\dagger & \mathbf{b}_q^\dagger \end{pmatrix} \begin{pmatrix} 0 & t_1 + t_2 e^{-i2q} \\ t_1 + t_2 e^{i2q} & 0 \end{pmatrix} \begin{pmatrix} \mathbf{a}_q \\ \mathbf{b}_q \end{pmatrix}, \tag{4.18}$$

where $q \in [-\pi/2, \pi/2)$ is the pseudo-momentum, $\mathbf{a}_q$ is the annihilation operator of an electron with pseudo-momentum q on sublattice A and $\mathbf{b}_q$ is the annihilation operator of an electron with pseudo-momentum q on sublattice B. Note that I have chosen t_1 to denote the tunnelling amplitude within the unit cell, while t_2 denotes the tunnelling amplitude between unit cells. Evidently, (4.18) has the same form as

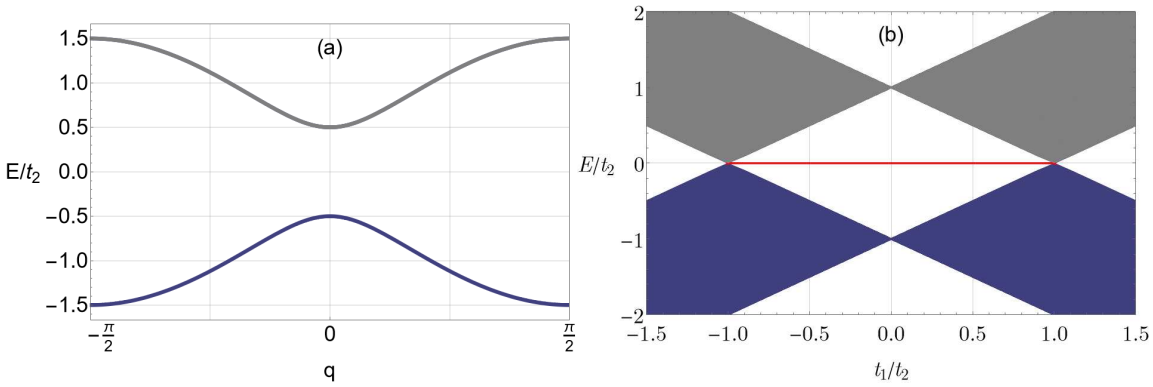

Figure 4.2: (a) Band structure of the SSH model with $t_1/t_2 = -0.5$ and (b) spectrum of the SSH model as a function of t_1/t_2, for a chain of length $L = 1000$ (see text). The filling is 1/2. The occupied bands/states are coloured blue, while the unoccupied bands/states are coloured gray. In both panels an insulating gap is clearly visible. Both the band structure and the spectrum are symmetric with respect to zero energy (chirality). Moreover, the spectrum is symmetric with respect to the transformation $t_1/t_2 \to -t_1/t_2$, which changes the phase of the band structure by $\pi/2$ (not shown). In panel (b), there are two symmetry-protected in-gap states which are coloured red. They disappear when the bulk gap closes, with the gap closing point at $|t_1/t_2| = 1$.

(4.11). This means that each pseudo-momentum block is chiral, and therefore the band structure has to be symmetric with respect to zero energy. The band structure of an infinite SSH chain with periodic boundary conditions and $t_1/t_2 = -0.5$ is shown in Fig. 4.2 (a). The spectrum of the SSH model on a finite, open chain of length $L = 1000$ is plotted in Fig. 4.2 (b) as a function of t_1/t_2. This chain length is divisible by the unit cell size of the SSH model and is large enough for finite size effects to be negligible. While Fig. 4.2 (a) shows that the SSH model is chiral and therefore its symmetry allows for it being a topological insulator, Fig. 4.2 (b) shows that in a finite, open chain there are indeed two zero-energy eigenstates that survive for a wide range of t_1/t_2, that is until the gap closes, indicating a topological phase.

Bulk topological properties

In order to establish the topological invariant associated with the observed end states one needs to go beyond the eigenvalues and look at the eigenvectors. For chiral Hamiltonians in one dimension in general, and for the SSH model Hamiltonian (4.18)

in particular, it is possible to define an integer topological invariant called the winding number [58]. The winding number ν is defined as

$$\nu = \sum_{n}^{\star} \frac{i}{2\pi} \int_{-\pi}^{\pi} dq \left(\langle \psi_n(q) | \partial_q \psi_n(q) \rangle - \langle \partial_q \psi_n(q) | \psi_n(q) \rangle \right), \tag{4.19}$$

where the $\star$ indicates that the sum runs over all occupied bands, $|\psi_n(q)\rangle$ is the eigenstate of the n-th band in a constant gauge form and $|\partial_q \psi_n(q)\rangle \equiv \partial_q |\psi_n(q)\rangle$. By a constant gauge form I mean that $|\psi_n(\pi)\rangle = |\psi_n(-\pi)\rangle$.

For the SSH model the winding number is especially simple to calculate, as there is only one occupied band. It is easy to check that the eigenstates of the SSH Hamiltonian (4.18), corresponding to the eigenvalues

$$\pm \epsilon = \pm \sqrt{t_1^2 + t_2^2 + 2 t_1 t_2 \cos q}, \tag{4.20}$$

take the constant gauge form

$$\vec{v}_{\pm} = \frac{1}{\sqrt{2}} (1, \pm e^{i\phi(q)}). \tag{4.21}$$

The phase ϕ is defined as

$$t_1 + t_2 e^{i2q} = \epsilon e^{i\phi(q)} \equiv z. \tag{4.22}$$

Using (4.19) and (4.21) one readily finds that

$$\nu = \phi(\pi) - \phi(-\pi). \tag{4.23}$$

Consequently, one can find ν graphically by analysing how the phase of (4.22) evolves as a function of q. This is presented in Fig. 4.3, which shows that as q changes from $-\pi/2$ to $\pi/2$ in the SSH model with $|t_2| \leq |t_1|$, ϕ does not wind full circle around the origin and consequently $\nu = 0$. Conversely, if $|t_2| > |t_1|$, ϕ winds full circle around the origin and $\nu = 1$. As a result, the ground state of the SSH model is a topological insulator only if $|t_2| > |t_1|$.

End states

A finite, one-dimensional, chiral topological insulator with non-zero ν is guaranteed to harbour in-gap states localised at the chain ends. The number of end states is 2ν. In this section I will characterise these end states for the finite SSH model with

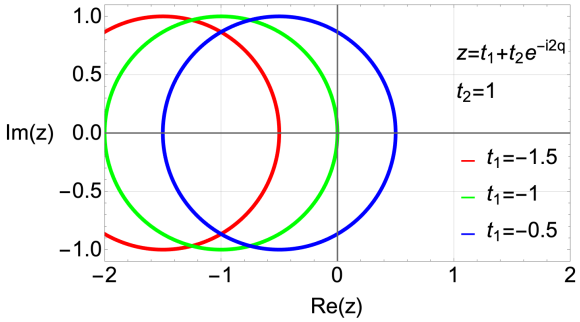

Figure 4.3: Parametric plots of z (4.22) for $q \in [-\pi/2, \pi/2)$, that is across the first Brillouin zone, with t_2=1. Different colours represent different values of t_1 (see legend). For $|t_1| < |t_2|$ the parametric plot of z encircles the origin. Consequently, the phase $\phi(q)$ differs by 2π at both ends of the first Brillouin zone and the winding number is $\nu = 1$. Conversely, if $|t_1| \geq |t_2|$ the phase $\phi(q)$ is the same at both ends of the first Brillouin zone and consequently $\nu = 0$. The plots are shown for $t_1/t_2 < 0$. For $t_1/t_2 > 0$ the curves are reflected with respect to the y axis.

open boundary conditions. First, note that in order for the bulk topological properties calculated above for the infinite SSH chain to hold for the open chain, the choice of the unit cell needs to be compatible with the cut – i.e. one must consider a chain which terminates at both ends with the edge of the fundamental unit cell. In the previous section I have established that the topologically non-trivial phase occurs when the inter-cell tunnelling amplitude t_2 is greater (per modulus) than the intra-cell tunnelling amplitude t_1. Consequently, I will consider an open chain terminating on one end with the a_0 site belonging to the A sublattice, and on the other end with the $b_{L/2}$ site from the B sublattice. The Hamiltonian of such a chain takes the form (4.15)-(4.17), with the dimension of each block equal to $L/2$, where L is the chain length.

Note that, due to chiral symmetry, the two end states need to be pinned to zero energy. This is seen by considering the chiral operator $\mathcal{S}$. First, notice that both end states must be eigenstates of $\mathcal{S}$. This is because $\mathcal{S}$ is proportional to identity on each sublattice [see (4.12)], so it preserves charge density in the chain, and both end states represent unique charge densities. Second, note that each eigenstate of the Hamiltonian $\mathbf{H}_{\text{SSH}} |\psi_n\rangle = \epsilon_n |\psi_n\rangle$ has to satisfy

$$\mathbf{H}_{\text{SSH}} \mathcal{S} |\psi_n\rangle = -\epsilon_n \mathcal{S} |\psi_n\rangle . \tag{4.24}$$

It follows that the energy of each end state must be zero. Finally, (4.12) shows that

the only way for the end states to be eigenstates of $\mathcal{S}$ is for each end state to be defined entirely on one sublattice.

One more symmetry is useful in finding the end states of the SSH model. The model has inversion symmetry, expressed by the operator $\mathcal{I}$. This symmetry maps one end of the chain onto the other and one end state onto the other. Consequently, it is enough to find one end state to know both. Because the chain terminates with atoms from different sublattices on each end, it also follows that if one end state is confined to sublattice A, the other must be confined to sublattice B. This also ensures their orthogonality.

All of the above tells us that in the basis of the Hamiltonian matrix (4.16)-(4.17) the coefficients of the wavefunction of one of the end states take the form

$$\vec{v} = \left(v_1, v_2, ..., v_{L/2}, 0, ..., 0\right). \tag{4.25}$$

This particular end state is confined to the A sublattice. It is now easy to check that for a zero-energy eigenstate

$$v_m = v_1 \left(-\frac{t_1}{t_2}\right)^{m-1}, \tag{4.26}$$

where v_1 is the normalization. Since $t_2 > t_1$, it represents a wavefunction decaying exponentially away from the left edge [1]. The charge density in this end state is shown in Fig. 4.4.

4.3 Symmetry-protected one-dimensional topological insulators

In this section I focus on topological insulators in one dimension which are protected not by one of the fundamental symmetries $(\mathcal{T}, \mathcal{C}, \mathcal{S})$, but rather by spatial, lattice symmetries, namely LSPTIs. Such topological insulator are less robust, in the sense that they are not as immune to disorder (they are only immune to disorder which preserves the relevant lattice symmetry). They are also less studied – the ten-fold

[1] Note that

$$H_{\mathrm{SSH}}\vec{v} = v_1 t_2 \left(-\frac{t_1}{t_2}\right)^{L/2} \vec{\xi}_{L-1}, \tag{4.27}$$

where $\vec{\xi}_{L-1}$ is a vector whose all components but the $L-1$-st (last) are zero. Namely, $\vec{v}$ is a zero-energy eigenstate only if $L \to \infty$ – the limit in which the end states are perfectly uncoupled.

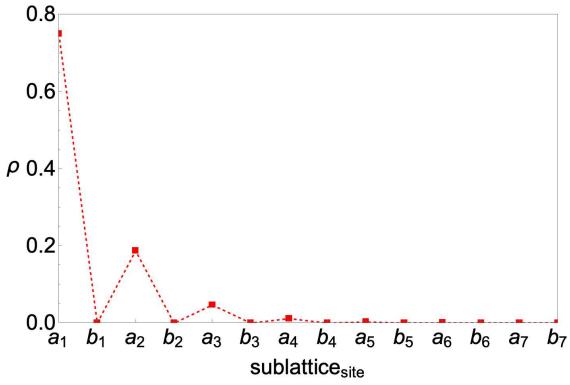

Figure 4.4: The left end state charge density in the SSH model with $t_1/t_2 = -0.5$. The charge density is decaying exponentially away from the edge and equal to zero on every second site. The right end state is obtained from the left using inversion.

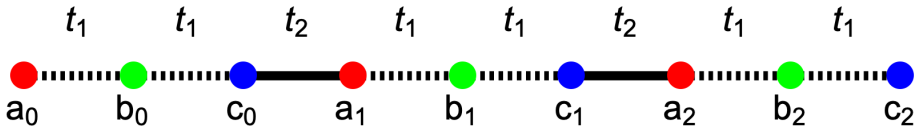

Figure 4.5: The SSH-3 chain. The atoms of the A sublattice are coloured red, the atoms of the B sublattice are coloured green and the atoms of the C sublattice are coloured blue. The dashed lines mark the intra-unit-cell tunnelling amplitudes (t_1), the solid lines mark the inter-unit-cell tunnelling amplitudes (t_2). The atoms in each sublattice are numbered separately.

classification [51] does not capture the topological phases that exist in such systems, it needs to be extended by considering different lattice symmetries.

Similarly to the previous section, I will now consider an example of a LSPTI. Again, I choose a very simple model, namely the SSH-3 model [15].

4.3.1 Period-three Su-Schrieffer-Heeger model

The SSH-3 model is that of a chain of atoms in which the tunnelling amplitudes on consecutive bonds follow a repeating $\cdots - t_1 - t_1 - t_2 - \ldots$ pattern. There are thus three non-equivalent positions in the fundamental unit cell – a, b and c – which can be grouped into three sublattices $a_0, a_1, \ldots = A$, $b_0, b_1, \ldots = B$ and $c_0, c_1, \ldots = C$. The tunnelling amplitudes between sublattices A and B and B and C are both t_1,

while the tunnelling amplitude between sublattices C and A is t_2. This is shown in Fig. 4.5. The filling is 2/3.

The SSH-3 Hamiltonian can be written as

$$\mathbf{H}_{\text{SSH-3}} = \begin{pmatrix} \vec{\mathbf{a}}^\dagger & \vec{\mathbf{b}}^\dagger & \vec{\mathbf{c}}^\dagger \end{pmatrix} H_{\text{SSH-3}} \begin{pmatrix} \vec{\mathbf{a}} \\ \vec{\mathbf{b}} \\ \vec{\mathbf{c}} \end{pmatrix}, \tag{4.28}$$

$$H_{\text{SSH-3}} = \begin{pmatrix} \mathbb{0} & H_{\text{BA}} & H_{\text{CA}} \\ H_{\text{BA}}^\dagger & \mathbb{0} & H_{\text{CB}} \\ H_{\text{CA}}^\dagger & H_{\text{CB}}^\dagger & \mathbb{0} \end{pmatrix}, \tag{4.29}$$

where

$$\begin{aligned} \vec{\mathbf{a}} &= (\mathbf{a}_0, \mathbf{a}_1, ...), \\ \vec{\mathbf{b}} &= (\mathbf{b}_0, \mathbf{b}_1, ...), \\ \vec{\mathbf{c}} &= (\mathbf{c}_0, \mathbf{c}_1, ...), \end{aligned} \tag{4.30}$$

with $\mathbf{a}_j$, $\mathbf{b}_j$ and $\mathbf{c}_j$ being the annihilation operators on the j-th atom of sublattice A, B and C respectively and

$$\begin{aligned} H_{\text{BA}} &= \begin{pmatrix} t_1 & 0 & 0 & \\ 0 & t_1 & 0 & \\ 0 & 0 & t_1 & \\ & & & \ddots \end{pmatrix}, \\ H_{\text{CA}} &= \begin{pmatrix} 0 & t_2 & 0 & \\ 0 & 0 & t_2 & \\ & & & \\ 0 & 0 & 0 & \ddots \\ & & & \end{pmatrix}, \\ H_{\text{CB}} &= \begin{pmatrix} t_1 & 0 & 0 & \\ 0 & t_1 & 0 & \\ 0 & 0 & t_1 & \\ & & & \ddots \end{pmatrix}, \end{aligned} \tag{4.31}$$

each a matrix of size $L/3$.

I choose the fundamental unit cell in such a way that t_2 is the inter-unit-cell tunnelling amplitude, while the two t_1 tunnelling amplitudes characterise tunnelling within each unit cell. With this choice, the Hamiltonian in pseudo-momentum space

is

$$\mathbf{H}_{\text{SSH-3}} = \sum_q \begin{pmatrix} \mathbf{a}_q^\dagger & \mathbf{b}_q^\dagger & \mathbf{c}_q^\dagger \end{pmatrix} \begin{pmatrix} 0 & t_1 & t_2 e^{-i3q} \\ t_1 & 0 & t_1 \\ t_2 e^{i3q} & t_1 & 0 \end{pmatrix} \begin{pmatrix} \mathbf{a}_q \\ \mathbf{b}_q \\ \mathbf{c}_q \end{pmatrix}, \tag{4.32}$$

where a_q, b_q and c_q are annihilation operators of an electron with pseudo-momentum $q \in [\pi/3, \pi/3)$ on sublattice A, B and C respectively. In contrast to the SSH model, the SSH-3 model has no sublattice symmetry. However, for a chain of length $L = 3M$, with $M \in \mathbb{N}$, it is inversion symmetric. When considering a finite system, I will use the chain length $L = 999$, which satisfies this condition and is large enough for finite size effects to be negligible.

The band structure of an infinite SSH-3 chain with periodic boundary conditions and with $t_1/t_2 = -0.5$ is shown in Fig. 4.6 (a). The spectrum of the SSH-3 model on a finite, open chain of length $L = 999$ is plotted in Fig. 4.6 (b) as a function of t_1/t_2. Panel (a) shows that the band structure is not chiral, which is a consequence of the absence of sublattice symmetry. Consequently, the winding number is not a topological invariant in the SSH-3 model. Yet, in Fig. 4.6 (b) we see that the spectrum of the SSH-3 model on an open chain contains in-gap states which survive for a wide range of model parameters, until the gap closing. It can be checked that these states are strongly localised at the ends of the chain, which indicates a topological phase. What is the nature of these end states?

First, one obvious possibility has to be excluded. Fig. 4.6 (b) shows that, even though the system is not chiral in the sense I use in this chapter, namely it is not chiral in each pseudo-momentum block [see Fig. 4.6 (a)], the energy spectrum itself is still symmetric with respect to zero energy. This indicates that there exists a chiral symmetry in the SSH-3 model, albeit it does not commute with translations. One needs to exclude the possibility that this symmetry is the origin of the end states. Fortunately, this is easy to do. Adding an extra term to the Hamiltonian

$$\mathbf{H}' = \delta \vec{\mathbf{b}}^\dagger \cdot \vec{\mathbf{b}} \tag{4.33}$$

breaks chiral symmetry. Fig. 4.7 (a) shows a plot of the spectrum of the Hamiltonian

$$\mathbf{H}'_{\text{SSH-3}} = \mathbf{H}_{\text{SSH-3}} + \mathbf{H}', \tag{4.34}$$

with $\mathbf{H}_{\text{SSH-3}}$ defined in (4.28)-(4.31), as a function of t_1/t_2. The in gap states survive until the gap closing, indicating that the system is in a topological phase even without chiral symmetry. Fig. 4.7 (b), on the other hand, shows the spectrum of the SSH-3

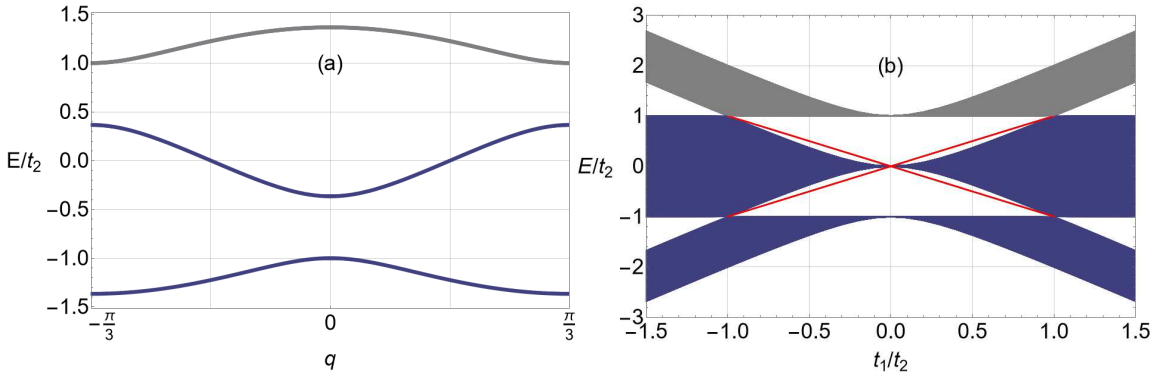

Figure 4.6: (a) Band structure of the SSH-3 model (4.28)-(4.31) with $t_1/t_2 = -0.5$ and (b) spectrum of the SSH-3 model (4.28)-(4.31) as a function of t_1/t_2, for a chain of length $L = 999$ (see text). The filling is 2/3. The occupied bands/states are coloured blue, while the unoccupied bands/states are coloured gray. In both panels two gaps are clearly visible, with the upper gap being the insulating gap at 2/3 filling. While the spectrum is symmetric with respect to zero energy, the band structure is not. Moreover, the spectrum is symmetric with respect to the transformation $t_1/t_2 \to -t_1/t_2$, which changes the phase of the band structure by $\pi/2$ (not shown). In panel (b), there are two in-gap states in each gap (coloured red), that disappear when the gap closes. The gap closing point is at $|t_1/t_2| = 1$.

model with preserved chiral symmetry but broken inversion symmetry. This is achieved by taking the model (4.28)-(4.31) and modifying equation (4.31) by putting

$$H_{\mathrm{CB}} = \begin{pmatrix} t_3 & 0 & 0 & \\ 0 & t_3 & 0 & \\ 0 & 0 & t_3 & \\ & & & \ddots \end{pmatrix} \neq H_{\mathrm{BA}}. \tag{4.35}$$

In this case the in-gap states are pushed into the bulk continuum without the gap closing, indicating a topologically-trivial phase. This strongly suggests inversion symmetry as the symmetry responsible for the presence of the end states.

Bulk

Since, according to the ten-fold classification of topological phases, the only fundamental symmetry which leads to non-trivial topological properties in one dimension is

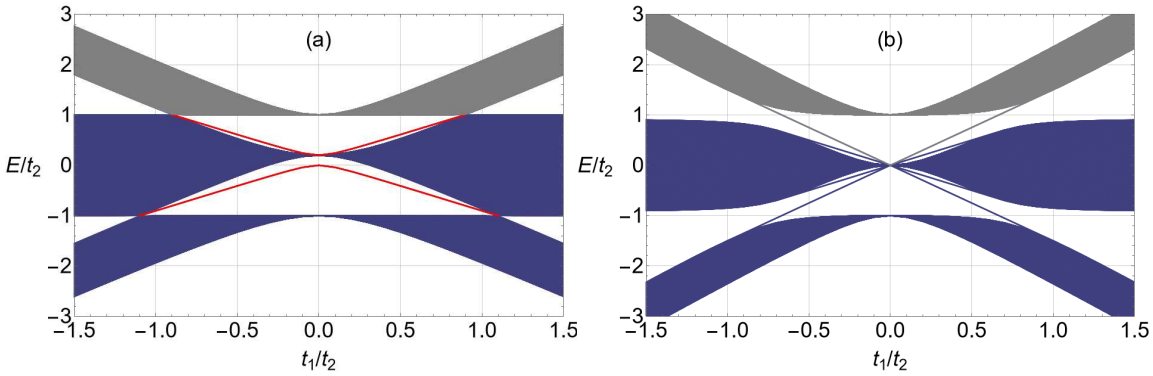

Figure 4.7: (a) The spectrum of the SSH-3 model with broken chiral symmetry (4.34), with $\delta/t_2 = 0.2$, plotted as a function of t_1/t_2 and (b) the spectrum of the SSH-3 model with broken inversion symmetry [(4.28)-(4.31) with the modification (4.35)], with $t_3/t_2 = 1.5 \times t_1/t_2$, plotted as a function of t_1/t_2. The system size in both panels is $L = 999$. The occupied states are coloured blue, while the unoccupied states are coloured gray. The filling is 2/3. While in panel (a) the in-gap states are symmetry protected and cannot be pushed into the continuum without closing the bulk gap, in panel (b) the in-gap states disappear into the bulk without the gap closing. This shows that it is the inversion symmetry which protects the end states in the SSH-3 model.

the chiral symmetry, the origin of the topological phase in the SSH-3 model is clearly not linked to one of the fundamental symmetries, as its topological properties survive the breaking of chiral symmetry [see Fig. 4.7 (a)]. What remains is lattice symmetries. As I have shown [see Fig. 4.7 (b)], the SSH-3 model is topological as long as it is inversion-symmetric. If one breaks inversion symmetry, the phase becomes trivial. The inversion symmetry operator is defined as

$$\mathcal{I} = \left(\vec{\mathbf{a}}^\dagger_{-q} \;\; \vec{\mathbf{b}}^\dagger_{-q} \;\; \vec{\mathbf{c}}^\dagger_{-q}\right) I \begin{pmatrix} \vec{\mathbf{a}}_q \\ \vec{\mathbf{b}}_q \\ \vec{\mathbf{c}}_q \end{pmatrix}. \tag{4.36}$$

with

$$I = \begin{pmatrix} & & 1 \\ & \iddots & \\ 1 & & \end{pmatrix}. \tag{4.37}$$

One can therefore label the bands of the SSH-3 model at inversion-symmetric pseudo-momenta (pseudo-momenta for which $-3q = 3q$, that is $q = 0, \pm\pi/3$) with their

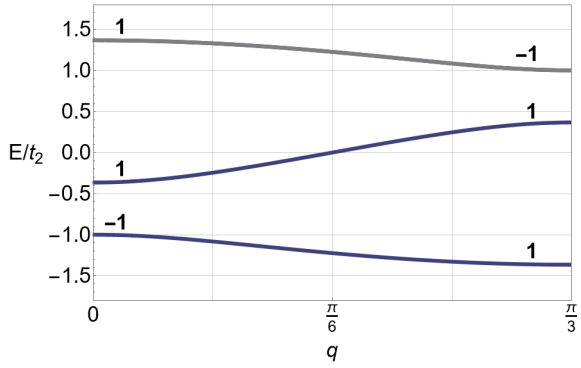

Figure 4.8: The band structure of the SSH-3 model (4.28)-(4.31) with $t_1/t_2 = -0.5$, with bands labelled using the corresponding eigenvalues of the inversion matrix (4.37) at inversion-invariant pseudo-momenta. The eigenvalues of the top and bottom bands change between $q = 0$ and $q = \pi/3$. Consequently, the SSH-3 model at 1/3 and 2/3 fillings is topologically non-trivial.

corresponding eigenvalues of the inversion matrix (4.37). Such labels are shown in Fig. 4.8.

One can then define a $\mathbb{Z}_2$ topological invariant as [59]

$$\mathcal{N} = \sum_{n}^{\star} \left[\vec{v}_n^{\dagger}(\pi) I \vec{v}_n(\pi) - \vec{v}_n^{\dagger}(0) I \vec{v}_n(0) \right] \mod 2, \tag{4.38}$$

where $\vec{v}_n(q)$ is the eigenvector of the n-th band at pseudo-momentum q, I is defined in (4.37), and the sum runs over all occupied bands. For a 2/3-filled SSH-3 model with $t_1/t_2 < 1$, $\mathcal{N} = 1$.

End states

Fig. 4.6 (b) shows that the SSH-3 model (4.28)-(4.31) with $t_1/t_2 < 1$ is topologically non-trivial. There are two gaps, one at 1/3 filling and one at 2/3 filling. There are two end states in each gap, which survive until the gaps are closed. The energy of the in-gap states $\vec{w}_{\pm}$ is exactly

$$\epsilon_{\pm} = \pm \frac{t_1}{t_2}. \tag{4.39}$$

I consider the 2/3-filled SSH-3 model, which means that the upper gap is the insulating gap. Consequently, the relevant end state is $\vec{w}_+$ if $t_1/t_2 > 0$ and $\vec{w}_-$ if $t_1/t_2 < 0$.

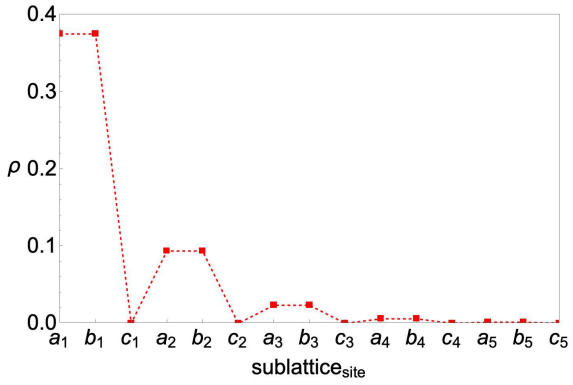

Figure 4.9: The charge density of the upper-gap, left end state of the SSH-3 model with $t_1/t_2 = -0.5$. The charge density is decaying exponentially away from the edge. In each unit cell it is equal on the A and B sublattices and zero on sublattice C. Thus, the end-state charge density is an exponentially decaying x-x-0 CDW. The right end state is obtained from the left using inversion.

It turns out that in the basis of the Hamiltonian (4.28)-(4.31), the end states of the SSH-3 model follow a regular pattern. The left end states are

$$\vec{w}_+ = w_1 \left(1, -\frac{t_1}{t_2}, ..., \left(-\frac{t_1}{t_2}\right)^{L/3-1}, 1, -\frac{t_1}{t_2}, ..., \left(-\frac{t_1}{t_2}\right)^{L/3-1}, 0, ..., 0\right), \qquad (4.40)$$

and

$$\vec{w}_- = w_1 \left(1, \frac{t_1}{t_2}, ..., \left(\frac{t_1}{t_2}\right)^{L/3-1}, -1, -\frac{t_1}{t_2}, ..., -\left(\frac{t_1}{t_2}\right)^{L/3-1}, 0, ..., 0\right), \qquad (4.41)$$

where w_1 is the normalization[2]. The corresponding right end states are obtained by reversing the order of coefficients (inversion).

Note that (4.40) and (4.41) are non-zero on sublattices A and B but exactly zero on sublattice C. Moreover, in both end states the charge distribution is equal on sublattices A and B, which translates to an exponentially decaying x-x-0 pattern in real space charge density. This is shown in Fig. 4.9.

[2]Note that

$$(H_{\text{SSH-3}} - \epsilon_\pm \mathbb{1})\, \vec{w}_\pm = w_1 t_2 \left(\mp \frac{t_1}{t_2}\right)^{L/3} \vec{\zeta}_{L-1} \qquad (4.42)$$

where $\vec{\zeta}_{L-1}$ is a vector whose all components but the $L-1$-st (last) are zero. Namely, $\vec{w}_\pm$ is a zero-energy eigenstate only if $L \to \infty$ – the limit in which the end states are perfectly uncoupled.

Chapter 5

Topology of chalcogen chains

This chapter is based on a 2023 article titled *'Topology of chalcogen chains'*, published in *Physical Review B 107, 125123* [36].

The topology of elemental chalcogens has not been extensively studied, although there exist electronic structure calculations that indicate that elemental selenium and tellurium undergo a topological phase transition from an insulator to a Weyl semi-metal under strain [60, 61]. There are also reports that surface states may be identified in crystals of elemental selenium [35], but their topological origin has not yet been conclusively established.

In this chapter I show that the topology of chalcogen chains, which are the weakly-coupled building blocks of elemental selenium and tellurium (see chapter 2 for details), is adequately described by the SSH-3 model (4.28)-(4.31) – an extension of one of the best-known topological models in condensed matter, the SSH model (4.15)-(4.17). What makes this result remarkable is that – despite the rise of topology to one of the prominent positions in modern condensed mater research – physical implementations of prototypical models of topological order are rare. One such implementation, however, is found in helical chalcogen chains which implement the conceptually-simple physics of the SSH-3 model.

I also demonstrate that the charge- and orbitally-ordered ground state of the chalcogen chain contains topological end states which are orbitally polarised. The orbital order in chalcogen chains is strongly reminiscent of the so-called orbital SSH model [15, 62]. I show, however, that the two models are topologically distinct. The topological invariant characterising the chalcogen chain model is the one-dimensional line invariant appropriate for time reversal symmetric systems with a two-fold lattice symmetry, the so called LBO invariant[34].

Model	Equation	Invariant	End states
SSH	(4.15)-(4.17)	ν (4.19) ($\mathbb{Z}_2$)	Fig. 4.4
SSH-3	(4.28)-(4.31)	$\mathcal{N}$ (4.38) ($\mathbb{Z}_2$)	Fig. 4.9
Orbital SSH	(5.5)-(5.7)	ν (4.19) ($\mathbb{Z}_2$)	Fig. 4.4 [1]
Cubic chain	(2.55)-(2.56)	$\mathcal{N}$ (4.38) ($\mathbb{Z}_2$)	Fig. 5.4 (b)
Chalcogen chain	(2.48)	$\mathcal{N}_{\mathcal{W}}$ (5.10) ($\mathbb{Z}_2$)	Fig. 5.4 (a)

Table 5.1: The five models of topological insulators described in chapters 4 and 5.

This chapter is organised as follows. In Sec. 5.1 I recall two models introduced in chapter 2, the chalcogen chain model and the cubic chain model, and introduce a third model – the orbital-SSH model. The summary of the models covered in this chapter is given in Tab. 5.1.

In Sec. 5.2 I analyse the topological properties of the chalcogen chain model. In particular: In Sec. 5.2.1 I show the band structure of a periodic chalcogen chain and the spectrum of a finite, open chalcogen chain as a function of the spin-obit parameter λ. The latter exhibits in-gap states which vanish when the gap closes. In Sec. 5.2.2 I link the presence of the in-gap states to the $\mathcal{R}_\pi$ (2.50) crystalline symmetry of the chalcogen chain. In Sec. 5.2.2 I describe the topological invariant of the bulk chalcogen chain. Finally, in Sec. 5.2.4 I describe the end states.

In Sec. 5.3 I compare the topological properties of the chalcogen chain model with those of the cubic chain model. Even though the latter is a much simpler model, it provides some key insights that help understand the former – it provides a link between the chalcogen chain model and the relatively simple SSH-3 model, discussed in chapter 4.

In Sec. 5.4 I compare the chalcogen and the cubic chain models to the orbital SSH model. I show that, despite some remarkable similarities, the first two models are topologically distinct from the third.

In Sec. 5.5 I provide some concluding remarks.

5.1 Models

In this section I consider three models – the chalcogen chain model, the cubic chain model and the orbital SSH model (see Tab. 5.1). Each model is studied for a different reason. While the chalcogen chain model provides a realistic description of a

[1] In one orbital flavour, no end states in the other orbital flavour.

chalcogen chain, the other two models, though much simpler, are nonetheless useful to pinpoint the key features that lead to non-trivial topological properties in the chalcogen chain model.

The chalcogen chain model and the cubic chain model were already introduced in chapter 2 and here I simply recall their Hamiltonians and discuss their relevance for chalcogen chains. The orbital SSH model, while still related to helical chains described at length in chapter 2, appears here for the first time. Consequently, I devote more space to its discussion compared with the other two models.

Chalcogen chain model

The chalcogen chain model Hamiltonian $\mathbf{H}_{\text{scc}}$ in real space and in the GO basis (see Sec. 2.2.2) is given by (2.48). The filling is 2/3 which is realistic for chalcogens [23, 24, 32]. In the GP basis (see Sec. 2.2.3) the chalcogen chain Hamiltonian is given by (2.46).

I use the following parameters: the inter-atomic distance is $a = 1$, the ratio of tunnelling amplitudes is $t_\pi/t_\sigma = -1/3$ and the bond angle is $\alpha = 103^\circ$. Finally, according to [63], the values of the SOC splitting between outermost orbitals (equal to $1.5 \times \lambda/t_\sigma$) are 0.23 for selenium and 0.49 for tellurium. This gives $\lambda/t_\sigma = 0.15$ for selenium and $\lambda/t_\sigma = 0.33$ for tellurium. Keeping this in mind, I will treat λ/t_σ as a free parameter in the model[2].

Cubic chain model

The cubic model Hamiltonian $\mathbf{H}_{\text{cubic}}$ in real space and in the GO basis is given by (2.55)-(2.56). The filling is 2/3. The inter-atomic distance is $a = 1$, the ratio of tunnelling amplitudes is $t_\pi/t_\sigma = -1/3$.

Remarkably, in the spinless cubic chain model the orbital channels separate, yielding three independent chains – one per orbital flavour. This is because the orbital channels are uncoupled, i.e. there are no tunnelling processes mixing different orbitals. To find the Hamiltonian for a single orbital channel consider the relevant orbital, say p_x. Next, pick a bond in the right-angle helical chain (see Fig. 2.7) which is aligned with the $\vec{x}$ direction of the orbital basis. The tunnelling element for the p_x orbital on this bond is t_σ, preceded by two t_π tunnelling elements on the $\vec{y}$ and $\vec{z}$ bonds which

[2]Note that $\lambda/t_\sigma > 0$, which indicates that $\lambda > 0$, since for p orbitals $t_\sigma > 0$. The SOC term is negative [see (2.48)] because the filling is 2/3 and since for more-than-half-filled orbital shells the sign of the SOC term is negative [64]

appear before the $\vec{x}$ bond [see (2.55)]. The pattern repeats every three sites

$$\cdots - t_\pi - t_\pi - t_\sigma - \ldots \tag{5.1}$$

The periodic tunnelling pattern (5.1) is precisely the $\cdots - t_1 - t_1 - t_2 - \ldots$ pattern of the SSH-3 model (4.28)-(4.31), which I described in Sec. 4.3.1.

For p_y and p_z orbitals the situation is exactly the same, albeit the pattern (5.1) undergoes a cyclic permutation, i.e. it is shifted by one lattice site to the right (p_z orbital) or to the left (p_y orbital). These shifts will be opposite for a helix with the opposite helicity. Thus, the cubic chain model splits into three SSH-3 models

$$\mathbf{H}_{\text{cubic}} = \sum_{m=I,II,III} \mathbf{H}^m_{\text{SSH-3}}, \tag{5.2}$$

where m numbers the three possible shifts, and $\mathbf{H}^I_{\text{SSH-3}}$ was defined in (4.28)-(4.31). The form of $\mathbf{H}^m_{\text{SSH-3}}$ for other m is the same, albeit with

$$\begin{aligned} H^{II}_{\text{BA}} &= H^I_{\text{BA}} \\ H^{II}_{\text{CB}} &= \tfrac{t_2}{t_1} H^I_{\text{CB}} \\ H^{II}_{\text{CA}} &= \tfrac{t_1}{t_2} H^I_{\text{CA}} \end{aligned} \tag{5.3}$$

for $m = II$, and

$$\begin{aligned} H^{III}_{\text{BA}} &= \tfrac{t_2}{t_1} H^I_{\text{BA}} \\ H^{III}_{\text{CB}} &= H^I_{\text{CB}} \\ H^{III}_{\text{CA}} &= \tfrac{t_1}{t_2} H^I_{\text{CA}} \end{aligned} \tag{5.4}$$

for $m = III$. The matrices H^I_{XY}, $X, Y = A, B, C$ were defined in (4.31). Finally, the $\mathcal{R}_\pi$ symmetry of the cubic chain translates to inversion symmetry in one of the three SSH-3 chains.

Orbital SSH model

The orbital SSH model is also an example of a helical chain, one with the helix angle $\beta = 180^\circ$ (see Fig. 2.1). For this helix angle the helical chain becomes a zigzag chain, with all atoms lying on a single plane. The alignment of consecutive bonds alternates between the $\vec{x}$ and $\vec{y}$ directions, with neighbouring bonds forming a 90-degree angle. On each site two orbitals are considered – the p_x orbital and the p_y orbital (see Fig. 5.1). As per usual Slater-Koster rules [9], the p_x orbital tunnelling amplitude along the $\vec{x}$ bond is t_σ, while along the $\vec{y}$ bond it is t_π. The situation is exactly opposite for the p_y orbital.

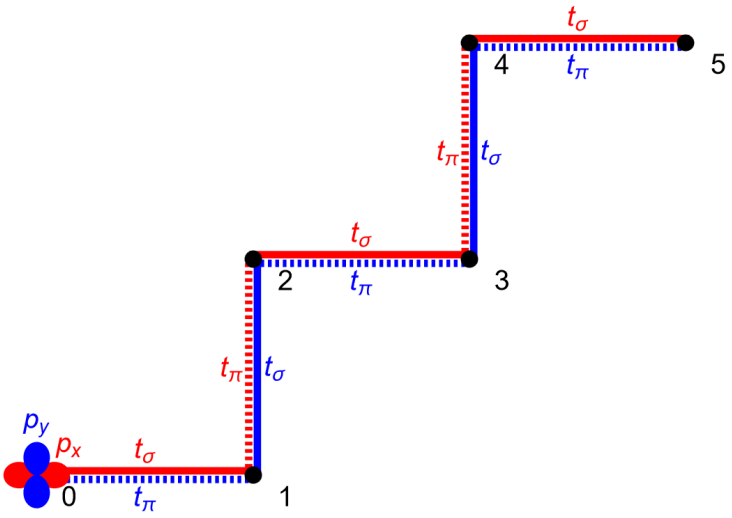

Figure 5.1: The zigzag chain in which the orbital SSH model is realised. On each site the local Hilbert space consists of two p orbitals, p_x and p_y (drawn schematically on site 0). On each bond the p_x orbital (red) and the p_y orbital (blue) have different tunnelling amplitudes, either t_σ (continuous line) or t_π (dashed line). This leads to an alternating $\cdots - t_\pi - t_\sigma - \ldots$ tunnelling pattern for each of the two orbitals, albeit the pattern for the p_x orbital is shifted by one chain site with respect to the pattern for the p_y orbital.

The real space Hamiltonian of the orbital SSH model is

$$\mathbf{H}_{\text{orb.}} = \sum_j \vec{\mathbf{c}}^{\,xy\dagger}_{j+1} \bar{K}_j \vec{\mathbf{c}}^{\,xy}_j + \text{h.c.}, \tag{5.5}$$

with

$$\vec{\mathbf{c}}^{\,xy}_j = (\mathbf{c}_{jx}, \mathbf{c}_{jy}), \tag{5.6}$$

where $\mathbf{c}_{jx}$ and $\mathbf{c}_{jy}$ are the annihilation operators of electrons on site j and orbital p_x and p_y respectively, while

$$\bar{K}_j = \begin{cases} \begin{pmatrix} t_\sigma & 0 \\ 0 & t_\pi \end{pmatrix} & j = 0 \bmod 2 \\ \begin{pmatrix} t_\pi & 0 \\ 0 & t_\sigma \end{pmatrix} & j = 1 \bmod 2 \end{cases}. \tag{5.7}$$

The filling is 1/2. The inter-atomic distance is $a = 1$ and the ratio of tunnelling amplitudes is set to $t_\pi/t_\sigma = -1/3$.

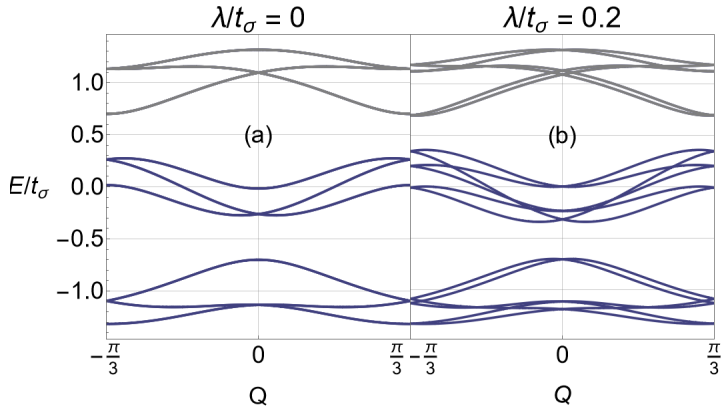

Figure 5.2: Band structure of the chalcogen chain model (2.48): (a) without SOC $\lambda/t_\sigma = 0$, and (b) with SOC $\lambda/t_\sigma = 0.2$. The other parameters are: the inter-atomic distance $a = 1$, the ratio of tunnelling amplitudes $t_\pi/t_\sigma = -1/3$ and the bond angle $\alpha = 103°$. Occupied bands are coloured blue, unoccupied bands are coloured gray.

The two orbital channels in the orbital SSH model decouple in a fashion completely analogous to the cubic model. However, while in the cubic model the three channels decouple to three copies of the SSH-3 model shifted by one site with respect to one another, in the orbital SSH model the channels decouple to two copies of the SSH model, one for the p_x orbital and one for the p_y orbital, also shifted by one lattice distance with respect to one another. Incidentally, this separation of orbital channels justifies neglecting the p_z orbital. If it were not neglected, it would decouple to form a simple chain, with equal tunnelling amplitudes on every bond, not leading to any interesting physics, at least from a topological viewpoint.

5.2 Topology of the chalcogen chain model

5.2.1 Band structure and spectrum

Fig. 5.2 shows the band structure of the chalcogen chain model (2.48) without SOC [panel (a)] and with SOC ($\lambda/t_\sigma = 0.2$) [panel (b)]. Two substantial band gaps are clearly visible in both cases, with the Fermi level located in the upper gap. Panel (a) is the same as Fig. 3.3 (d), since without SOC the band structures of the spinless and spinfull chalcogen chains are the same. Compared to Fig. 3.3 (d), however, there is an additional degeneracy of the bands in Fig. 5.2 (a), which is lifted by SOC in Fig.

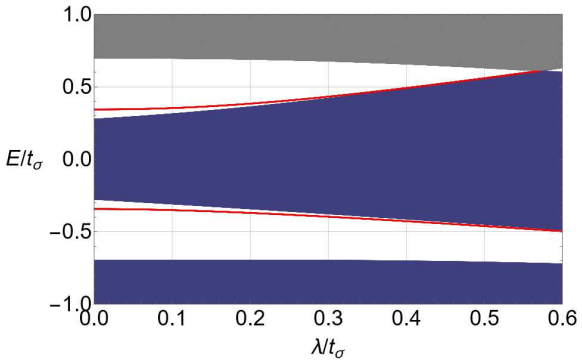

Figure 5.3: The spectrum of the chalcogen chain model (2.48) as a function of λ/t_σ on a finite open chain of length $L = 501$ [4]. The other parameters are: the interatomic distance $a = 1$, the ratio of tunnelling amplitudes $t_\pi/t_\sigma = -1/3$ and the bond angle $\alpha = 103°$. The end states are coloured red, the occupied bulk states are coloured blue and the unoccupied bulk states are coloured gray. There are four end states in each gap.

5.2 (b).

Fig. 5.3 shows the spectrum of the chalcogen chain model as a function of λ/t_σ. As the SOC λ increases, the upper gap closes, with the closing point at $\lambda_{\text{crit.}}/t_\sigma \approx 0.57$. The four in-gap states disappear after the gap closing, indicating a topological phase transition. Since in real chalcogen chains $\lambda/t_\sigma \in [0.15, 0.33]$ (see above), Fig. 5.3 indicates that chalcogen chains harbour a topological ground state. In the lower gap, the four in-gap states disappear into the bulk at around $\lambda/t_\sigma = 0.8$, while the gap remains open even for very large λ/t_σ (not shown). I will omit the lower gap in my analysis, as it lies well below the Fermi level.

For completeness, note that if one were to increase α further, beyond the value $\alpha = 103°$ in chalcogens, one would necessarily encounter a topological phase transition. This is because for $\alpha = 180°$ the helical chain becomes a simple chain which is not gapped at 2/3 filling and therefore cannot be a topological insulator. However, I have verified that the bulk invariant (5.10) defined below is robust up to at least $\alpha = 120°$, well beyond the bond angle reported for chalcogens.

[4] This system size respects the three-atom unit cell of the chalcogen chain and at the same time is large enough for finite size effects to be negligible. It is smaller than system sizes used in chapter 4, as the chalcogen chain model is more complex than the models discussed there.

5.2.2 Bulk topological properties

The spectrum of the chalcogen chain model exhibits in-gap states which survive until the gap closing. This is highly indicative of a topological phase and the existence of an associated topological invariant. What might this invariant be?

Looking at the band structure in Fig. 5.2 one sees that the chalcogen chain model (2.48) is not chiral, and therefore the winding number is not quantised, ruling it out as a topological invariant. As I have discussed in chapter 4, the only remaining option is that the chalcogen chain model describes an LSPI, with an associated crystalline symmetry protecting the topological phase. As discussed in Sec. 2.3.3, the only crystalline symmetry of the chalcogen chain is $\mathcal{R}_\pi$ (2.50), a 180-degree rotation around the axis $\vec{r}$ going through the atom at the centre of the chain (see Fig. 2.6).

Since the chalcogen chain model is spinfull, the situation is more complicated than the one discussed in chapter 4 for the SSH-3 model. The difference is the transformation of spin and orbital degrees of freedom upon $\mathcal{R}_\pi$, as well as the properties of the time-reversal symmetry operator $\mathcal{T}$ (4.1) (which is a symmetry of both the chalcogen chain model and, trivially, any spinless model without orbital degrees of freedom, such as the SSH-3 model). In models without spin or orbital quantum numbers $\mathcal{T}$ is equivalent to complex conjugation and always squares to +1. Moreover, in such systems 180-degree rotation symmetry (or, equivalently, mirror or inversion symmetry) always commutes with the simple $\mathcal{T}$ operator. In such a scenario one can always define the topological invariant $\mathcal{N}$ (4.38). In contrast, in a spinfull system with both $\mathcal{T}$ and $\mathcal{R}_\pi$ symmetries $\mathcal{T}$ may square to either +1 or -1 and either commute or anti-commute with $\mathcal{R}_\pi$.

In the chalcogen chain model $\mathcal{T}$ can be chosen so that its unitary part is equal to $\mathcal{R}_\pi$. Consequently, $\mathcal{T}$ commutes with $\mathcal{R}_\pi$ and squares to -1. In such a situation a topological invariant exists, distinct from (4.38). This is the LBO invariant [34].

The Lau-Brink-Ortix invariant

The 180-degree rotation symmetry of the chalcogen chain $\mathcal{R}_\pi$ can be regarded as spinfull inversion. One can therefore generalise the notion of inversion eigenvalues used to define the invariant (4.38) in the SSH-3 model [59]. The crux of the generalization is that instead of using inversion eigenvalues one uses the spectrum of the Wilson loop operator $\mathcal{W}$ to define the topological invariant. $\mathcal{W}$ is defined as

$$\mathcal{W}_{nm} = \langle E_n(Q_1)| \mathcal{P}(Q_2) \dots \mathcal{P}(Q_N) |E_m(Q_1)\rangle \,, \tag{5.8}$$

with

$$\mathcal{P}(Q) = \sum_{n}^{\star} |E_n(Q)\rangle \langle E_n(Q)| \,, \tag{5.9}$$

where $|E_m(Q_j)\rangle$ are the eigenstates of the chalcogen chain Hamiltonian (2.48) and $Q_j = 2\pi j/N$ are the pseudo momenta, with N taken large enough to assure convergence. The symbol $\star$ in the sum indicates that the summation is over occupied bands, so that the operators $\mathcal{P}(Q)$ are projectors onto the occupied subspace for a given q.

Due to the symmetry $\mathcal{R}_\pi$ the spectrum of the $\mathcal{W}$ operator comprises $+1$, -1 or pairs of complex conjugate numbers of unit modulus [59]. The invariant is the number of -1 eigenvalues in the spectrum, which I denote as $\mathcal{N}_{(-1)}$. In [59] the authors show that for spinless inversion-symmetric systems (such as the SSH-3 model) $\mathcal{N}_{(-1)}$ is equal to $\mathcal{N}$ (4.38). For spinfull systems, however, no such equality exists. In case of the chalcogen chain model $\mathcal{N}$ (4.38) is zero, because in each Kramers doublet there are two opposite $\mathcal{R}_\pi$ eigenvalues. $\mathcal{N}_{(-1)}$, meanwhile, is non-zero and is a topological invariant.

Finally, from the general classification involving mirror symmetries [65], and more specific work [34], it follows that a one-dimensional system with the symmetries of the chalcogen chain model can support only one non-trivial phase. Therefore, we define a $\mathbb{Z}_2$ topological invariant as

$$\mathcal{N}_{\mathcal{W}} = \frac{1}{2}\mathcal{N}_{(-1)} \mod 2. \tag{5.10}$$

This expression is equivalent to the LBO invariant [34], and is valid as long as $\mathcal{N}_{(-1)}$ is even, which is always satisfied because the bands come in pairs of time-reversal partners and each pair's contribution to $\mathcal{N}_{(-1)}$ is either 0 or 2. For the chalcogen chain model we find that $\mathcal{N}_{\mathcal{W}} = 1$ and $\mathcal{N}_{\mathcal{W}} = 0$ at 2/3-filling for $\lambda < \lambda_{\text{crit.}}$ and $\lambda > \lambda_{\text{crit.}}$ respectively. The critical value $\lambda_{\text{crit.}}$ coincides with the gap closing in Fig. 5.3.

5.2.3 Bulk-boundary correspondence

In one dimension, the bulk-boundary correspondence is robust only when a symmetry exists which binds the end states to zero energy, that is either chiral symmetry or particle-hole symmetry, with only the former relevant to insulators. In any other case the energy of in-gap states can be pushed into the bulk continuum by a local potential. Whether this happens or not depends on the specific model. In the chalcogen chain model the fact that $\mathcal{N}_{\mathcal{W}} = 1$ for some λ is consistent with the appearance of in-gap

states in Fig. 5.3. However, these are not protected by chiral symmetry. Thus, in order to establish their robustness, in this section I perform an expansion of the chalcogen chain model (2.46) around the upper gap closing.

There are two points in the first Brillouin zone for which the gap closes (see Fig. 5.2), symmetric with respect to $Q = 0$. I will first focus on the gap closing at pseudo-momentum $Q_0 > 0$. I proceed as follows. I first perform a basis change $\mathbf{u}_{Q_0,\lambda_{\text{crit.}}}$ to the eigenbasis of the chalcogen chain Hamiltonian (2.46) at $Q = Q_0$ and $\lambda = \lambda_{\text{crit.}}$.

$$\mathbf{H}'_{\text{scc}}(Q,\lambda) = \mathbf{u}^{\dagger}_{Q_0,\lambda_{\text{crit.}}} \mathbf{H}_{\text{scc}}(Q,\lambda)\, \mathbf{u}_{Q_0,\lambda_{\text{crit.}}}, \tag{5.11}$$

where $\mathbf{H}_{\text{scc}}(Q,\lambda)$ is the chalcogen chain Hamiltonian (2.46) with the dependence on pseudo-momentum Q and the SOC parameter λ explicitly stated. Note that $\mathbf{H}'_{\text{scc}}(Q_0,\lambda_{\text{crit.}})$ is diagonal.

It turns out that $\mathbf{H}'(Q,\lambda)$ is real. The existence of a basis in which the chalcogen chain Hamiltonian is real is guaranteed, because

$$\mathcal{T}^{\dagger}\mathcal{R}^{\dagger}_{\pi}\mathbf{H}_{\text{scc}}(Q,\lambda)\mathcal{R}_{\pi}\mathcal{T} = \mathbf{H}^{*}_{\text{scc}}(Q,\lambda) = \mathbf{H}_{\text{scc}}(Q,\lambda). \tag{5.12}$$

The first equality is a consequence of the fact that the unitary part of $\mathcal{T}$ is the same as $\mathcal{R}_{\pi}$ (see Sec. 5.2.2), and both are a two-fold symmetry, while the second equality simply states that since both $\mathcal{T}$ and $\mathcal{R}_{\pi}$ are symmetries, so is their product.

Next, I project the resulting Hamiltonian onto the two eigenstates forming the Dirac cone at Q_0, obtaining an effective 2×2 Hamiltonian

$$\mathbf{h}(Q,\lambda) = \mathbf{P}\mathbf{H}'_{\text{scc}}(Q,\lambda)\mathbf{P}, \tag{5.13}$$

where $\mathbf{P}$ is the relevant projection operator. Since $\mathbf{h}(Q,\lambda)$ is real, I can write it as

$$\mathbf{h}(Q,\lambda) = \begin{pmatrix} \mathbf{c}^{\dagger}_1 & \mathbf{c}^{\dagger}_2 \end{pmatrix} h(Q,\lambda) \begin{pmatrix} \mathbf{c}_1 \\ \mathbf{c}_2 \end{pmatrix}, \tag{5.14}$$

with

$$h(Q,\lambda) = s(Q-Q_0,\lambda)\sigma_0 + f(Q-Q_0,\lambda)\sigma_x + g(Q-Q_0,\lambda)\sigma_z, \tag{5.15}$$

where the scalar term is $s(0,\lambda_{\text{crit.}}) = E_0$ (the gap closing energy) and $f(0,\lambda_{\text{crit.}}) = g(0,\lambda_{\text{crit.}}) = 0$. After subtracting the scalar term, the effective 2×2 Hamiltonian becomes

$$\tilde{h}(Q,\lambda) = h(Q,\lambda) - s(Q-Q_0,\lambda)\sigma_0 = f(Q-Q_0,\lambda)\sigma_x + g(Q-Q_0,\lambda)\sigma_z, \tag{5.16}$$

which is chiral.

Were $\tilde{h}(k,\lambda)$ the full 2×2 Hamiltonian, the standard bulk-boundary correspondence guarantees that it would support zero-energy end states upon interfacing with a trivial phase. For the full 2×2 Hamiltonian $h(k,\lambda)$, however, this is not necessarily the case. This is because the scalar term, while irrelevant for the topology of the bulk, does not commute with $\tilde{h}(k,\lambda)$ on an open chain and can therefore affect the end states. One therefore needs to check whether the chirality-breaking scalar term in (5.15) affects the in-gap states.

To this end I follow the standard adiabatic argument in which I claim that interfacing a non-trivial phase of $h(Q,\lambda)$ with the vacuum is equivalent to continuously interpolating between the non-trivial and trivial phases by changing the parameters of the model. This involves passing through the gapless point. The linear expansion of $h(Q,\lambda)$ around the gap closing point is

$$\begin{aligned} h_{\text{lin.}} &= h(Q_0+\delta Q, \lambda_{\text{crit.}}+\delta\lambda) \\ &= E_0 + \delta\lambda\left(a_1\sigma_0 + a_2\sigma_x + a_3\sigma_z\right) + \delta Q\left(b_1\sigma_0 + b_2\sigma_z\right) + \\ &+ \mathcal{O}\left(\delta Q^2, \delta\lambda^2\right), \end{aligned} \tag{5.17}$$

where a_i and b_i are real numbers. In the continuum setting

$$\begin{aligned} \delta Q &= -i\partial_x, \\ \delta\lambda &= \lambda(x), \end{aligned} \tag{5.18}$$

I search for solutions of the Schrödinger equation

$$h_{\text{lin.}} \begin{pmatrix} \psi_a(x) \\ \psi_b(x) \end{pmatrix} = E \begin{pmatrix} \psi_a(x) \\ \psi_b(x) \end{pmatrix}. \tag{5.19}$$

More explicitly

$$\begin{aligned} &-i\, M\partial_x \begin{pmatrix} \psi_a(x) \\ \psi_b(x) \end{pmatrix} + R\lambda(x) \begin{pmatrix} \psi_a(x) \\ \psi_b(x) \end{pmatrix} \\ &= (E-E_0) \begin{pmatrix} \psi_a(x) \\ \psi_b(x) \end{pmatrix}, \end{aligned} \tag{5.20}$$

with

$$M = \begin{pmatrix} b_1+b_2 & 0 \\ 0 & b_1-b_2 \end{pmatrix}, \tag{5.21}$$

and

$$R = \begin{pmatrix} a_1 + a_3 & a_2 \\ a_2 & a_1 - a_3 \end{pmatrix}. \tag{5.22}$$

Since the interesting solutions (i.e. in-gap states) are those whose energy in the vicinity of the gap-closing is equal to the gap-closing energy E_0, I search for solutions of the homogeneous Schrödinger equation

$$-i\, M\partial_x \begin{pmatrix} \psi_a(x) \\ \psi_b(x) \end{pmatrix} + R\lambda(x) \begin{pmatrix} \psi_a(x) \\ \psi_b(x) \end{pmatrix} = 0. \tag{5.23}$$

I postulate

$$\psi_a(x) = C_a \exp\left(\gamma \int \lambda(x) dx\right) \tag{5.24}$$

$$\psi_b(x) = C_b \exp\left(\gamma \int \lambda(x) dx\right), \tag{5.25}$$

where γ is a parameter to be determined. (5.23) now reads

$$\lambda(x) \exp\left(\gamma \int \lambda(x) dx\right) A \begin{pmatrix} C_a \\ C_b \end{pmatrix} = 0, \tag{5.26}$$

with

$$A = \begin{pmatrix} -ib_+\gamma + a_+ & a_2 \\ a_2 & -ib_-\gamma + a_-) \end{pmatrix}, \tag{5.27}$$

where

$$\begin{aligned} a_\pm &= a_1 \pm a_3, \\ b_\pm &= b_1 \pm b_2. \end{aligned} \tag{5.28}$$

If $\lambda(x) \neq 0$ a solution exists for such γ that $\mathrm{Det}(A) = 0$. In the case of the chalcogen chain model with realistic parameters (that is $\alpha = 103°$, $t_\sigma = 1$, and $t_\pi/t_\sigma = -1/3$) two solutions exist:

$$\Psi_j = \begin{pmatrix} \psi_a^{(j)}(x) \\ \psi_b^{(j)}(x) \end{pmatrix}, \tag{5.29}$$

with $j = 1, 2$ and

$$\psi_a^{(j)}(x) = C_{aj} \exp\left(\gamma_j \int \lambda(x) dx\right) \tag{5.30}$$

$$\psi_b^{(j)}(x) = C_{bj} \exp\left(\gamma_j \int \lambda(x) dx\right), \tag{5.31}$$

with $\gamma_1 = -0.582 + 0.056i$, $\gamma_2 = 0.582 + 0.056i$, i.e. $\gamma_2 = -\gamma_1^*$.

Depending on the shape of the domain wall, only one of these solutions is physical and one can set the other one to zero, so that $\Psi_j(\pm\infty) = 0$. If I choose

$$\begin{aligned} \lambda(x) &= \Lambda \tanh\left(\frac{x}{w}\right), \\ \int \lambda(x)dx &= \Lambda w \log\cosh\left(\frac{x}{w}\right) > 0, \end{aligned} \tag{5.32}$$

the topological phase occurs for $x \to -\infty$, where $\lambda = \lambda_{\text{crit.}} - \Lambda$, while the trivial phase occurs when $x \to +\infty$, where $\lambda = \lambda_{\text{crit.}} + \Lambda$. I set $C_{a2} = C_{b2} = 0$. Then, the solution is

$$\Psi_1(x) = \begin{pmatrix} C_{a1} \\ C_{b1} \end{pmatrix} \exp\left(\gamma_1 w \Lambda \log\cosh\frac{x}{w}\right). \tag{5.33}$$

Thus, I obtain the localization length of the domain-wall state by taking the limit

$$\Psi_1(x \to \pm\infty) \propto e^{|x|\Lambda\gamma_1}, \tag{5.34}$$

which gives

$$\xi = \frac{1}{\Lambda\,|\text{Re}(\gamma_1)|}\,. \tag{5.35}$$

This characterises one end state. A similar analysis of the other gap closing point, at $Q_0' < 0$, yields another. This solution describes a state with energy E_0 – lying in the gap and constant for all values of $\lambda(x) < \lambda_{\text{crit.}}$ – and whose localization length is finite. One concludes that in the vicinity of the gap closing the end states survive even in the presence of the scalar term.

Note that this conclusion applies only in the region around the gap closing, where the linearised model (5.17) is valid. In particular, the constant energy of end states for $\lambda(x) < \lambda_{\text{crit.}}$ obtained in the above calculation is at odds with the dispersion of the end states in the upper gap observed in the chalcogen chain model (see Fig. 5.3). This is because the linearised model (5.17) is a two-band p-orbital model and consequently the SOC interaction in the linearised model $h^{\lambda}_{\text{lin.}}$ is much simpler than that in the full chalcogen chain model, namely,

$$h^{\lambda}_{\text{lin.}} \propto -\lambda L_z \otimes \sigma_z. \tag{5.36}$$

As a result, the linearised model does not capture the evolution of the end-state energy with λ. It does, however, show that the end states survive near the gap closing. This, taken together with the results of exact diagonalization (see Fig. 5.3), allows one to conclude that the end states survive for $\lambda(x) < \lambda_{\text{crit.}}$.

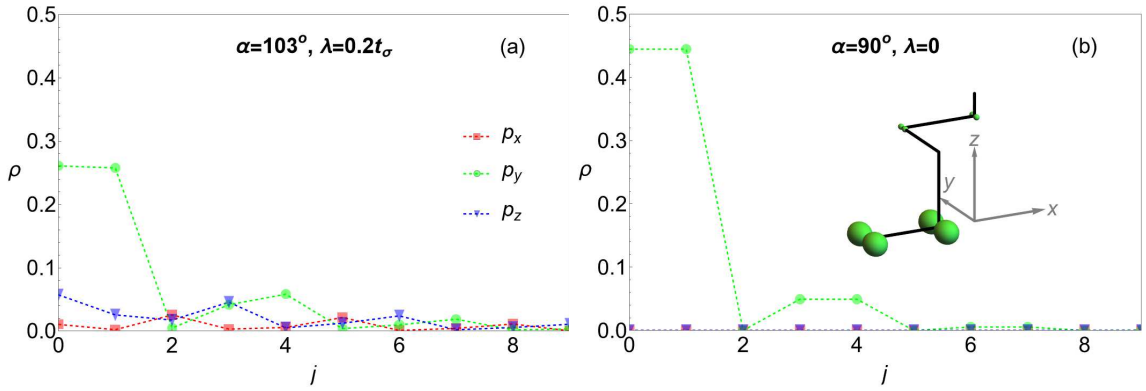

Figure 5.4: The end-state orbital density as a function of site number j, starting from $j = 0$ at the left edge, for a chain cut across two y bonds: (a) for the chalcogen chain model (2.48) ($\alpha = 103°$, $t_\pi/t_\sigma = -1/3$) with $\lambda/t_\sigma = 0.2 < \lambda_{\text{crit.}}/t_\sigma$, (b) for the cubic chain model (2.55) with $t_\pi/t_\sigma = -1/3$. Both plots use the GO basis defined in Sec. 2.2.2 (see Fig. 2.2 and Fig. 2.3). Also shown in panel (b): a schematic picture of the end-state charge density along the helix for the cubic chain model. The calculation was performed for a chain of length $L = 213$ sites (see text). Note that the orbital density in panel (b) is the same as that for the SSH-3 model, shown in Fig. 4.9.

5.2.4 End states

Fig. 5.4 (a) shows the real-space distribution of orbital densities in the end states of the chalcogen chain model ($\alpha = 103°$, $t_\pi/t_\sigma = -1/3$) with $\lambda/t_\sigma = 0.2 < \lambda_{\text{crit.}}/t_\sigma$, obtained using ED on an open chain of size $N = 213$ [5]. The orbital densities are plotted in the GO basis introduced in Sec. 2.2.2 (in particular, see Fig. 2.2 and Fig. 2.3). The overall charge density decays exponentially away from the edge while the end states have a strong orbital polarisation. This polarisation is dependent on the bulk bond pattern. In Fig. 5.4 it carries a predominantly p_y orbital character, since in the calculation the break in the chain occurs where a y bond would be if the chain were longer.

The end states of the chalcogen chain model are closely related to the end states

[5] This system size respects the three-atom unit cell of the chalcogen chain and at the same time is large enough for finite size effects to be negligible. It is smaller than the system size used to calculate the spectrum of the chalcogen chain model, because in this case one needs to track not only eigenvalues but also eigenstates. This system size was at the limit of processing power available for the calculations.

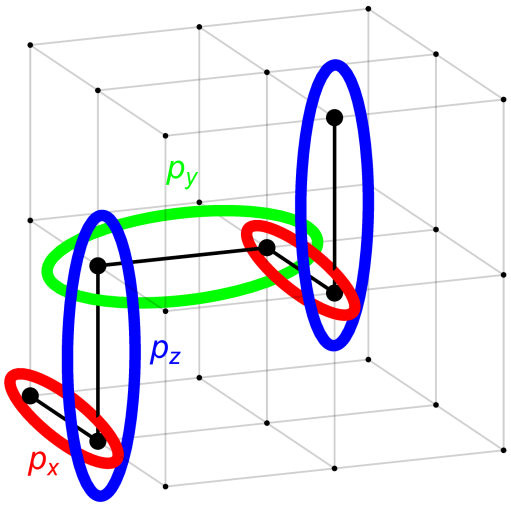

Figure 5.5: Dimers forming in the cubic chain model (2.55) (hole picture). The helical chain is shown in a cubic environment. Each dimer type, indicated by a different colour, appears on every third bond. For each dimer type, a distinct orbital tunnelling amplitude is amplified, so that each orbital experiences a $\cdots - t_\pi - t_\pi - t_\sigma - \ldots$ weak-weak-strong tunnelling amplitude when moving along the chain. This gives a SSH-3 model for each orbital flavour.

of the cubic chain model (2.55) with $t_\pi/t_\sigma = -1/3$ [Fig. 5.4(b)]. The relation between the two models is explored in the next section.

5.3 Chalcogen chain model vs cubic chain model

In terms of bulk topological properties, while both the chalcogen chain model (2.48) and the cubic chain model (2.55) possess a non-trivial LBO invariant $\mathcal{N}_\mathcal{W}$ (5.10), the cubic chain model has an additional invariant $\mathcal{N}$ (4.38). This additional invariant appears due to the absence of SOC and the resulting separation of spin degrees of freedom. Thus, the cubic chain model is topologically distinct from the chalcogen chain model.

The end states of the cubic chain [Fig. 5.4 (b)] are fully orbitally polarised, with vanishing p_x and p_z orbital densities[6]. The p_y orbital density, while exponentially

[6]While the orbital densities in Fig. 5.4 (a) are plotted in the particular GO basis introduced in Sec.

decaying away from the chain end, is modulated by a period-three, x-x-0 CDW. Strikingly, Fig. 5.4 (b) is precisely the same as Fig. 4.9, which shows the end states in the SSH-3 model. Under closer inspection this is not surprising, given that the cubic chain model splits into three SSH-3 chains and therefore the cubic chain end states are simply the end states of one of the three SSH-3 models (the one which is inversion-symmetric, see Sec. 4.3.1 for details).

Looking at Fig. 5.4 (a) vs (b) one sees that the modifications introduced in the chalcogen chain model on top of the cubic chain model, that is non-zero SOC interaction and the deviation from the bond angle $\alpha = 90°$, change the character of the end states in two ways. The first difference is a small admixture of the other two p-orbitals. It appears due to the coupling between the p orbitals which absent in the cubic chain model but present in the chalcogen chain model. The second difference is that the x-x-0 CDW modulation in the p_y orbital density observed in the end states of the cubic chain model is broken in the chalcogen chain model. However, its traces are still sharply visible, not least in the vanishing of the p_y orbital density on every third site. Overall, the end states in both models are remarkably similar. This is commonly seen in topological systems, when upon weak symmetry breaking a change in the invariant (by nature discontinuous) is accompanied by only a minute change in the end states, with the end states before and after the symmetry breaking adiabatically connected [66]. All of the above indicates that the insights gained from studying the end states of the cubic chain model – and, by extension, the SSH-3 model – can be used to understand the end states of the chalcogen chain model. Let me do just that.

In a 2/3-filled SSH-3 model the one hole per unit cell will accumulate in the anti-bonding state of the strong σ bond ($|t_\sigma| > |t_\pi|$). This can be thought of as a dimer, in which case the 2/3-filled SSH-3 model is a chain of dimers. Thus, the cubic chain model, which consists of three SSH-3 chains, is a helical chain of dimers – each orbital flavour forms one dimer per unit cell, which gives rise to an alternating dimer pattern in the chain (see Fig. 5.5). In this language, end states appear if one cuts the chain across a dimer. In the standard SSH-3 model, where there is one dimer for every three sites, this means that only certain cuts lead to end states. This reflects the fact that the SSH-3 model supports end states only if the unit cell is compatible with the cut and the strong bond is the inter-unit-cell coupling (see Sec. 4.3.1). In contrast, Fig. 5.5 shows that in the cubic chain model every cut leads to end states. It is just the orbital flavour of the end states which depend on the cut. There are

2.2.2 (see above), it is simple to show that the perfect orbital polarisation which characterises the cubic chain model is not recoverable for the chalcogen chain model, no matter the orbital basis.

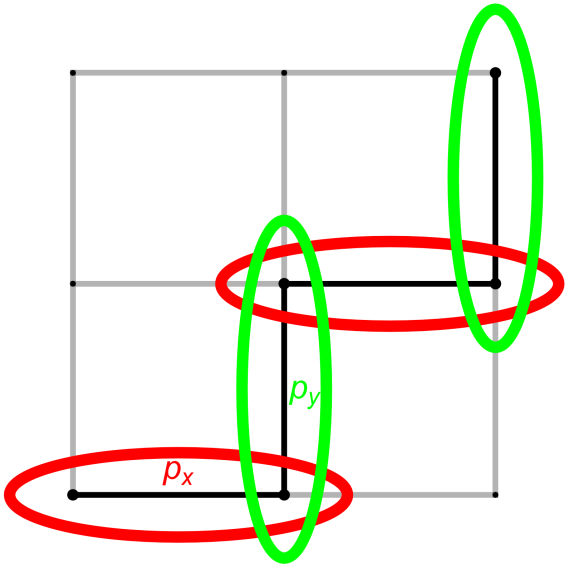

Figure 5.6: Dimers forming in the orbital SSH model. The zigzag chain is defined on a simple square lattice. Each dimer type, indicated by a different colour, appears on every second bond. For each dimer type, a distinct orbital tunnelling amplitude is amplified, so that each orbital experiences a $\cdots - t_\pi - t_\sigma - \ldots$ tunnelling pattern when moving along the chain. This gives an SSH model for each orbital flavour.

two end states for each cut – one for each end. This number is doubled to four if one considers two spin channels. These four end states are adiabatically connected to the four end states in the upper gap of the chalcogen chain model.

5.4 Comparison with orbital SSH model

The topological phase of the orbital SSH model (5.5)-(5.7) is easy to understand by analogy to the half-filled SSH model. As I have written above, the orbital SSH model consists of two uncoupled copies of a half-filled SSH model, one in each orbital flavour (p_x, p_y) (see Sec. 5.1 for details). Again, one can analyse the model in the language of dimers. The emerging dimer pattern is shown in Fig. 5.6.

Just as in the 2/3-filled SSH-3 model, in the standard, half-filled SSH model, with one dimer per unit cell, the presence of end states is dependent on the cut. If one cuts across two weak bonds no end states are found. If one cuts across two strong bonds (dimers), one observes end states. This reflects the observation that the SSH

model is topological if the unit cell is compatible with the cut and if the inter-unit-cell coupling is stronger than the intra-unit-cell coupling (see Sec. 4.2.1 for details). In contrast, Fig. 5.6 shows that no matter how one cuts the orbital SSH chain one always cuts two dimers – just like in the cubic chain model. Consequently, one always finds end states in the orbital SSH chain.

Despite these remarkable similarities, there is one crucial difference between the orbital SSH model and the cubic chain model. The end states of the orbital SSH model are the same as these of the standard SSH model. They stem from the winding number (4.19) and are protected by chiral symmetry. In contrast, the end states of the cubic chain model and, by extension, also the chalcogen chain model, are related to the SSH-3 model. They originate in the invariant (5.10) and are protected by the crystalline symmetry $\mathcal{R}_\pi$. Consequently, while the orbital SSH model is a FTI and is therefore robust, unaffected by lattice deformations, the cubic and chalcogen chain models are gapless at half-filling and cannot exhibit end-states protected by chiral symmetry. Instead, they are LSPTIs, protected by a lattice (spatial) symmetry and are susceptible to lattice disorder.

5.5 Conclusions

In this chapter I set out to study the topological properties of chalcogen chains which are the building blocks of the chalcogen crystal structure (see Fig. 2.5). The chalcogen chains are described by an electronic model with active p orbital degrees of freedom. There are two main results of this chapter. First, I have shown that in a realistic chalcogen chain model the occupied electronic bands carry a $\mathbb{Z}_2$ LBO [34] topological invariant. The invariant is non-trivial for realistic values of the SOC parameter λ and becomes trivial only for very large λ/t_σ. It is related to the number of -1 eigenvalues of the Wilson loop operator $\mathcal{N}_{(-1)}$ [59], and is protected by the 180° rotation symmetry $\mathcal{R}_\pi$ around an axis $\vec{r}$ normal to the helical chain. The end states of the open chalcogen chain are orbitally polarised, that is depending on the particular cut they have a predominantly p_x, p_y or p_z orbital character.

Second, I have demonstrated that the topological properties of the realistic chalcogen chain model can be understood by comparison with the simpler cubic chain model. The cubic chain model also describes a helical chain with active p orbital degrees of freedom, but with two important simplifications. (i) the helix bond angle is $\alpha = 90°$, instead of $\alpha = 103°$ for the chalcogen chain (ii) there is no SOC. The topological properties of the cubic chain model are closely related to these of the chalcogen chain

model, moreover, its topology can be simply understood as inherited from the SSH-3 model, whose topological invariant $\mathcal{N}$ (4.38) is protected by inversion symmetry.

I have also discussed how the cubic and chalcogen chain models relate to the orbital SSH model (5.5)-(5.7) (see Tab. 5.1 for a summary of models discussed in this chapter). While these three models are surprisingly similar, they are nonetheless topologically distinct. The orbital SSH model consists of two standard SSH chains, one per each p-orbital channel. The SSH model has a winding-number topological invariant, which is protected by chiral symmetry. As such, the orbital SSH model is an FTI. In contrast, the cubic and the chalcogen chain models' topological phases are protected by crystalline symmetry, making them LSPTIs.

Appendix A

Table of abbreviations

TB	Tight Binding (model)
LCAO	Linear Combination of Atomic Orbitals
CF	Crystal Field
SOC	Spin-Orbit Coupling
SSH	Su-Schrieffer-Heeger (model)
SSH-3	Period-three Su-Schrieffer-Heeger (model)
ODW	Orbital Density Wave
LBO	Lau-Brink-Ortix (invariant)
DMRG	Density Matrix Renormalisation Group
GBT	Generalized Bloch Theorem
GO	Global Orbital (basis)
LO	Local Orbital (basis)
GP	Generalized Pseudomomentum (basis)
AGO	Alternative Global Orbital (basis)
ALO	Alternative Local Orbital (basis)
AGP	Alternative Generalized Pseudomomentum (basis)
CDW	Charge Density Wave
SDW	Spin Density Wave
LP	Lone Pair
FTI	Fundamental Topological Insulator
AZ	Atland-Zirnbauer (class)
LSPTI	Lattice-Symmetry-Protected Topological Insulator

Table A.1: Table of abbreviations used in the thesis.

Bibliography

[1] N. N. Greenwood and A. Earnshaw, *Chemistry of the elements* (Elsevier, 2012).

[2] A. Auerbach, *Interacting electrons and quantum magnetism* (Springer Science & Business Media, 1998).

[3] I. Langmuir, "The arrangement of electrons in atoms and molecules.", Journal of the American Chemical Society 41, 868–934 (1919).

[4] H. A. Bent, "An appraisal of valence-bond structures and hybridization in compounds of the first-row elements.", Chemical Reviews 61, 275–311 (1961).

[5] A. Sommerfeld, "Zur elektronentheorie der metalle auf grund der fermischen statistik: i. teil: allgemeines, strömungs-und austrittsvorgänge", Zeitschrift für Physik 47, 1–32 (1928).

[6] C. Kittel and P. McEuen, *Introduction to solid state physics* (John Wiley & Sons, 2018).

[7] R. d. L. Kronig and W. G. Penney, "Quantum mechanics of electrons in crystal lattices", Proceedings of the royal society of London. series A, containing papers of a mathematical and physical character 130, 499–513 (1931).

[8] R. O. Jones, "Density functional theory: its origins, rise to prominence, and future", Rev. Mod. Phys. 87, 897–923 (2015).

[9] J. C. Slater and G. F. Koster, "Simplified lcao method for the periodic potential problem", Physical Review 94, 1498 (1954).

[10] F. Bloch, "Quantum mechanics of electrons in crystal lattices", Z. Phys 52, 555–600 (1928).

[11] W. Heitler and F. London, "Wechselwirkung neutraler atome und homöopolare bindung nach der quantenmechanik", Zeitschrift für Physik 44, 455–472 (1927).

[12] J. E. Lennard-Jones, "The electronic structure of some diatomic molecules", Transactions of the Faraday Society 25, 668–686 (1929).

[13] H. A. Jahn and E. Teller, "Stability of polyatomic molecules in degenerate electronic states-i—orbital degeneracy", Proceedings of the Royal Society of London. Series A-Mathematical and Physical Sciences 161, 220–235 (1937).

[14] H. Keller, A. Bussmann-Holder, and K. A. Müller, "Jahn–teller physics and high-tc superconductivity", Materials Today 11, 38–46 (2008).

[15] G. Sun, W.-L. You, and T. Zhou, "Topological phases of spinless *p*-orbital fermions in zigzag optical lattices", Phys. Rev. A 102, 063301 (2020).

[16] A. J. Heeger, S. Kivelson, J. R. Schrieffer, and W. P. Su, "Solitons in conducting polymers", Rev. Mod. Phys. 60, 781–850 (1988).

[17] N. Mott and R. Peierls, "Discussion of the paper by de boer and verwey", Proceedings of the Physical Society 49, 72 (1937).

[18] P. W. Anderson, "Antiferromagnetism. theory of superexchange interaction", Physical Review 79, 350 (1950).

[19] J. B. Goodenough, "Theory of the role of covalence in the perovskite-type manganites [la, m (ii)] mn o 3", Physical Review 100, 564 (1955).

[20] J. B. Goodenough, "An interpretation of the magnetic properties of the perovskite-type mixed crystals la1- xsrxcoo3- λ", Journal of Physics and Chemistry of Solids 6, 287–297 (1958).

[21] J. Kanamori, "Superexchange interaction and symmetry properties of electron orbitals", Journal of Physics and Chemistry of Solids 10, 87–98 (1959).

[22] K. I. Kugel and D. I. Khomskiıλ, "The Jahn-Teller effect and magnetism: Transition metal compounds", Sov. Phys. Usp. 25, 231 (1982).

[23] A. Von Hippel, "Structure and conductivity in the VI b group of the periodic system", J. Chem. Phys. 16, 372–380 (1948).

[24] J. R. Reitz, "Electronic band structure of selenium and tellurium", Phys. Rev. 105, 1233–1240 (1957).

[25] D. J. Olechna and R. S. Knox, "Energy-band structure of selenium chains", Phys. Rev. 140, A986–A993 (1965).

[26] H. Fukutome, "Charge density wave-soliton model for Se and Te", Prog. Theor. Phys. 71, 1–15 (1984).

[27] Y. Shimoi and H. Fukutome, "Vector charge density wave model of metallic and trigonal Te", Prog. Theor. Phys. 87, 307–329 (1992).

[28] A. Silva, J. Henke, and J. van Wezel, "Elemental chalcogens as a minimal model for combined charge and orbital order", Phys. Rev. B 97, 045151 (2018).

[29] A. Silva and J. van Wezel, "The simple-cubic structure of elemental Polonium and its relation to combined charge and orbital order in other elemental chalcogens", SciPost Phys. 4, 028 (2018).

[30] M. Matsui, "Role of interchain interaction in determining the band gap of trigonal selenium: a density functional theory study with a linear combination of Bloch orbitals", J. Phys. Chem. C 118, 19294–19307 (2014).

[31] D. I. Khomskii, *Transition metal compounds* (Cambridge University Press, 2014).

[32] A. Kłosiński, A. M. Oleś, C. E. Agrapidis, J. van Wezel, and K. Wohlfeld, "Chalcogenic orbital density waves in the weak-and strong-coupling limit", Phys. Rev. B 103, 235123 (2021).

[33] Y. He and C.-C. Chien, "Non-Hermitian generalizations of extended Su–Schrieffer–Heeger models", J. Phys. Cond. Matter 33, 085501 (2020).

[34] A. Lau, J. van den Brink, and C. Ortix, "Topological mirror insulators in one dimension", Phys. Rev. B 94, 165164 (2016).

[35] A. Pal, S. N. Shirodkar, S. Gohil, S. Ghosh, U. V. Waghmare, and P. Ayyub, "Multiferroic behavior in elemental selenium below 40 K: effect of electronic topology", Sci. Rep. 3, 1–7 (2013).

[36] A. Kłosiński, W. Brzezicki, A. Lau, C. E. Agrapidis, A. M. Oleś, J. van Wezel, and K. Wohlfeld, "Topology of chalcogen chains", Phys. Rev. B 107, 125123 (2023).

[37] P.-O. Löwdin, "On the non-orthogonality problem connected with the use of atomic wave functions in the theory of molecules and crystals", The Journal of Chemical Physics 18, 365–375 (1950).

[38] G. Kresse, J. Furthmüller, and J. Hafner, "Theory of the crystal structures of selenium and tellurium: the effect of generalized-gradient corrections to the local-density approximation", Physical Review B 50, 13181 (1994).

[39] J. van Wezel, "Chirality and orbital order in charge density waves", EPL (Europhysics Letters) 96, 67011 (2011).

[40] J. van Wezel, "Polar charge and orbital order in 2H-TaS_2", Phys. Rev. B 85, 035131 (2012).

[41] J. E. Hirsch, "Charge-density-wave to spin-density-wave transition in the extended Hubbard model", Phys. Rev. Lett. 53, 2327–2330 (1984).

[42] P. G. J. van Dongen, "Extended Hubbard model at strong coupling", Phys. Rev. B 49, 7904–7915 (1994).

[43] M. Tsuchiizu and A. Furusaki, "Phase diagram of the one-dimensional extended Hubbard model at half filling", Phys. Rev. Lett. 88, 056402 (2002).

[44] D. R. Hartree, "The wave mechanics of an atom with a non-coulomb central field. part ii. some results and discussion", Mathematical Proceedings of the Cambridge Philosophical Society 24, 111–132 (1928).

[45] S. Deng, J. Köhler, and A. Simon, "Unusual lone pairs in tellurium and their relevance for superconductivity", Angewandte Chemie International Edition 45, 599–602 (2006).

[46] S. Deng, A. Simon, and J. Köhler, "Lone pairs, bipolarons and superconductivity in tellurium", in *High T_c superconductors and related transition metal oxides: special contributions in honor of k. alex müller on the occasion of his 80th birthday*, edited by A. Bussmann-Holder and H. Keller (Springer Berlin Heidelberg, Berlin, Heidelberg, 2007), pp. 201–211.

[47] S. R. White, "Density-matrix algorithms for quantum renormalization groups", Phys. Rev. B 48, 10345–10356 (1993).

[48] U. Schollwöck, "The density-matrix renormalization group", Rev. Mod. Phys. 77, 259–315 (2005).

[49] E. Jeckelmann and S. R. White, "Density-matrix renormalization-group study of the polaron problem in the holstein model", Phys. Rev. B 57, 6376–6385 (1998).

[50] S. Nishimoto, E. Jeckelmann, and D. J. Scalapino, "Differences between hole and electron doping of a two-leg cuo ladder", Phys. Rev. B 66, 245109 (2002).

[51] A. Altland and M. R. Zirnbauer, "Nonstandard symmetry classes in mesoscopic normal-superconducting hybrid structures", Phys. Rev. B 55, 1142–1161 (1997).

[52] C.-K. Chiu, H. Yao, and S. Ryu, "Classification of topological insulators and superconductors in the presence of reflection symmetry", Phys. Rev. B 88, 075142 (2013).

[53] T. L. Hughes, E. Prodan, and B. A. Bernevig, "Inversion-symmetric topological insulators", Phys. Rev. B 83, 245132 (2011).

[54] R.-J. Slager, A. Mesaros, V. Juričić, and J. Zaanen, "The space group classification of topological band-insulators", Nature Physics 9, 98–102 (2013).

[55] H. C. Po, A. Vishwanath, and H. Watanabe, "Symmetry-based indicators of band topology in the 230 space groups", Nature communications 8, 50 (2017).

[56] J. Kruthoff, J. de Boer, J. van Wezel, C. L. Kane, and R.-J. Slager, "Topological classification of crystalline insulators through band structure combinatorics", Phys. Rev. X 7, 041069 (2017).

[57] J. Kruthoff, J. de Boer, and J. van Wezel, "Topology in time-reversal symmetric crystals", Phys. Rev. B 100, 075116 (2019).

[58] C.-S. Lee, I.-F. Io, and H.-c. Kao, "Winding number and zak phase in multi-band ssh models", Chinese Journal of Physics 78, 96–110 (2022).

[59] A. Alexandradinata, X. Dai, and B. A. Bernevig, "Wilson-loop characterization of inversion-symmetric topological insulators", Phys. Rev. B 89, 155114 (2014).

[60] L. A. Agapito, N. Kioussis, W. A. Goddard, and N. P. Ong, "Novel family of chiral-based topological insulators: elemental tellurium under strain", Phys. Rev. Lett. 110, 176401 (2013).

[61] T. Ideue, M. Hirayama, H. Taiko, T. Takahashi, M. Murase, T. Miyake, S. Murakami, T. Sasagawa, and Y. Iwasa, "Pressure-induced topological phase transition in noncentrosymmetric elemental tellurium", PNAS 116, 25530–25534 (2019).

[62] P. St-Jean, V. Goblot, E. Galopin, A. Lemaître, T. Ozawa, L. Le Gratiet, I. Sagnes, J. Bloch, and A. Amo, "Lasing in topological edge states of a one-dimensional lattice", Nat. Photon. 11, 651–656 (2017).

[63] F. Herman, C. D. Kuglin, K. F. Cuff, and R. L. Kortum, "Relativistic corrections to the band structure of tetrahedrally bonded semiconductors", Phys. Rev. Lett. 11, 541–545 (1963).

[64] M. Reis, *Fundamentals of magnetism* (Elsevier, 2013).

[65] C.-K. Chiu and A. P. Schnyder, "Classification of reflection-symmetry-protected topological semimetals and nodal superconductors", Phys. Rev. B 90, 205136 (2014).

[66] W. Brzezicki, M. M. Wysokiński, and T. Hyart, "Topological properties of multilayers and surface steps in the snte material class", Phys. Rev. B 100, 121107 (2019).